UNIVERSIDAD DE CHILE
FACULTAD DE CIENCIAS FÍSICAS Y MATEMÁTICAS
DEPARTAMENTO DE INGENIERÍA DE MINAS

GRAVITY FLOW AND FRAGMENTATION MODELING IN BLOCK CAVING

TESIS PARA OPTAR AL GRADO DE DOCTOR EN INGENIERIA DE MINAS

RENÉ ESTEBAN GÓMEZ PUIGPINOS

PROFESOR GUÍA:
RAÚL CASTRO RUÍZ

MIEMBROS DE LA COMISION:
KIMIE SUZUKI MORALES
ANDRÉS BRZOVIC PEREZ
LEONARDO DORADOR ORTIZ
LUIS FELIPE ORELLANA

SANTIAGO DE CHILE
2022

Resumen

MODELAMIENTO DE FLUJO GRAVITACIONAL Y FRAGMENTACIÓN EN MINERÍA DE BLOCK CAVING

En minería de Block Caving es fundamental comprender el comportamiento del flujo del material quebrado por su impacto en el diseño, operación y planificación minera. Sin embargo, debido a la gran cantidad de variables involucradas y la escala del problema, es difícil estudiar este fenómeno directamente en la mina. Existen variables, por ejemplo, que dependen del tipo de roca, el campo de esfuerzos y la dinámica de la operación en relación a la propagación del hundimiento y las políticas de extracción que definen el comportamiento del método. Este gran número de factores han sido estudiados con diferentes grados de detalle, en algunos casos con falta de entendimiento de impacto real. Por esto, en este trabajo son desarrollados diversos estudios de fragmentación secundaria, migración de material fino y esfuerzos en la columna de extracción, en el contexto de minería de Block Caving, con el objetivo de contribuir al estado del arte y proponer un modelo de flujo que integre la mayor cantidad de parámetros relevantes.

La estructura de esta tesis se dividió en 5 etapas. Primero se analizó el efecto de los diferentes tipos de roca a través de un modelo de fragmentación secundaria, para posteriormente comparar sus resultados a escala mina. Segundo, se complementó el estudio de fragmentación en material granular analizando el efecto que tiene la distancia recorrida por los fragmentos en la generación de material fino por abrasión. Tercero, se llevó a cabo un estudio experimental para analizar los esfuerzos inducidos generados en el material quebrado durante el flujo de material granular. Cuarto, se propone un modelo de esfuerzos verticales desarrollado en un simulador de flujo gravitacional basado en autómatas celulares. Finalmente, es incorporado un modelo de fragmentación y migración preferencial en el simulador de flujo gravitacional.

El modelo de fragmentación es calibrado en función del tipo de roca y esfuerzos. Adicionalmente, la generación de material fino es incluido en el modelo de fragmentación secundaria producto de la distancia recorrida por los fragmentos. Los estudios de fragmentación llevados a cabo en esta tesis consideran al esfuerzo vertical y la resistencia de la roca como variables claves. Por otro lado, el modelo de esfuerzos propuesto permite estimar los esfuerzos verticales presentes en el material quebrado, modelo que fue calibrado y validado con datos experimentales. Finalmente, los modelos de esfuerzo y fragmentación son incluidos en el simulador de flujo gravitacional, en el cual se utiliza el tamaño medio para incorporar la fragmentación y flujo de mineral, a través de la disminución del tamaño medio durante la extracción, tamaño que influye inversamente en la probabilidad de fluir del material.

El presente trabajo permite integrar diferentes aspectos claves que ocurren en la columna de material quebrado durante su extracción, a través de simulaciones de flujo gravitacional. Adicionalmente, una de las ventajas de incorporar los fenómenos estudiados en un simulador de flujo gravitacional basado en autómatas celulares es que permite representar diferentes aspectos de manera precisa y en tiempo cortos de simulación para la escala del problema.

Abstract

In block caving, the behavior of gravity flow is fundamental in mine design and planning. However, the great number of variables that influence this large-scale phenomenon are difficult to study directly in the field. There are variables that depend on the rock type, stress field and the dynamics of the operation itself through the caving progress and draw policies, which will define the performance of the method. This large number of factors have been studied to different degrees in some cases with lack of knowledge of their real influence. Thus, this work has developed various studies in block caving related to the secondary fragmentation, the migration of fine material and the stress in the draw column, in order to update the state of the art and propose a flow model that integrates a greater number of key parameters.

The structure of this thesis was divided into 5 stages. First, the effect of different rock types was analyzed in a secondary fragmentation model, and this model was compared with the what was found at the mine. Second, the study of fragmentation in the granular material was complemented by analyzing the effect of the travel distance in fragmentation by abrasion. Third, an experimental work was carried out to analyze the induced stress by draw in a broken column. Fourth, a stress model was developed using a flow simulator based on cellular automata. Finally, a fragmentation model and a fine migration model were incorporated in the previous flow simulator. These models included the rock size in the flow function.

In rock fragmentation, the described stages allowed a secondary fragmentation model to be calibrated based on different rock types. Additionally, a correction to the secondary fragmentation model is proposed, including a greater amount of fine material generated as a function of the travel distance. These fragmentation studies incorporate the rock strength and induced vertical stress. The proposed vertical stress models the stress generated in the extraction zones, which was calibrated and validated on an experimental scale. Finally, the stress and fragmentation models are included in the flow simulator which used the mean rock size as a key variable. The mean rock size is fragmented during draw and influences the flow probability inversely.

The present work allows different key aspects present in the broken column in block caving to be linked, simulating the gravity flow with greater precision and proximity to the real phenomenon. Furthermore, the advantage of incorporating the studies carried out in a gravity flow simulator based on cellular automata is that different aspects and parameters can be assimilated with good precision and in a reasonably short simulation for the problem scale.

Acknowledgements

Table of CONTENT

1. Introduction

In block caving, the behavior of gravity flow is fundamental in mine design and planning. However, the great number of variables that influence this large-scale phenomenon are difficult to study directly in the field. This large number of factors have been studied to different degrees in some cases with lack of knowledge of their real influence. Thus, this work has developed various studies in block caving related to the secondary fragmentation, the migration of fine material and the stress in the draw column, in order to update the state of the art and propose a flow model that integrates a greater number of key parameters.

Granular material can behave between solid and fluid at the macroscopic level [1], especially during flow. At the microscopic level, the particles can be described by stochastic interactions [2] mainly due to their random shapes, sizes, contact points and contact forces [3]. However, this randomness follows a degree of regularity, which has allowed the development of stochastic models to model the flow of granular material [2], [4]–[6].

In mining, the stochastic rules used for gravity flow have been applied through Cellular Automata (CA) [7]–[16]. Gravity flow modelling with CA is based on the void diffusion mechanism [4], [17]. This mechanism has been identified in Block and Sublevel caving mines [18]–[23], including in fine material fragmentation (< 0.4 mm [24]). CA have also been used for a wide variety of complex matter in models such as rough annular shear cells, lattice-gas, lattice-grain, hybrid models and movable CA [25]–[30].

In block cave mining discrete modelling should be used to properly represent the gravity flow over extraction level in the broken column where there are high rock columns of large rock fragments. Unfortunately, we lack methods that use discrete modeling in the broken column at block caving scale. Discrete Element Methods (DEM) are not preferable yet for full block cave scales because of the time required for simulation. In this work, we propose a gravity flow model that include a migration, fragmentation and stress models. The models are developed within a gravity flow simulator based on CA to simulate the scale of the problem and flow conditions. The CA is able to quickly simulate gravity flow in high draw columns under different draw scenarios.

1.1 Hypothesis and objectives

"In block caving, the gravity flow in the broken column is rule by the granular material flow, inter-particle percolation and rock fragmentation"

<u>Main objective</u>

Develop new knowledge of gravity flow considering the migration and fragmentation on block cave mining, through the interaction of gravity flow and fragmentation models.

Secondary objectives:

- Improve the current Block Caving Comminution Model [31], including rock type variability though the UCS.
- Study the effect of the fragment travel distance on fragmentation.
- Propose a fine migration model using CA.
- Propose a stress model using CA.
- Integrate fine migration and fragmentation models using CA.
- Calibrate and validate the integrated models.

1.2 Thesis structure

In Chapters 2 and 3 are presented the background and literature review of this thesis divided in gravity flow (Chapter 2) and fragmentation (Chapter 3). In Chapter 2, gravity flow in block caving is introduced including the flow zones, mechanisms, fine material migration, stress and modelling using CA. In Chapter 3, granular material fragmentation is introduced including the fragmentation stages in block caving, secondary fragmentation, prediction tools and hang-ups. Finally, a brief summary of the literature review is presented in Chapter 4.

In Chapter 5, the main researches of this thesis are presented in five papers. The first paper updates a secondary fragmentation model [31] including different rock type and analyzed the use of the normalized breakage model. The second paper studies the granular material fragmentation due to travel distance, incorporating this finding in the secondary fragmentation model of paper 1. The third paper study the stress in granular material under different draw scenarios. The results of the third paper, more other works, are used to proposed a stress model presented in paper 4. Finally, in paper 5 is presented a percolation model based on CA including previous findings that is validate at mine scale.

2. Gravity flow in cave mining

In block caving, the rock mass is fragmented due to ore draw forming a caved column. The rock fragment in the caved column commonly are studied as granular materials. Granular material can behave between solid and fluid at the macroscopic level [1], especially during flow. At the microscopic level, the particles can be described by stochastic interactions [2] mainly due to their random shapes, sizes, contact points and contact forces [3]. However, this randomness follows a degree of regularity, which has allowed the development of stochastic models to model the flow of granular material [2], [4]–[6].

The flow of granular material by gravity is known as gravity flow. In caving mines, the main parameters of interest associated with the gravity flow are: the geometries of flow zones, fine material migration, rock fragmentation, stress distribution, inrush of mud or fine materials, among others [17], [32]. These parameters influence mine design and planning. Initial studies of some of these parameters have been carried out through physical models (e.g. [33]–[39] [33], [34], [36], [39]–[42]), back analysis of mine data (e.g.: [18], [38], [43]–[48]) and numerical modeling mainly by Discrete Elements Method (DEM) and Cellular Automata (AC) (e.g.: [10], [12], [49]–[55])

Several variables will influence the parameters of interest described, such as the material properties (e.g.: strength, friction, density, elastic moduli, cohesion), particle size distribution (PSD), cave geometry, column heights, depth, presence of moisture. These variables have been studied with different levels of detail in some cases, as presented below.

2.1 Flow zones

During ore draw from one or more drawpoints, different zones are generated by the movement of particles. Kvapil [36] identified the extraction zone, the movement zone and the stagnant zones. The extraction zones are defined by the initial position of the particles that were extracted. The movement zone is defined by the particles that have undergone a change in position with respect to their initial position. Finally, the stagnant zones are defined by particles which remain in their initial position during extraction.

In mining, identifying these zones (particularly the extraction and movement zones) allows us to know the ore to be recovered by drawpoints. In multiple draw, the geometry of the movement zones is defined if there is interaction between drawpoints, generating interactive flow [56]. On the other hand, if there is no interaction, a series of problems could be generated such as ore losses, stagnant pillars and dilution. The stagnant pillars can transmit stress to the extraction level [57]–[59]. The irregular extraction is related to migration of fine material; consequently, there is a potential risk of inrush of mud and/or fine material [60], [61].

First characterizations of the flow zones in granular material were carried out in physical models constructed for studies of silo design (e.g.: [35], [39], [42], [62], [63]). In these studies, the ellipsoid of movement was identified during gravity flow [36], among other parameters of interest. Figure 2.1 presents the ellipsoid of movement in the center generated during draw. Additionally, a zone of less

displacement is also observed when contacting the surface (2) and a stagnant zone (4) that delimits the movement zone (3). The geometry of the ellipsoid of movement depends on various parameters of the granular material and the system.
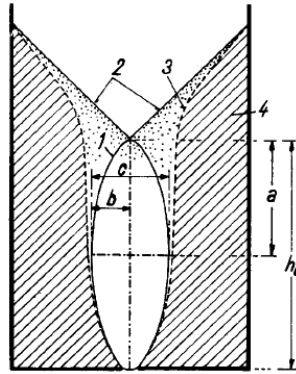
Figure 2.1 Flow zone observed in physical models [36]

There are analytical approaches that defined the geometry of this ellipsoid [6], [64], [65]. Nedderman & Tüzün [66] develop a kinematic model initially) which applied a profile distribution of velocities in which the upper particles move towards the lower particles that have the greatest velocity gradient ($\partial v / \partial x$) and a constant kinetic (B) which is correlated with the diameter of the particles. Bergmark-Roos model [67] which is developed from a force balance between the gravity and the friction of particles, causing the width to continually increase with the extraction height. Mullin [68] subsequently proposed that the distribution speed at these models converges.

Nedderman [64], through considerations made on the kinematic model, expresses a geometric relationship for the movement zone of a drawpoint. This relation, presented in Figure 2.2, has been used in caving to study the movement of fragmented ore. Here, the movement zone width increased continuously with its height.
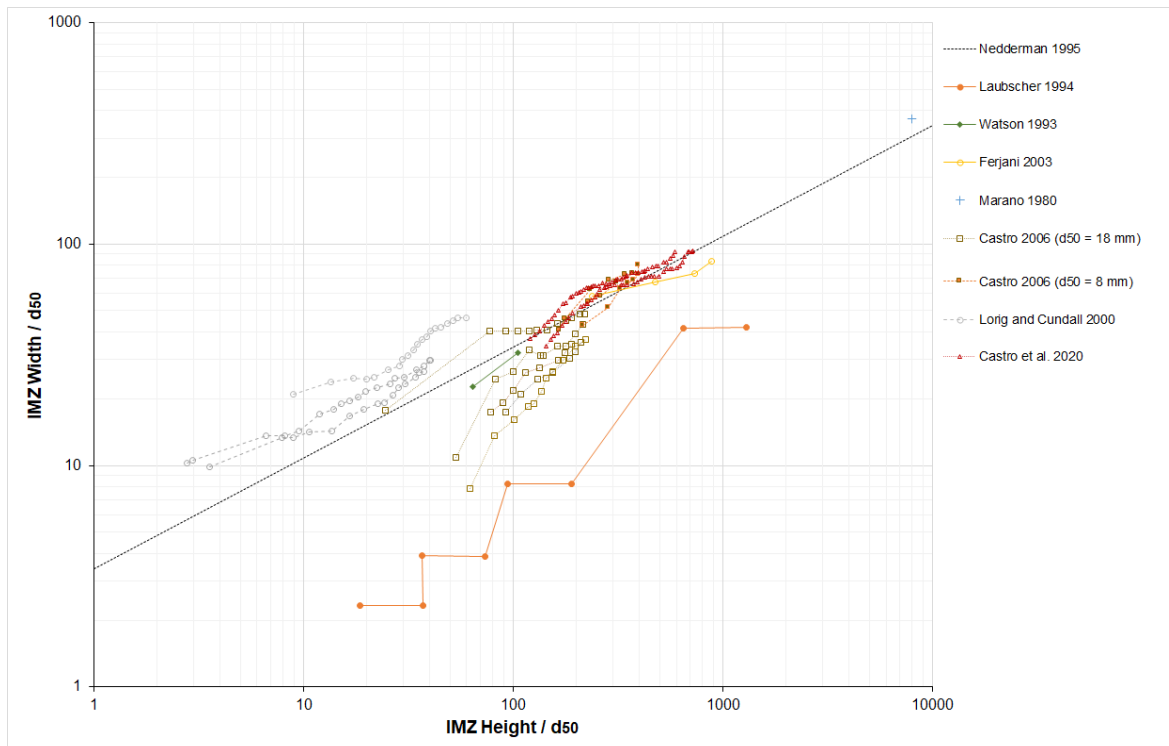
Figure 2.2 Width and Height of the movement zone relation at different studies (after [54])

The formula presented in Figure 2.2 has usually shown a good correlation with physical and numerical models [33], [52], [54], [69], [70]. This relationship gives a good approach to estimate the geometry of the ellipsoid during gravity flow. However, there are different parameters that influence the geometry of the ellipsoid, such as [32], [37], [40], [55]:

- Particle size distribution
- Drawpoint width
- Internal friction angle
- Rock quality
- Fragment's shape
- Moisture

2.1.1 Particle size distribution

The smaller the fragments, the narrower the ellipsoids. Kvapil [36] quantified the influence of fragment size, as seen in Figure 2.3. In mines, a diameter of 11.9 m has been reported for d_{50} of 25 cm (estimated [18]) and diameters between 6 to 15.1 m for d_{50} between 20 and 50 cm [71].
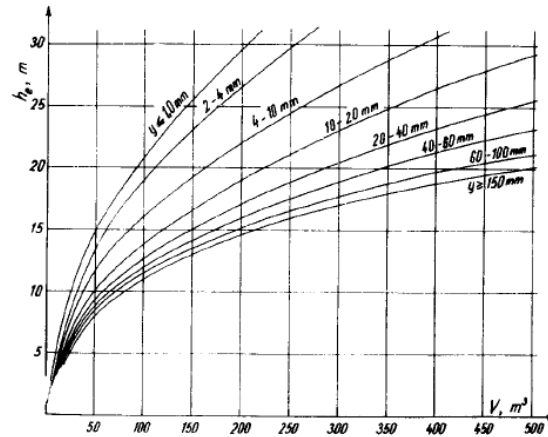
Figure 2.3 Ellipsoid of movement for different fragment size [36]

The PSD effect has been studied by different authors. An experimental study indicated that there is no significant influence on the movement zone width [72], in which two similar PSD were tested (Cu=d_{60}/d_{10} of 1.2 and 2.3). Castro et al. [73]also obtained similar results in a large-scale physical model using three Cu of 1.21, 1.53 and 2.33. On the hand, Hancock [52] reported a narrow ellipsoid when dense initial packing was used in a DEM study. However, Reyes [74] could not observe differences for a range of cohesive particles between 3.5, 4 and 4.5 cm, also using DEM.

At mine scale, Laubscher [40] introduced a graph to estimate the diameter of the ellipsoid considering ranges of rock sizes (or rock mass quality or ff/m) and the drawpoint width (Figure 2.4). In this graph, the minimum and maximum drawpoint spacing is also determined, maintaining the connection between adjacent flow zones.
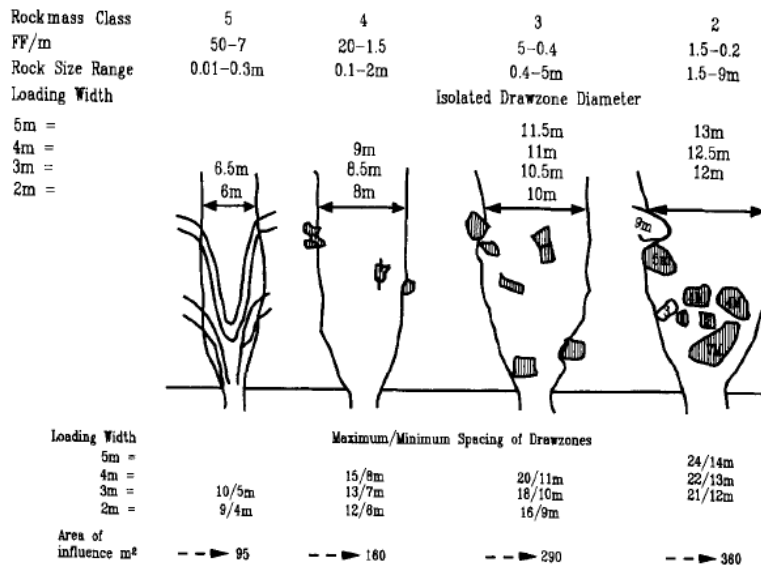
Figure 2.4 Empirical graph used to estimate IMZ diameter [40]

In Figure 2.5, the diameter of the isolate extraction zone (IEZ) has been estimated as function of d_{80}, based on a numerical tool calibrated with mine data [11], [75], [76]. The diameter grows with ore extraction, for a constant fragmentation, which has also been observed in physical models [33], [77]–

6

[79] and numerical models [80]. In block caving, the secondary fragmentation could stabilize this diameter.
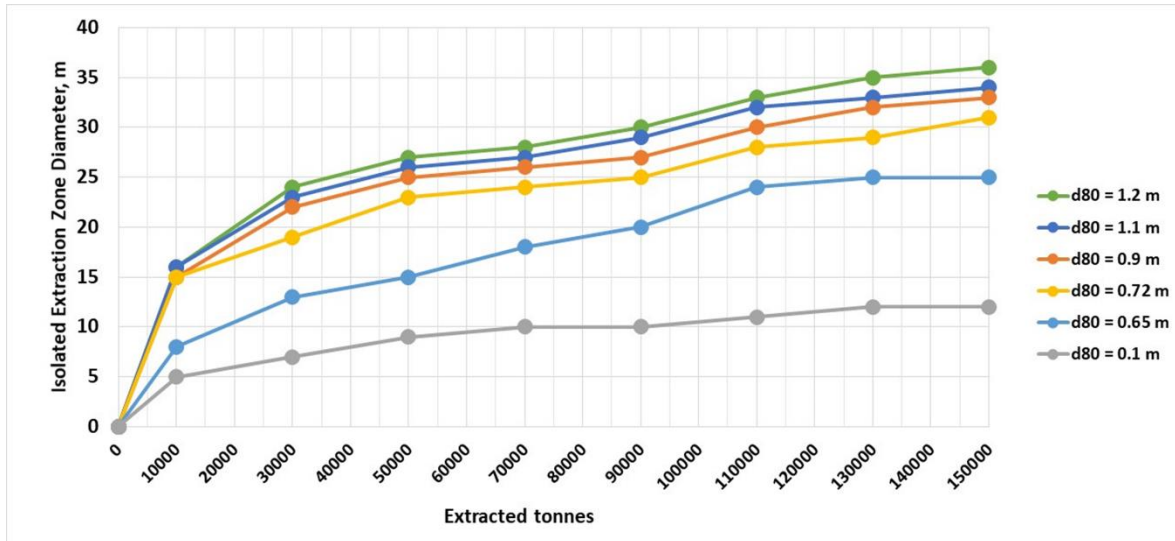
Figure 2.5 IMZ diameter evolution during ore draw [81]**.**

2.1.2 Drawpoint width

The opening of the drawpoint influences the geometry of the ellipsoid. Kvapil [36] introduced equation 2.1, in the case of a square opening with side *a,* to generate continuous flow.

$$a = \sqrt{1.4(5d_{50})^2} \qquad (2.1)$$

In Eq. 1.1, d_{50} is the mean fragment size [m]. Circular openings favor continuous flow. A circular area 15% smaller achieves the same efficiency as a square area [36]. Melo et al. [67] reported a direct correlation between the opening width and the diameter of the flow zone, through the kinematic model. In Sub-level Caving (SLC), Yu et al. [82] reported that the drawpoint width influences the IEZ diameter. However, some authors suggest that the drawpoint width does not have a significant impact [32], [33], [52], [74], [80]. Hancock [52], through observations in DEM, observed that the effect of the geometry of the opening only affects the near field. Then the IMZ diameter depends mainly on material properties.

In drawpoint design, one of the main criteria is to minimize the interruptions of the material flow. This can be controlled by defining a large ratio between the drawpoint width and the fragment size. Studies in ore pass and drawbells quantified the hang-up frequency at different ratios [83], [84], which are more deeply described in Section 2.3 Hang-up.

2.1.3 Interlocking friction angle

Susaeta [85] indicates that the friction angle is indirectly related to the diameter of the ellipsoid through Eq. 2.2, in which the diameter of the ellipsoid increases at lower friction angle. Laubscher [40] suggests that this inverse relationship is because the low friction allows fragments to travel

greater horizontal distances, which has been observed through numerical models (PFC3D [55]; FLAC3D [86]).

$$D = 5d_{80}tg(\phi)^{-7} \tag{2.2}$$

D is the diameter of the ellipsoid, d_{80} fragment size such that 80 % of the particles are smaller [m] and ϕ is the internal friction angle [°]. Susaeta [85] also proposes a formula between the internal friction angle and the particle distribution through the Cu (Eq. 2.3).

$$\phi = \frac{100Cu}{(1 + 2.332Cu)} \tag{2.3}$$

The interlocking friction angle is directly influenced by the fragment shapes, in which the lower sphericity, the greater the friction [55], [87]. Therefore, high friction angles can be expected in block caving due to the irregular fragment shapes, especially in early extraction stages. There are widely accepted and known methods for determining the angle of internal friction in a granular material, at laboratory scale. Nevertheless, Dorador [88] proposes a methodology to be able to scale the internal friction angle of fragments in block caving, making a similarity between the shear bands (around the IMZ) and a direct shear test.

2.1.4 Rock quality
The rock-mass quality is directly related to the geometry of the flow ellipsoid, as shown in Figure 2.4. A high rock mass index generates a wider ellipsoid diameter [40], mainly because high rock-mass quality implies coarse fragmentation. Additionally, poor rock quality can suffer more fragmentation during flow.

2.1.5 Fragment shape
The effect of the fragment shape in the ellipsoid of movement has been studied mainly using DEM. Pierce et al. [55] using PFC3D and later Hancock [52] using EsysParticle, analyzed and noted that the geometry of the flow zone of the granular material is influenced by the shape of the fragments. The more spherical particles generate larger diameters compared to angular particles.
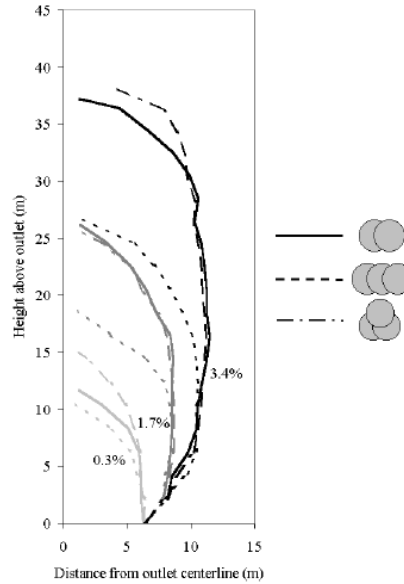
Figure 2.6 IMZ profiles with different clump shapes, using PFC3D [55]

2.1.5 Moisture

Moisture affects the flow-ability of the granular material [84], [89] as well as the geometries of the flow zones [78]. Sánchez et al. [78] observed through experiments in a physical model that the ellipsoid width increases with increasing humidity in the range of 0 to 6%, which was also observed by Antilao [90] in a range between 0 and 4%. Figure 2.7 shows the effect of the moisture in the extraction and movement zones.
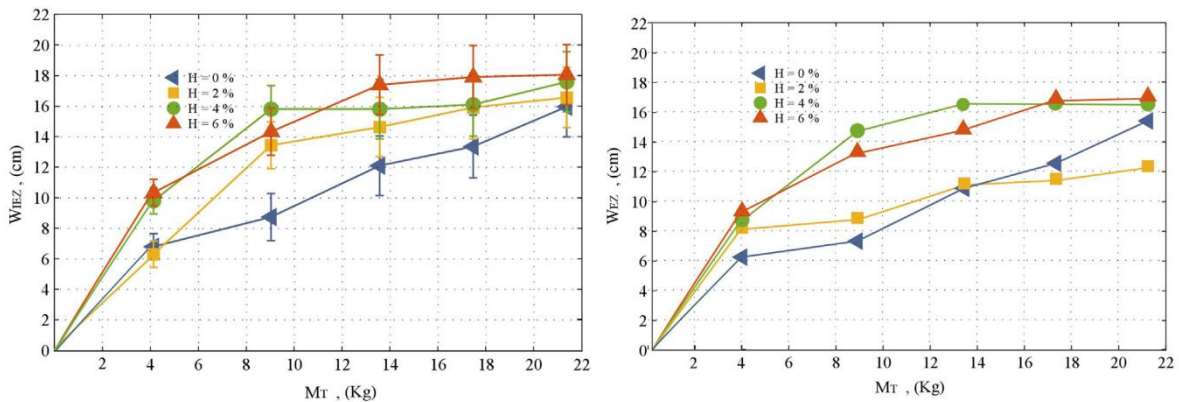
Figure 2.7 Moisture effect on extraction (left) and movement (right) zones [78]**.**

The moisture percentage used in Figure 2.7 could decrease the friction between particles when there is no presence of fine material. There are studies that indicate that the friction and shear strength decrease due to moisture content in clays [91]–[93], in gravel [90] and in different materials [94]. However, studies in sand using triaxial tests have not shown an effect of moisture content on the friction angle [95], between a range of 3 to 22% moisture. Moreover, Ayers [96] showed that the friction angle increased with humidity between 2 and 8% and then decreased, in tests on different granular materials through torsional shear tests. Apparently, there are a limit humidity percent in

which the friction angle start to decrease. This limit is small in coarse material. Then, it is expected in cave mining that the presence of water decreases the friction between fragments.

2.2 Mechanisms of gravity flow

Laubscher [97] proposed the main mechanisms used to study gravitational flow in block caving, presented in Figure 2.8. These mechanisms are indicated as follows:

- **Mass flow**, this mechanism occurs over the interaction zone where the material descends uniformly. The mass flow has little or zero blending, unlike the interaction zone where the highest blending can occur. In the interaction zone (see Figure 2.8) close to the drawpoints, the mechanisms of gravitational flow or void diffusion can occur.

- **Gravity flow**, was the first mechanism known as the classical gravitational flow mechanism [41], [98]. Here, the material flow is generated by the internal stress, towards the zones of lower stress, forming the so-called extraction ellipsoid (described in section 2.1).

- **Void diffusion,** is associated coarser granularity where the temporary generation of voids and rock arching occurs. The material flows due to the arch collapse, while the voids generated allow fine material to flow preferentially. This mechanism has been observed in fine rocks [71]. In particular, in SLC, such as Ridegay [18] and Perseverance Nickel mine, with fragmentation lower than 0.4 m, and an IEZ diameter of 11.5 m [24].
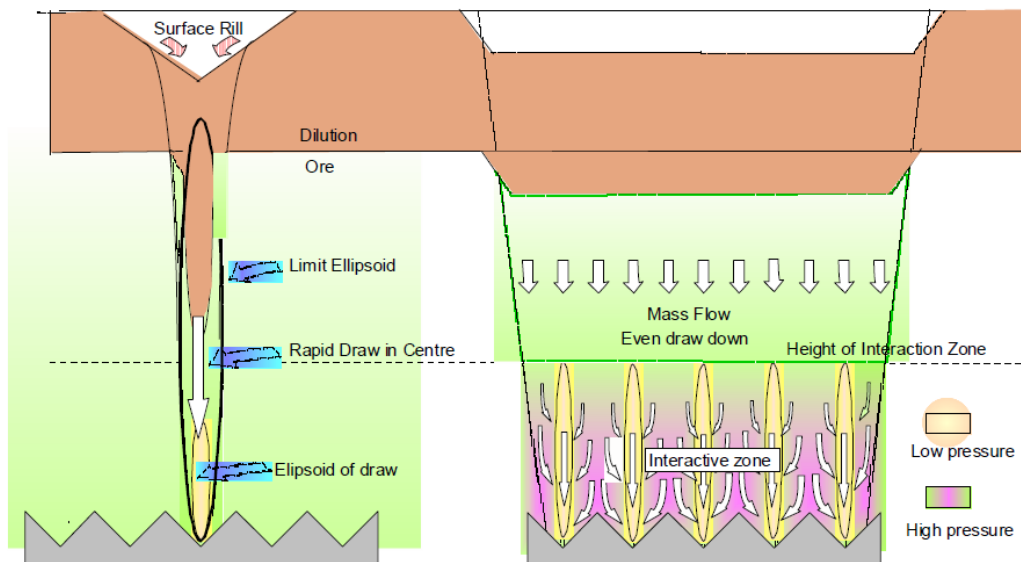
Figure 2.8 Gravity flow mechanisms in Block Caving [97]**. Left: Gravity Flow during isolate draw. Right: Mass Flow and interactive zone during multiple draw.**

The void diffusion mechanism is analogous to palm-and-finger [43] or disturbed flow [99], [100]. Brunton et al. [100] propose that this mechanism is associated with wide PSD and occurs because large particles or a group of coarse particles interrupt the movement of fine particles. On the other

hand, the void diffusion mechanism is associated with large rock fragments that fall and generate a flow of material of smaller granularity behind it. This flow mechanism has been observed through markers in sub-level caving and block caving mines [19]–[22], [43], [44], [100].

In the interactive zone, the presence of gravity flow or void diffusion mechanisms depend on the type of material [97]. Heslop [101] states that the mechanisms proposed by Laubscher are not mutually exclusive. Gravity flow is expected in rounded and good fragment distribution, while void diffusion is expected in material with a spaced or very wide PSD, and preferentially angular rocks. Additionally, Encina et al. [102] propose that the material between ellipsoids flow by the horizontal movement of fragment under compression. Different mechanisms have been proposed depending on the interaction or lack thereof between the movement zones of drawpoints. As example, Susaeta [32] defines 3 gravity flow mechanisms:

- **Isolate draw** occurs by the isolated extraction from a drawpoint forming a "vertical chimney". The characteristic parameters are the diameter and the uniform draw.

- **Interactive draw** occurs when there is interaction between drawpoints generating a flow zone that moves uniformly.

- **Isolate-interactive draw**, occurs by overlapping during the opening and closing of drawpoints. Here, the opening of drawpoints implies material flow towards the surface during the generation and collapse of mechanical arches. This implies horizontal movement between flow zones if there is interaction between points. Then, the closure of drawpoints generates material flow from an area of higher to lower density. This type of mechanism occurs over the crown pillar [103].

2.2.1 Interactive draw

The interactive draw between drawpoints is generated when the flow zones of drawpoints (2 or more) intersect at a certain height (Height of the interaction zone, Hiz), generating a common flow zone. The drawpoints spacing is the key parameter to induce the interaction of flow zones. Different authors propose different ratios between the drawpoints spacing and the IMZ diameter, which must be less than 1.2 or 1.5 [32], [40], [56], [102], [104].

A poor interaction can cause quick connection with the surface or with an upper level, resulting in dilution entry, which induces stress transmission to the extraction level [105], and causes poor recovery. On the other hand, a poor interaction due to large drawpoints spacing also generates less investment and more stability. Castro et al. [106] proposed a methodology that allows the drawpoints spacing to be defined.

In block caving, it is key to determine the spacing between drawpoints to ensure interactive draw. Ideally, the greater spacing must be selected to ensure this interaction because it provides a robust extraction level, large extraction drift for LHD maneuvers, and it minimizes the increase of costs [56]. In drawbells, the diameter of interaction (D_I) can be determined using the following formula [85],

$$D_I = D_{ps} + D_{IMZ} \qquad\qquad (2.4)$$

where, D_{ps} is the drawpoint spacing in a drawbell [m] and D_{IMZ} is the IMZ diameter [m]. Figure 2.9 indicates a different interaction between flow zone of drawpoints and drawbells. During ore extraction, an angle of draw is developed in the movement zone, which depends on various factors, such as the stress field, the material properties, the caving mechanisms, the extraction methods and the draw rate [107].
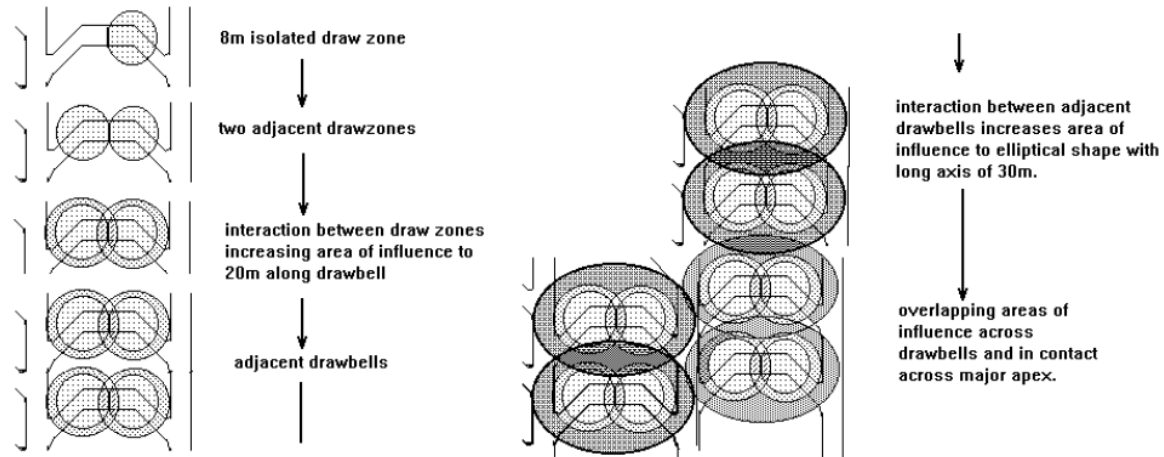
Figure 2.9 Drawpoints and drawbells interaction, plan view (after Lausbcher [56])

2.2.1 Far field and near field

Some authors propose classifying the flow zones according to the distance between the broken ore and the drawpoints, calling near field the zone close to the drawpoints and far field the furthest zone [52], [54], [88], [100]. In particular, this allows the gravity flow mechanisms that occur in high extraction columns to be better classified [54].

In the near field, shear bands are generated around the movement zones and a piston flow in the center, as shown in Figure 2.10. In the far field, a mass flow occurs similar to a plug flow. Dorador [88] proposed a secondary fragmentation model based on these fields. Pierce [54] stated that a reasonable shear band thickness could be 10 times the mean fragment size. The thickness of the shear bands was determined using DEM. However, the thicknesses of these bands have not been reported in physical modeling but has been empirically demonstrated.
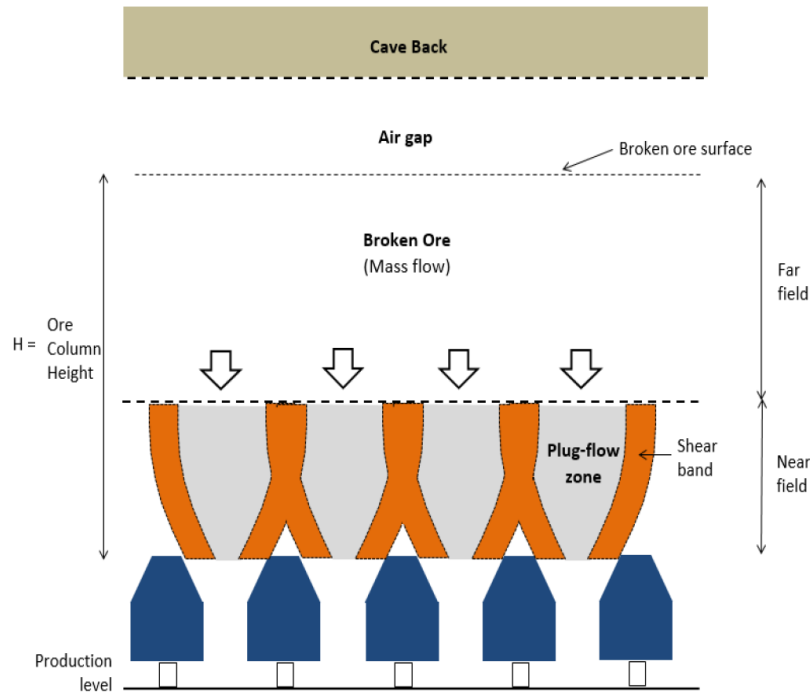
Figure 2.10 Far-field and Near-field in broken column [88]

A near field study was conducted by Brunton et al. [100] through markers placed at Ridgeway mine. In this study, a conceptual model is proposed in Figure 2.11. In this model, the blasted rock of the drawbell and undercutting are initially identified. Then, the ore flow is mainly fine material flow that drags coarse fragments, and finally, a slow movement of the coarse fragmentation flowing as a disturbed flow (void diffusion).
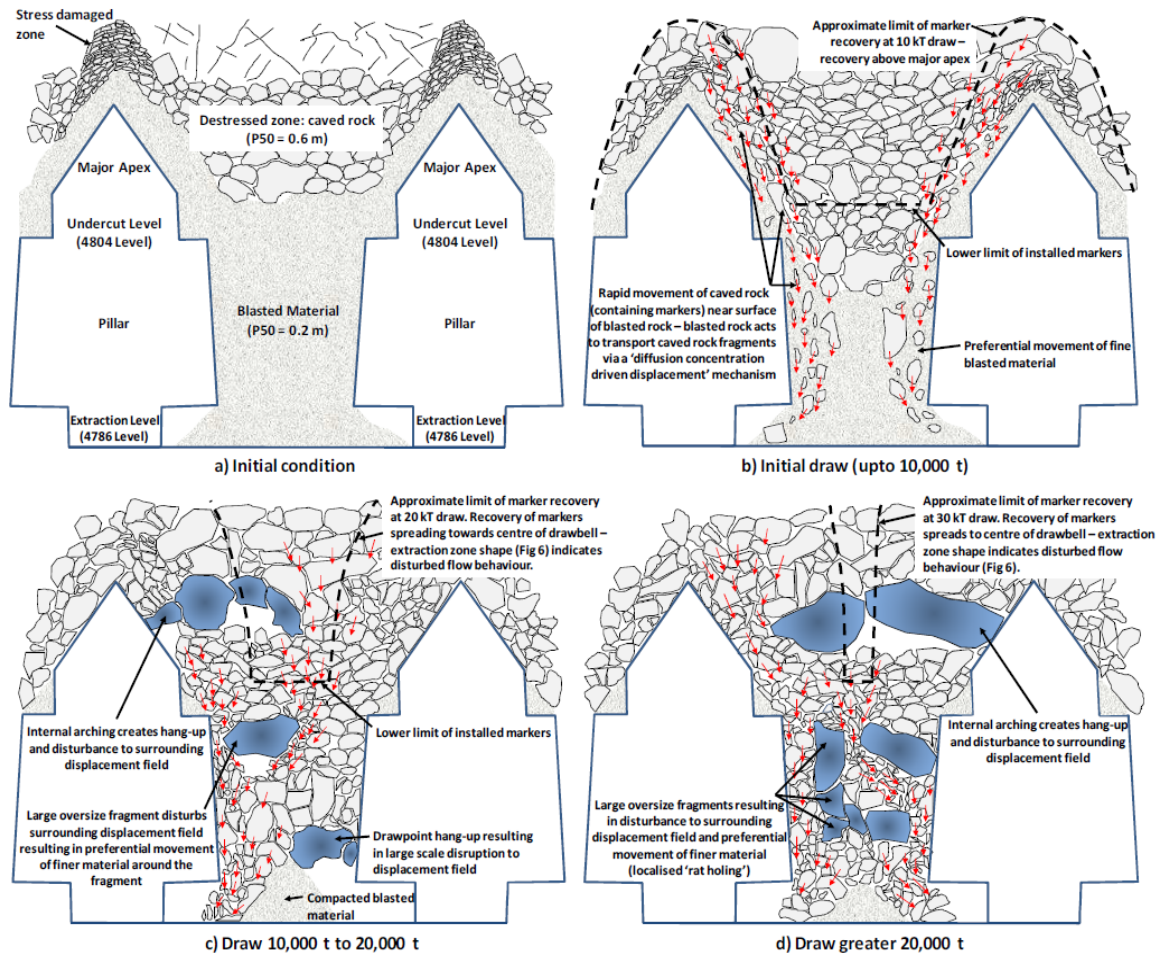
Figure 2.11 Conceptual flow model of near field [100]

2.3 Fine material migration

The particle percolation is a phenomenon that occurs in granular material as consequence of differences between the fragment sizes, the fragment densities or by shear strain [108], [109]. In block caving, the percolation of fine material occurs mainly through the preferential migration of waste rock of smaller granularity through the coarse ore, generating dilution. Dilution is the uneconomic material extracted from drawpoints that mixes with the ore, reducing ore grade, in some cases implying losses of reserves due to early closure of drawpoints.

Normally, fine material can be present within the ore column related to a previous exploitation level and may be found over or on the side of the ore column. Also, weaker rock and secondary rock fragmentation can generate fine material. Fine material can flow faster than coarse material during flow due to percolation [108], [110], and when it appears within the drawbell, it can generate cohesive hang-ups [78], mud-rush events [111], or inrush of fine events [61]. Furthermore, this fine material can cause the entry of dilution if it is waste material [112].

Differences in the following parameters can influence the dilution of fine material in block caving [103], [112]: fragmentation between coarse and fine material, mineral-diluent fragmentation, tonnages extracted between active points, drawpoint geometry and drawpoint layout. Laubscher[112]

mentions other variables such as the ratio of mineral/diluent volume, mineral-diluent disposal and form, flow interaction, extraction rate, and in-situ heights, which can affect dilution of fine material. Additionally, Laubscher [40] proposed the following formula to estimate the dilution entry:

$$DE = 100\frac{H_{dc}sf - H_{iz}}{H_{dc}sf}DCF \qquad (2.5)$$

where *DE* is the percentage of the draw column extracted when dilution is reported in drawpoint for the first time. $H_{dc}$is the height of the draw column (m), and *sf* is the swell factor (1.16 for finer fragmentation, 1.12 for medium fragmentation and 1.08 for coarse fragmentation). $H_{iz}$is the height of interaction, and *DCF* is the "Draw Control Factor" that can be determined as follows:

$$DCF = 1 - \frac{0.055d_e}{100} \qquad (2.6)$$

where d_e is the monthly standard deviation of drawpoint extraction (t). Additionally, many researchers have studied the fine particle migration phenomenon using shear and annular cells (i.e., [109], [113], [114]), physical flow experiments[33], [61], [77], [79], [115] and numerical modeling [54], [74], [114].

Bridgwater et al. [113] were among the first authors to quantify fine particle migration through physical experimentation, relating the ratio between particle size and the amount of percolation using shear cells with spherical particles. Hashim & Sharrock [109] conducted experiments similar to those of Bridgwater et al. but varying the shape of the particles, where it turns out that a more angular particle shape generates greater percolation, thus requiring the adjustment of the percolation equation. Pierce[54] conducted fine particle migration experiments through numerical simulations in PFC3D, concluding that fine particles have less lateral movement than coarse particles, and that migration occurs mainly vertically. Additionally, Pierce[54] used the Bridgwater model of percolation induced by shearing (Eq. 2.7) to estimate fine migration in block caving conditions.

$$\bar{L} = 4.5\Gamma\bar{d}exp\left(-k_2\frac{d_p}{\bar{d}}\right) \qquad (2.7)$$

Here, $\bar{L}$ is the mean percolation distance, and Γ is the shear strain while k_2 is a model constant that depends on the shear strain rate. The percolating particle diameter is d_p, and $\bar{d}$ is the mean particle diameter.

2.3.1 Dilution entry mechanisms

In block caving, the dilution entry is estimated primarily by vertical migration. However, Castro & Paredes[116] propose the existence of 3 main dilution entry mechanisms based on data collected from Block Caving mines in Chile:

- Vertical dilution is the gravitational migration of fine material through the ore column (Figure 2.12A).
- Lateral dilution is the mechanism generated by the presence of a large air gap and an angle of draw that can favor the fine material migration (Figure 2.12B).
- Caving dilution is generated by a bad propagation of the caving, which can imply a large air gap (Figure 2.12C).
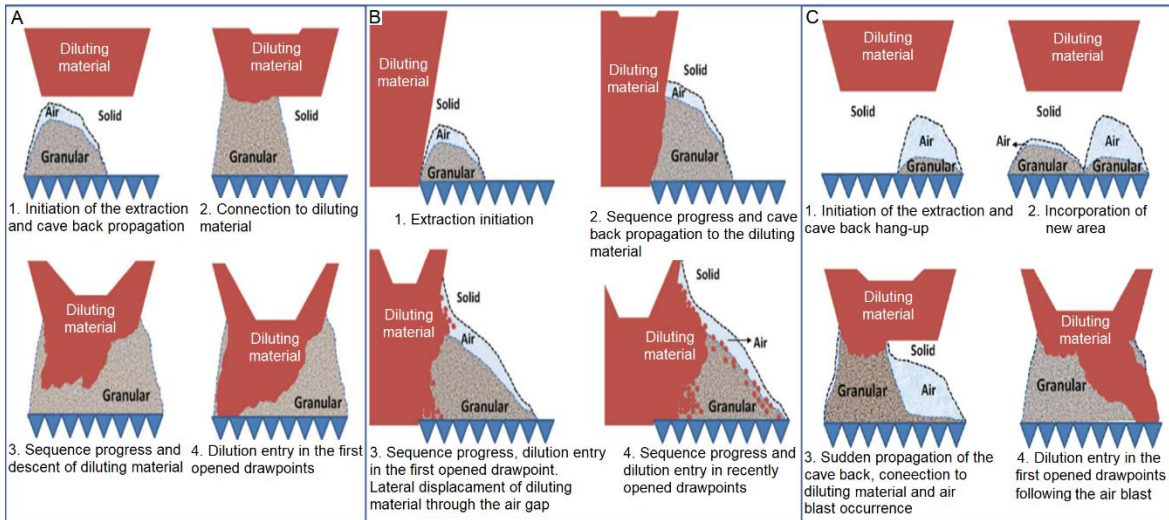
Figure 2.12 Dilution entry mechanisms[116]**. A: Vertical dilution, B: Lateral dilution, C: Caving dilution.**

The fine material movement can also be influenced by the presence of shear zones associated with geological structures [112]. Lateral dilution can be enhanced by high angles of draw in Panel Caving method, as has been observed in physical modeling [117].

On the other hand, Sougarret[118] proposes that the dilution entry can be delayed by the preconditioning due to the reduction in fragmentation. This lower fragmentation minimizes percolation, reduces hang-up events favoring uniform draw, and it improves the caving propagation by minimizing the air gap. The preconditioning has reduced connection times [119].

Susaeta [85] proposes the inclusion of the uniform draw using the Uniformity Index (UI) to determine the dilution entry. The UI indicates the uniformity that exists in the extraction of a drawpoint (p) with respect to its neighbors (i), defined by Eq 2.8.

$$IU = \Delta + \Gamma \frac{t_p - t_{min}}{t_{max}^2 \cdot n} \cdot \sum_{i=1}^{n} (t_{max} - t_i) \qquad (2.8)$$

Here, Δ is the amount of inactive drawpoints around the reference drawpoint p, Γ is a factor equal to 99/89, t_p is the tonnage extracted from the drawpoint p in a given period of time t, t_{min} is the minimum tonnage extracted in a drawpoint neighbor of p in period t, t_{max} is the maximum tonnage extracted in a drawpoint neighbor of p in period t, t_i is the tonnage extracted from a drawpoint i in period t neighbor of p, and n is the number of the total drawpoints including p. The second part of the equation is also

called the Specific Uniformity Index (SUI) and varies from 0 to 1. Here, 0 means absolutely uniform draw and 1 means isolated draw. Table 1 shows the correlation that has been found between UI and the DE using mine data.

Table 1 Relation between UI and DE [85]

Mine	Sector	Uniformity Index		Dilution entry
		%t = isolation	**% t = uniform + semi.**	**%**
El Salvador	Inca Norte	34	66	57
El Salvador	Inca Central	57	43	41
El Teniente	Quebrada Teniente	19	81	62
El Teniente	Teniente 4	34	66	54

There are numerical tools used to estimate dilution such as PCBC, also applied in SLC[120]; Flow simulators such as REBOP[54] and FlowSim[75] have also been used to simulate dilution entry, which have been compared in Figure 2.13. Moreover, Leonardi et al. [121], [122] models fine material migration using coupled models, applying a continuum model to represent the fine material (Lattice Boltzmann Method; LBM) and DEM for bulk material. One tool may be preferred over another depending on the level of detail and time required.
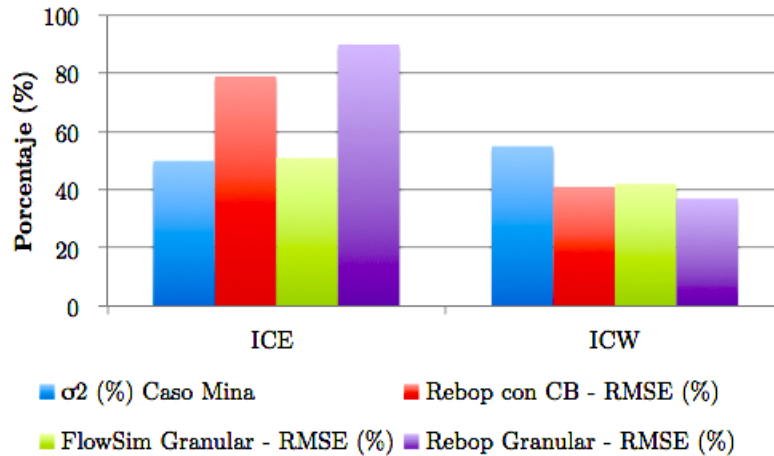
Figure 2.13 Dilution entry simulated using FlowSim and REBOP[75]**.**

2.3.3 Inrushes

In caving mines, fine material is associated with two major hazards: inrush of fine material and mud-rushes [123], [124]. The sudden entry of mud or fine material usually causes several problems such as injured workers, loss of life, damage to mining infrastructure and/or equipment, excess dilution, productions delays, permanent or partial closure of work sectors implying ore losses [125]. Examples of these inrush events are shown in Figure 2.14.

Figure 2.14 Inrush events in caving mines [124]**. Left: Inrush of fine event. Right: Mud-rush event.**

Inrush of fine material events (or dry rush) can be described as the suddenly inrush of wet and fine granular material at drawpoints [61]. On the other hand, mud-rush or mud-burst events occur when the mud entry is violent and quick, formed by a mixture of fine material, water, a disturbance and a discharge point [111]. These events can occur at any moment during mining as a result of ore extraction, seismicity, secondary breakage in drawpoint or ore passes [124]. Nevertheless, the risk of this hazard can be indicated and evaluated in previous mining through geology and geotechnical studies [126].

Several studies have reported inflow mainly from mud in block caving operations. For example, in El Teniente, a mixture of water from thawing and the fine materials generated during caving associated with overflow, caused a mud rush [127]. Another case was reported in Kimberley and De Beers diamond mines in South Africa. Here, mud events occurred because of the mixture of Kimberlite, which contains clays and shales, and water from rains. This water entered through an open pit operation located on the surface [128]. P.T. Freeport underground operations in Indonesia have also experienced mud-rush problems, which have caused fatalities [125]. Early wet muck entry was registered in IOZ mine [129] and DOZ mine [130], [131].

Various measures have been developed in order to prevent mud-rush events or to mitigate their damage. For example, in the Kimberley-Wesselton mine, South Africa, additional drifts were developed to increase mine drainage. These drifts helped decrease the amount of water; however, they weren't enough to prevent rainwater from dumps from entering the drawpoints, and consequently, the mud re-entry [111]. Another example of a mitigation measure was done in Even at the Dutoitspan Mine. Here, the surface clays and the kimberlite rock were mixed during the draw process. Additionally, the presence of groundwater generated wet muck [111] when mixed with kimberlite during draw. In the P.T. Freeport underground mine, the mitigation and control tools for mud problems are as follows: active water extraction through drainage pits, tele-operated LHD equipment in mud areas to reduce the exposure of mining personnel to the occurrence of a dangerous events, inspections of mud made by geotechnical engineers, hydrologists and operation engineers [132] and operational classification of the drawpoints with a table of criticality of the qualitative moisture of the mud [129], [131], which is a preventive method for closing drawpoints, and controlling extraction by using autonomous or semi-autonomous equipment to avoid the risk of personal accidents.

Planning tools have been developed to control or minimize mud-flow events. Hekmat et al. [133] developed a decision tool using an analytic hierarchy process to prevent mud-rush; the inputs were operational parameters, design parameters and geological parameters, where the extraction rate (an operational parameter) was the main controllable variable. Castro et al. [134] identified extraction rate and environmental conditions as the main variables in a predictive model they developed using logistic regression. Also, fuzzy logic was used as a tool to prevent mud-rush by determining the status of drawpoints through the estimation of the spatial-temporal distribution of wet muck [135].

2.4 Stress in granular material

Studies of stresses in granular material have been carried out for many years due to its importance in many industries (i.e. Food[136], Pharmacy[137], Mining[138]). In block caving mining, where the granular material are large rock fragments within a broken column of hundreds of meters, this approach has been used in soil mechanics to estimate stresses in the caved column [54], [59], [70] using the corrected classical Janssen approach[39] as an initial stress estimation,

$$\overline{\sigma_v} = \frac{R_h \rho_b g}{\mu k}\left(1 - e^{-\frac{\mu k z}{R_h}}\right) + Q_0\left(e^{-\frac{\mu k z}{R_h}}\right) \tag{2.9}$$

Where $\overline{\sigma_v}$ is the mean vertical stress, R_h is the hydraulic radius (area/perimeter; m), ρ_b is the bulk density (kg/m³), g is the gravity constant (m/s²), k is a friction parameter that represents the horizontal and vertical stress ratio, σ_h/σ_v, z is the depth (m), Q_0 is the initial vertical overload (Pa) and μ is the friction between particles and walls. Eq. (2.9) has shown good approximation in gravity flow experiments simulating a Block Caving environment [70]. The friction parameter μ is commonly defined with the Coulomb coefficient as follows [139]–[141]:

$$\tau = \mu \sigma_h \tag{2.10}$$

Here, τ is the shear stress placed between the model wall and granular material (Pa), and σ_h is the horizontal stress (normal to wall, Pa). Also, μ can be separated into a static, μ_s, and a dynamic, μ_d, resulting in a parameter where $\mu_s > \mu_d$ [136]. If there is adhesion between the granular material and the wall, Eq. 2.12 at the wall must be modified as follows[142]:

$$\tau = \mu \sigma_h + c_w \tag{2.11}$$

Here, c_w is the adhesion parameter. Additionally, μ is defined as follows [143], [144]:

$$\mu = tan(\phi_w) \tag{2.12}$$

where ϕ_w is the friction angle between the wall and the granular material. Some authors indicate that for fully rough wall this angle can be assumed to be close to the inter-particle frictional angle ϕ_i [139], [145]. Moreover, if the friction wall angle is greater than the internal friction angle, Nedderman [142] indicates that the internal friction angle must be used in the Equation instead of the friction wall

angle because in a fully rough wall the material does not slip along the wall, but rather the slip occurs along an internal slip plane.

Thus, considering the existence of a static ($\phi_{w,s}$) and a dynamic ($\phi_{w,d}$) wall friction angle, the following condition holds: $\phi_{w,d} < \phi_{w,s} \leq \phi_i$. In cave mining, because the wall is formed by the same un-caved rock, it can be expected that $\phi_{w,s} \leq \phi_i$. Due to the interlocking between rock fragments, there should be greater friction.

It is well known that a drawback of the Janssen approach is the determination of friction parameters, k and μ [146](Zhao et al. 2018A). The parameter k only depends on the material properties and is independent of μ [147], [148], and in several cases is considered constant, but it varies with depth [139], [148], [149]. Zhao et al. [150] observed that k decreased asymptotically to a constant value. Moreover, k also could vary in the horizontal direction depending on the distance with the walls. Additionally, μ is not necessarily a constant parameter. Peng et al. [151] in an experiment with glass beads, showed that μ has a dependence on the depth. Moreover, Vivanco et al. [152], through DEM simulation, also reported the same behavior of μ.

It is common to assume that σ_h and σ_v are the principal stresses; however, this is not true in the boundary due to the existence of vertical shear stress related to the wall friction. Walker [143] proposed the incorporation of a distribution factor, D_f, to represent the ratio of the vertical stress at the wall, $\sigma_{v,w}$, and the mean vertical stress, $\overline{\sigma_v}$, as follows:

$$D_f = \frac{\sigma_{v,w}}{\overline{\sigma_v}} = \frac{1 + sin^2(\phi) + 2sin(\phi)\sqrt{1-c}}{1 + sin^2(\phi) + (\frac{4c}{3})sin(\phi)(1 - (1-c)^{1.5})} \tag{2.13}$$

Here, $\sigma_{v,w}$ is the vertical stress at the wall (Pa), and c is defined as $tan(\phi_w)/tan(\phi)$ or it equals 1 for fully rough walls. Then, Eq. 2.10 is updated to Eq. 2.15.

$$\overline{\sigma_v} = \frac{R_h \rho_b g}{\mu k D_f}\left(1 - e^{-\frac{\mu k z}{R_h}D_f}\right) + Q_0\left(e^{-\frac{\mu k z}{R_h}D_f}\right) \tag{2.14}$$

Additionally, Walker [143] estimates k for a fully rough wall, based on the stress distribution correction, as follows:

$$k = \frac{1 - sen^2(\phi)}{1 + sen^2(\phi)} \tag{2.15}$$

In the literature, there are a lot of reported experiments of stress measurements in granular material, but usually how the wall friction angle was determined has not been reported. In addition, the Coulomb friction coefficient, μ is directly assumed (e.g.: [33], [42], [62], [139], [143]). Moreover, the method proposed by some authors [136], [142] to determine the wall friction angle cannot be directly applied to Block cave mining because of the scale of the problem.

2.4.1 Stress in Block Caving

Current challenges in the mining environment include factors such as deeper deposits, harder rock, higher in-situ stresses, greater production demand and increased costs [153], [154]. One issue which can have consequences at greater depths is that the rock mass already subjected to high stresses suffers even higher induced stresses during mining activities. In particular, induced stress occurs during the caving propagation stage in the advancing undercut front [40], [155], [156], where damage has been observed and reported in several block caving mines [157]–[162]. This is mainly related to drift convergence and pillar failure. Measurements of stresses, strain, crack extension and seismicity have been carried out at this stage [163]–[165]. However, in caving mines with greater depths, the column height of caved rock also increases, and consequently, there is an overload on the production level.

Usually in block or panel caving mines, when the caving propagation connects to surface, vertical stress over the production drifts is not closely monitored because of the low frequency and magnitude of seismic events. Nevertheless, experience indicates that production drift stability can also be affected during ore extraction in productive areas [57]–[59], [166]–[168] causing drift convergence, concrete slabbing at the walls, collapse, and closure.

Stress has also been measured in the extraction level of block cave mines [163], [169], [170] with different techniques for field stress measurement such as stress cells, over-coring, the Flat Jack test, and hydraulic fracturing [171]. Rojas et al. [163] used stress cells in the Esmeralda mine (within the El Teniente mine) and identified the need for production pillar rehabilitation after abutment stress to provide support stress during ore extraction. Xia et al. [170] also studied the stability of the extraction level before and after undercutting in the Tongkaungyu mine using over-coring. In this mine, the stability problems mainly occurred during the undercutting but stability problems were also reported during ore extraction. Additionally, indirect techniques have been applied. Martin et al. [172] proposed stress model calibration based on the drift damage and the depth of failure, while Gonzales et al. [173] used the damage observed in borehole cameras to model stress. In the Deep Ore Zone mine, they measured production drift convergence [174], where stress concentration during ore extraction was observed. Another indirect technique was proposed by Xia et al. [175] to estimate stress in the extraction level through the thin plate theory.

In the broken column of a block caving mines, there are irregular boundary geometries of caves, variable column heights, different cave wall dips and zones under draw or with non-draw (known as movement and stagnant zones respectively[33]) that make this process more involved than bin extraction. Pierce[54] proposed to assume the Janssen[39] approach as an initial stress estimation and then used the area tributary theory to estimate the stresses in the stagnant and movement zones of the broken columns. The vertical stress in the stagnant zone, $\overline{\sigma}_v^S$, could be determined as follows:

$$\overline{\sigma}_v^S = \frac{\overline{\sigma}_{v,0}A - \sum_{i=1}^n \overline{\sigma}_{v,i}^M A_i}{A_s} \qquad (2.16)$$

Where $\overline{\sigma}_{v,0}$ is the mean vertical stress before draw (initial condition, Pa), A is the total area of the cave in a planar view (m^2), and $\overline{\sigma}_{v,i}^M$ is the mean vertical stress of the movement zone i (Pa). Ai is the

area of the movement zone i (m^2), and As is the area of the stagnant zone (m^2). The estimation of the $\overline{\sigma}_{v,0}$ and $\overline{\sigma}_{v,i}^{M}$, can be determine considering the Janssen[39] approach (Eq. 2.9).

2.5 Gravity flow modeling using cellular automata

The most commonly used methods to model gravitational flow in caving mines have been: physical modeling, DEM and CA. However, continuous methods such as FEM using FLAC3D [86] have also been used, as well as a combination of different methods [13], [176]–[179]. A common tool used to study complex granular media problems is the distinct element method (DEM; [180]), frequently used in mining studies [50], [52], [55], [74], [83]. However, in cave mining studies [52], [55], the problems have been limited to a drawbell, a short column height and simplified shape fragments because of the problem of scale. As an example in [50], a draw simulation of a cylindrical model of 0.7 m height and 0.34 m diameter takes between a week and a month to complete. Thus, this section is focused on cellular automata, which provide the advantage in block caving of being able to simulate high broken columns with multiple drawpoints in short simulation times (<1 h). The main disadvantage is that this method doesn't simulate the physical interaction between the fragments.

Granular media can be described by stochastic interactions [2] mainly due to their random shapes, sizes, contact points and contact forces [3]. These stochastic rules have prompted the development of stochastic models of granular material flow [2], [4]–[6], [181]. In mining, the stochastic rules used for gravity flow have been applied using CA [7]–[16], [43].

The gravity flow modeling with CA is based on the void diffusion mechanism[97], which has been identified in Block and Sub-level caving mines[18]–[22], [44], and in fine material fragmentation (< 0.4 mm[24]).

2.5.1 FlowSim

FlowSim is an AC-based gravity flow simulator, initially developed in Matlab in a 2D and 3D environment [10], [33]. In its first version, FlowSim represents the gravity flow observed in a large-scale physical model, quickly and efficiently. Then, it was validated with mine data [11], simulating sectors of the El Salvador and El Teniente mines, Codelco. In this validation, the flow simulator simulated the ore dilution, mixing and ore recovery.

The flow simulator used a 3D cubic cell arrangement to represent granular material, while the material flow is generated as void cells moving upwards starting from drawpoints. The void cells are exchanged with upper granular cells. Each upper granular cell has a probability, P_i, of being selected to exchange (see Figure 2.15) based on its distance as follows [10]:

$$P_i = \frac{d_i^{-n}}{\sum_{k=1}^{9} d_k^{-n}} \qquad (2.17)$$

Where di is the distance between the void cell (k level, Figure 2.15) and one of the nine cells i (k+1 level, Figure 2.15B), and n is a function parameter that depends on rock properties such as fragmentation. Studies have shown that for the cell size 2x2x2 (m^3), the parameter n calibrates between 3 and 10 depending on rock properties, and $n = 3$ or $n = 4$ are most frequently used for coarse

22

fragmentation; for smaller rock fragments, *n* is increased, linked to the width of the flow zone [11], [44], [75], [76]. Additionally, a minimum number of adjacent voids are required to interchange cells. Therefore, when a cell void is evaluated to move up, the amount of void cells, *Cv*, around it are calculated (Eq. 2.18).
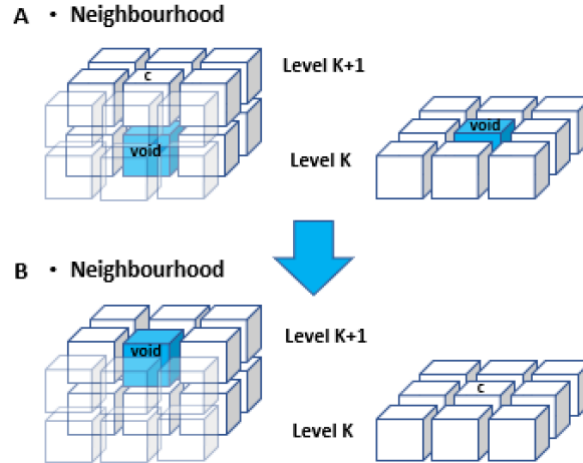
Figure 2.15 Representation of the descent of a superior block into a void available from a k + 1 level to a k level [76].

$$Cv = \sum_{k=0}^{1} \sum_{j=-1}^{1} \sum_{i=-1}^{1} (c_{ijk}), \forall c_{ijk} > 0 \qquad (2.18)$$

Where, $c_{ijk} = 1$ if there is a cell void and 0 if not. Then, the void cells flow up if

$$Cv \geq C_v^{threshold} \qquad (2.19)$$

where $C_v^{threshold}$ is the minimum void cells to propagate the flow using Eq. 2.17 Miranda [182] implements the algorithm in the C++ language, in order to reduce simulation times. Then, some authors [75], [183], [184] incorporated a rilling logic and preferential flow. The cave-back is also applied in the flow simulator [75], [184], using DXF files to discretize whether a block was caved or not.

Fuentes [185]calibrates the model with data from Esmeralda mine (Sector 2), El Teniente, collected through Smart-marker in 5 drawbells (135 markers recovered at the date of the study, 43% of the total). Figure 2.16 shows a simulation using FlowSim of the Emeralda mines (Sector 1 and 4; 370 drawpoints) after calibration with sector 2. Vergara [117] simulated the ore entry from a previous mine level calibrated using physical modeling with an error under 10% of mine data.
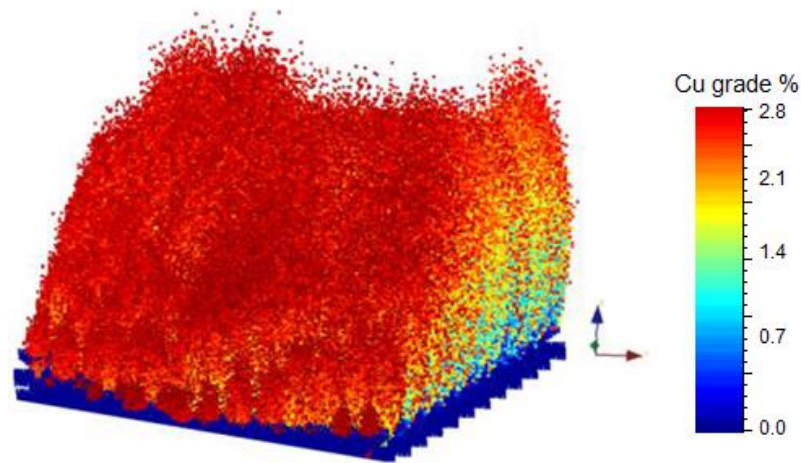
Figure 2.16 FlowSim simulation of Esmeralda mine, El Teniente [185]

In parallel with the development of the flow simulator, this model has been calibrated, validated and/or applied in various mines, a such as El Salvador, Esmeralda in El Teniente, and PC1 and PC2 in Cadia. East [11], [75], [184], [186]. Recently, Vega [187] used to study mud-rush events through the uniformity and drawpoint interaction of different extraction level designs.

3. Granular material fragmentation in Block Caving

Rock sizes are fundamental in the mining process, mainly in design stages, ore extraction, ore transportation and mineral processing [40], [106], [188], [189]. In block caving, the prediction of rock sizes in the draw column influences the geometry of the flow zones, which defines drawpoint spacing, draw control, drawpoint productivity and secondary breakage [40]. Rock fragmentation is directly related to various operational problems during ore extraction such as hang-ups, oversize rocks, fine material migration, mud-rush and the inrush of fine material. Thus, rock fragmentation is key to understanding the rock fragmentation mechanisms and to predicting rock size distribution, which, together with the caving propagation, define the performance of the method [105].

In block caving, there are different stages and mechanisms that influence the resulting rock fragmentation observed in drawpoints. In mining methods that use blasting to fragment ore, it is possible to have a certain degree of control over the resulting fragment sizes. However, in block/panel caving, blasting is applied in the initial undercutting, and it may eventually also be applied in confined preconditioned spaces. Nevertheless, the greater ore column is naturally fragmented during caving and ore draw.

In block caving, the rock fragmentation increases during extraction [32], [190] due to primary and secondary fragmentation. Moreover, in a sublevel caving mine, rock fragmentation during draw has also been quantified [191]. Hence, it is important to understand the different stages of in-situ, primary and secondary fragmentation, which are described below.

3.1. Fragmentation stages in block caving

The fragmentation of a rock block is a complex process in which several variables are involved, such as rock characteristics (e.g.: strength, hardness, joints, friction, density, mineralogy) as external phenomena. Thus, the rock heterogeneity, mechanical properties associated with each rock type and environment must be known. Additionally, the ratio between the rock strength and induced stress generate high variability in rock mass fragmentation during caving [54].

During rock mass fragmentation, three fragmentation mechanisms have been defined: in-situ fragmentation, primary fragmentation, and secondary fragmentation [40], [192]. The in-situ fragmentation corresponds to what is naturally presented in the rock mass formed by blocks defined by joints. Currently, in this fragmentation fractures due to preconditioning have also been incorporated. Then, the primary fragmentation is observed during the caving process, caused by breakage and subsequent disjoining of blocks from the cave-back. Finally, the secondary fragmentation occurs in the broken column because of the rock movement in the column to the drawpoints [192]. Additionally, impact fragmentation can be considered depending on the size of the air gap, which can greatly affect the primary fragmentation [88].

There are two key stages that also influence the fragmentation observed at drawpoints from an operational point of view; the propagation stage of the broken column before breakthrough to surface (or previous level) and the extraction stage, when caving has connected to surface. These stages may influence the final fragmentation depending on the stages in which the fragmentation occurs. For

example, at the beginning of the caving, in the cave-back, there is mainly tensile stress and a short distance between the broken ore and the drawpoints. On the other hand, at higher caving heights of the caving, due to the geometry adopted by the cave-back, compression forces are generated which can overcome the compressive strength of the rock, leaving the rock in the breaking column with a post-peak resistance (lower). Additionally, the distance between the broken minerals and the extraction points increases. All of these influence the resulting primary and secondary fragmentation.

The initial block size distribution is the starting point from which the following fragmentation process can be determined. The main methodologies to represent in-situ fragmentation rely on joints quantification. Some of these are listed below:

- Q de Barton [193]: RQD/Jn
- ISRM [194]
- Volumetric Rock Quality Designation [195]
- Hardy et al. [196]
- Block Cave Fragmentation [197]
- JKFrag[188]
- Fracman[198]

The Discrete Fracture Networks (DFN) is one of the methods most used to determine in-situ fragmentation. In DFN, joints are three-dimensionally tessellated to represent the rock blocks, thus allowing their geometric properties (length and volume) to be determined. Then the size distribution curves are constructed. This method was originally developed to analyze groundwater flows through natural fracture systems. Nowadays, it is possible to find it in a wide range of areas. The main variables used to construct a DFN model are [199], [200]: joint frequency, joint orientation, joint length and fracture ends. Core-drilling campaigns or drift mapping can provide the information required to create the fracture network.

In block caving, the in-situ fragmentation and the preconditioning are key input parameters for the following fragmentation stages. There are studies in which the use of preconditioning, by hydraulic fractures, has been modeled in the initial fracture network [201], [202]. Hydraulic fracturing creates new fractures and extends/connects pre-existing joints (30-50m). The hydraulic fracture networks can be simulated based on the stress orientation and the estimated/measured fracture diameter, as presented in Figure 3.1. The pressure applied by hydraulic fractures could decrease the intact rock strength [203]. However, changes in fragmentation have mainly observed when confined blasting has been used [118], [119].
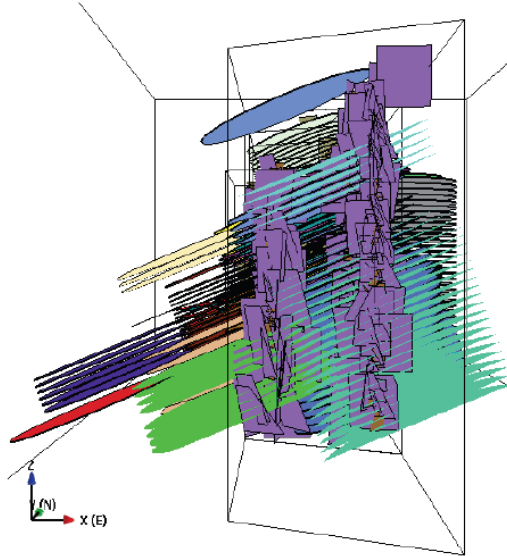
Figure 3.1 Hydraulic fracture modelling (disc) during fragmentation prediction [201]

In situ fragmentation influences primary fragmentation. The main variables that influence primary fragmentation are the stress distribution in the cave-back and the geo-mechanical properties of the rock mass [192], [204]. In primary fragmentation, the main mechanisms that are identified are the opening and/or sliding of joints under low compressive stress or tensile stress [192]. Thus, the in-situ joint networks govern the block formation during primary fragmentation [171]. Nevertheless, intact rock fracture can also occur under high compressive stress. The main parameters that influence primary fragmentation are [40], [188], [192], [205]:

- Joint frequency and joint spacing
- Main geological structures
- Induced stress
- Cave-back orientation and geometry
- Rock mass quality

3.1.1 Secondary fragmentation

Secondary fragmentation is the last fragmentation stage that the ore undergoes in the broken column before being extracted from the drawpoints. Here, the rock is mainly fragmented by compression and abrasion [188], [192]. Some authors [88], [192], [206], [207] also include fragmentation by impact, when a rock block falls from the cave-back. The fragmentation mechanics proposed during secondary fragmentation are [192]: extension of pre-existing discontinuities, opening of filled or healed discontinuities, opening along bedding or schistocity planes, crushing under superimposed weight, compressive failure of block by induced tension produced by point line or line loading at inter-block contacts within the caved mass, bending failure of elongated blocks and abrasion of block corners and edges to reduce block sizes and produces fines.

Abrasion occurs when insufficient energy is applied to fracture a fragment, generating localized stress in a small area. This can generate fine material, which is also known as peripheral fragmentation

[208]; compression fracture occurs when the energy applied is sufficient to load a small area to the breaking point. In soil mechanics, the granular material fragmentation by compression is usually divided into splitting [209] and total fracture [208]. On the other hand, the fracture by impact occurs when energy is applied in excess, generally resulting in a large number of fragments. In practice, these events do not occur in isolation; the presence of abrasion can be observed in points of load compression [188].

Variables that influence secondary fragmentation can be classified into those that depend on the rock and those that depend on the design parameters, such as [40], [206], [210], [211]: Broken rock: intact rock strength, size, shape and distribution of fragments, void index, friction between fragments, roughness, humidity, rock fractures and veins; Design parameters: column height, extraction rate, stress, draw strategies. Some of these parameters and variables are described below.

3.1.1.1. Rock strength
The strength is directly related to the capacity of support stress. A block strength is related to the intact rock strength, the joints and the deformation capacity. Low rock strength implies early breakage under stress [206], whereas increasing the rock strength decreases the amount of breakage [212]. The strength of a block is indirectly related to its size; an individual block decreases its strength when it increases in size [171]. Dorador [88] indicated that the block strength is the most relevant variable in fragmentation events in comparison with other parameters such as shape and size distribution of fragments.

3.1.1.2. Fragment size distribution
Breakage is greater in a uniform soil than it is in well-graded soils because there is a better stress distribution due to the contact number [213]. Furthermore, the strength ratio between the largest rock and the smallest particles plays an important role in the cushioning potential [209], [214]. Dorador [88] identified that the dense packing exhibits three key stages that represent different breakage steps: i) splitting initiation, ii) matrix collapse and fragment reorganization, and iii) matrix support strengthening. Collapse and reorganization have also been reported by Müller & Tomas [93]. Confinement also damages the particles as observed in Point Load Test (PLT) measurements before and after tests [88](Figure 3.2A); DE = PLT before / PLT after.
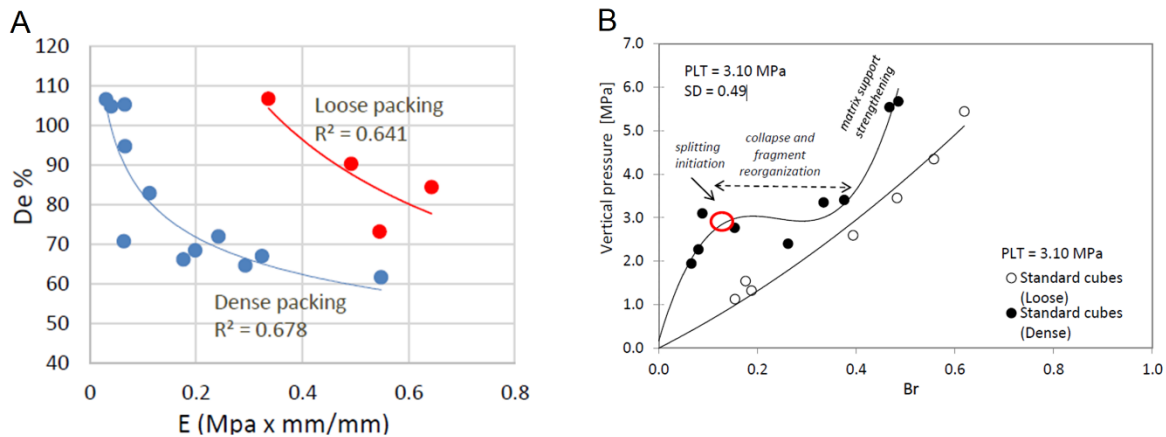

Figure 3.2 A: Initial packing effect. B: Fragmentation of dense and loose packing [88]

28

On the other hand, the fine material increases the number of contacts and reduces the probability of large rock breakage by avoiding a high concentration of load in a reduced area [215], [216]. The fine material generates a cushioning effect on the larger rock, reducing the degree of breakage. In caving mines, the fine material travels through the draw column filling the voids generated between the large rocks, and then the concentration of fine material is increased at the base of the draw column [110], [217].

3.1.1.3.Fragment shape

The geometry of the rock fragments has an impact on their breakage. An angular fragment tends to be reduced more easily than a cubic or a spherical fragment because of its singularities. In Figure 3.3, the angular particles suffer greater breakage than rounded ones for the same size and under similar stress conditions [213]. In angular fragments, the stress is concentrated at the edges of the particles, while in the rounded particles the stress is mainly concentrated at the center [212]. Additionally, the angular fragments are usually broken through abrasion (edges breaking) while the rounded fragments are mainly broken by crushing [218]. In cuboids with irregular shapes (elongated and platy), more fragmentation compared with regular cubes is observed [88] when comparing cubes and cuboids with similar strengths (PLT = 3.10 MPa).
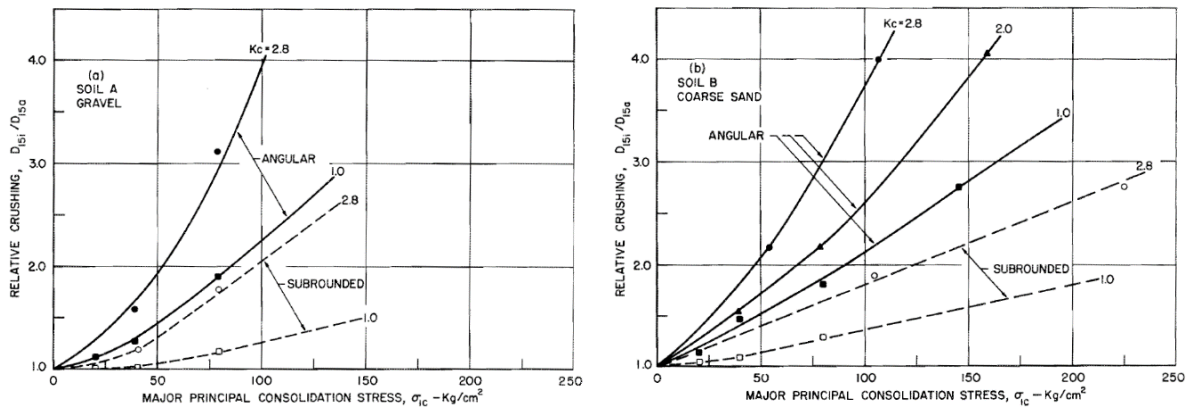
Figure 3.3 Effect of fragment shape on fragmentation [213]

During ore extraction, the rock corners are rounded, producing fine material. The amount of fine material depends on the rock angularity[219]. The rounding effect is associated with the grinding mechanism generated by the formation and collapse of coarse arches (mechanical arches) in the extraction column. Lower stress in weak rock corners can generate rounding. However, a high stress concentration generates more breakage during draw [34].

3.1.1.4.Presence of water

Triaxial tests carried out on dry and saturated granite conclude that the saturated samples present greater breakage [220] because the water enters into micro cracks and generates a pressure that facilitates the particle breakage [213], [220], [221]. Tests carried out under extraction and compression, dry and with 6% humidity, showed that only the fine material suffers fragmentation at these humidity percentages while the coarse fragments suffered less fragmentation [222], as illustrated in Figure 3.4. Verma et al. [223] reported 29 UCS tests with moisture content between 0% to 4% finding an average of strength ratio (r = UCSsat/UCSdry) r = 88%, although this ratio is reduced to 71% for moisture content between 3% and 4%.
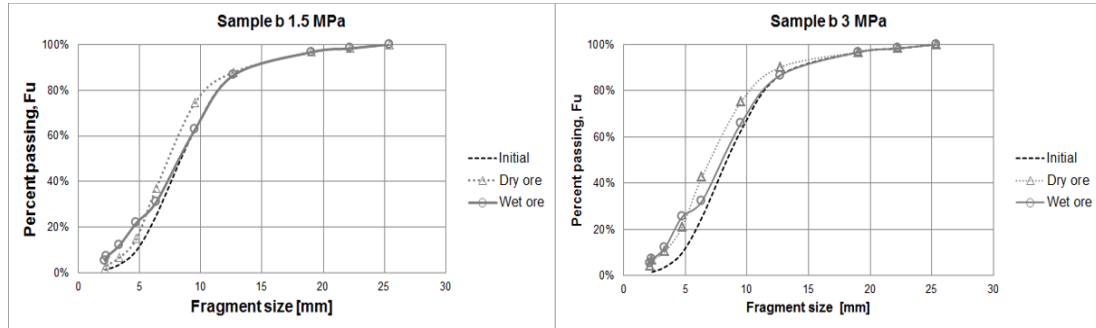
Figure 3.4 Humidity effect on rock fragmentation under draw and confined condition [222]

3.1.1.5. Draw rate

The draw rate influences the residence time of the rocks in the broken column. Under low draw rates, the rock breakage is dependent on the time in which rocks are under stress related to caving and arching [206]. The draw rate and draw strategy are mainly differentiated to avoid an early dilution entry, controlling the draw rate to maintain the waste/ore contact at a certain angle. Irregular draw should favor rock fragmentation. An experimental study [224] showed that the draw rate doesn't impact fragmentation in a setup of fragmented rock under draw and 4 MPa of vertical stress at different draw rates during 1, 2 and 10 hours (Figure 3.5).
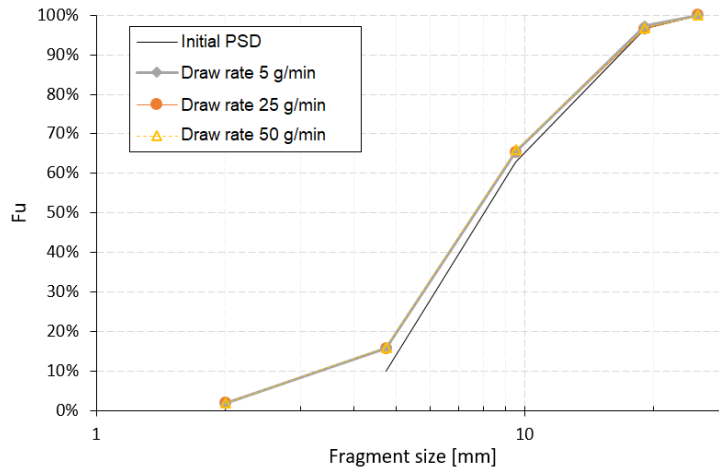
Figure 3.5 Fragmentation under different draw rate [224]

3.1.1.6. Column height

The column height influences stress due to the overload of broken material, as well as the residence time due to the distance traveled. The travel distance of fragments from their initial position can influence the degree of fragmentation. The rock fragmentation during large travel distances has been quantified in ore passes, where the mean rock size decreased by 78% after traveling 257 m [225]. In Brunswick and Kidd Creek mines, the maximum particle size was reduced by 50% after traveling 300 m of vertical distance [226]. Laubscher [40] indicates that the draw height influences on secondary fragmentation. Nevertheless, there are lack of fragmentation studies that quantified the effect of the column height on fragmentation in block caving.

The stress generated by the column height can be estimated in broken material through Janssen approach [39], [70], described in section 2.4. In particular, Pierce [59] proposed a nomogram to

estimate the vertical stress based on the extraction level depth (Figure 3.6). This nomogram was originally developed to estimate the potential damage in the extraction level.
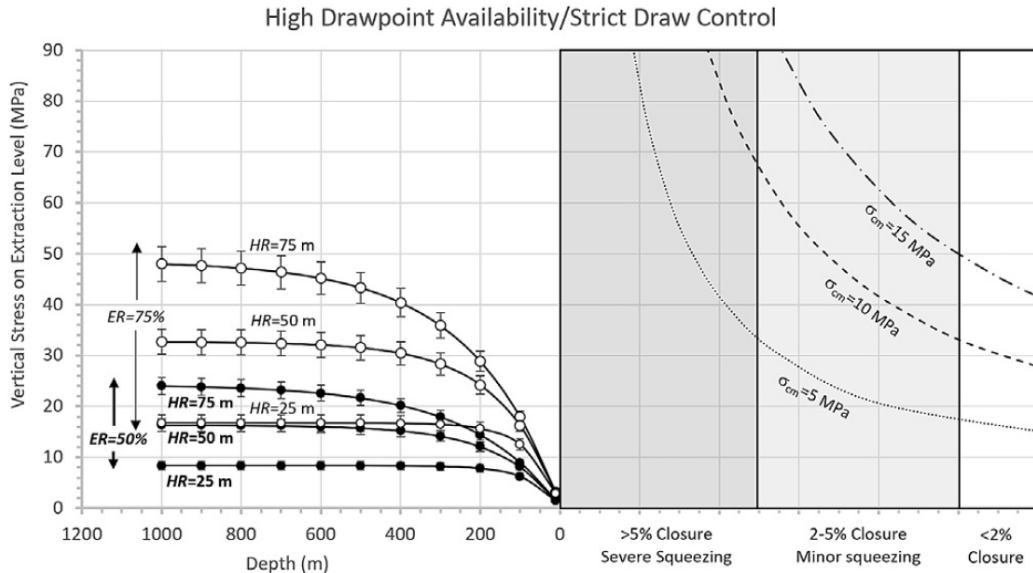
Figure 3.6 Pierce nomogram developed to estimate extraction level responded due to cave load [59].

3.1.1.7. Presence of veins

Dorador [88] studied the effect of veins on fragmentation, testing veins with different lengths and orientations in 1D compression tests. Embedded veins promote higher fragmentation, and the length does not imply noticeable differences in fragmentation. In contrast, vertical veins, aligned parallel with the 1-D loading direction, resulted in less fragmentation than veins aligned horizontally [88], [227]. In Figure 3.7, the results of veins in terms of the relative breakage are illustrated (Br [210]). Brzovic & Villaescusa [228] reported that vein thicknesses greater than 2 mm tends to significantly increase the rock fragmentation.
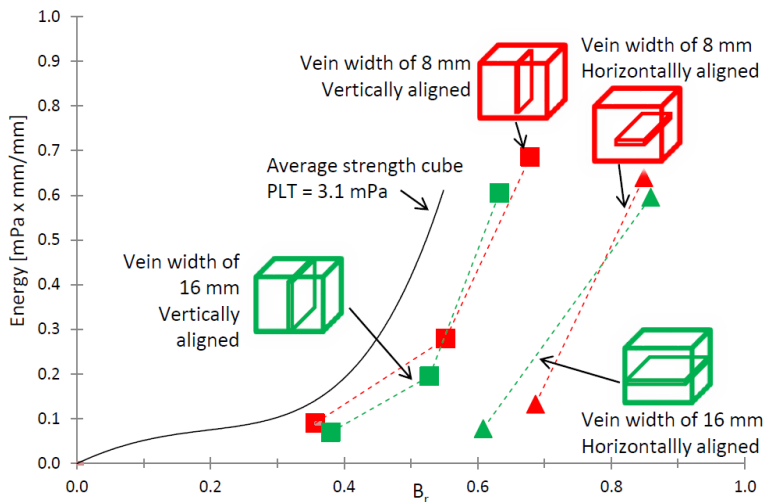
Figure 3.7 Veins effect on fragmentation [88]

31

3.2 Fragmentation prediction in block caving

One of the most used methods to estimate in-situ, primary and secondary fragmentation in Block caving operations is the Block Caving Fragmentation software (BCF [197]). BCF estimates the particle size distribution curves, using as inputs: the cavity orientation (dip and dip-dir), stress, rock mass quality (MRMR), joint orientation and joint spacing discontinuity spacing. In block caving, empirical models used to predict rock fragmentation lack a theoretical framework to explain the influence of stress compression (by overload) and shear strain, which have an evident influence on fragmentation [207]. In particular, the gravity flow model REBOP, has an empirical basis for estimated rock fragmentation based on Bridgwater et al.[108] applying the shear strain during extraction [54], [229]. On the other hand, some authors have used fragmentation mechanisms based on comminution processes to describe secondary fragmentation [205], [230]. For example, the Matrix Model is a method used to study the comminution process, which has its origin in milling processes [231]–[233]. This last model was extended to block caving, and it was calibrated through experiments during draw and stress [31]. Dorador [88] also proposes a secondary fragmentation model considering different fragmentation zones within the column and the effect of the far field and near field. Table 2 summarizes the main models used to estimate fragmentation in block caving.

Table 2 Summarized of main fragmentation models in block caving

Model	Fragmentation	Main characteristics
Size[205]	In-situ, primary and secondary.	It doesn't apply the stress field neither joints [46], [205]
El Teniente [234]	In-situ.	Three dimensional model that used 3 joint orthogonal sets [46]
BCF [197]	In-situ, primary and secondary.	It is based on empirical rules and doesn't consider stress in secondary fragmentation [197]
Chart Laubscher[40]	Primary and secondary.	It is quick and simple to use, but does not specify the data source or subsequent validations [40], [46].
JKFrag [188]	In-situ, primary.	Rock blocks are built by joint triangulation [188]
Core2Frag [204]	In-situ, primary and secondary.	It is based on information collected from drillholes (spacing and orientation) assumes fractal breakage and considers an additional generation of fine material [171], [204]
Rebop [54]	Secondary	It considers fragmentation by shear strain at MZ boundaries and by compression in stagnant zones [54]. It has also been applied in a hybrid methodology [207].
FracMan [235]	In-situ, primary and secondary.	It uses DFN, with the P32 as the key variable in early fragmentation stages. The secondary fragmentation model is based on the generation and fragmentation of veins [198], [235]
Dorador [88]	Secondary	It is based on the subdivision of zones of near field and far field in the extraction column, proposed by Pierce [54]
BCCM [31]	Secondary	It is based on experimental tests, considering compression and abrasion during draw under overload[31]. It has shown good correlation compared with data from El Teniente.
Castillo [236]	In-situ, primary and secondary.	This methodology applied the Laubscher methodology for in-situ and primary fragmentation[38] also including the preconditioning and blasting during undercutting.

Additionally, there are examples of the combination of these models. In DOZ mine, Core2frag was used to estimate primary fragmentation while BCF was used to estimate secondary fragmentation [204]. This estimation obtained good results in medium and large rock sizes (d_{50} and d_{80}), but it underestimated fine material.

3.3 Hang-ups: Coarse arches

In the extraction level, hang-ups and oversize rocks are critical operational problems in block caving. The largest number of hang-ups and oversize rocks at drawpoints come from block caving mines in competent ore bodies, during the caving breakthrough. Both phenomena interfere with the production by disabling the drawpoint and closing mining areas to hang-up removal and/or secondary breakage. The hang-ups at drawpoints generate irregular ore extraction, which can lead to fine material migration [112]. Additionally, this irregular extraction could also cause mud-rush, inrush of fine material and stress transmission. In Figure 3.8, the effect of the uniformity index on the hang-up index is shown.
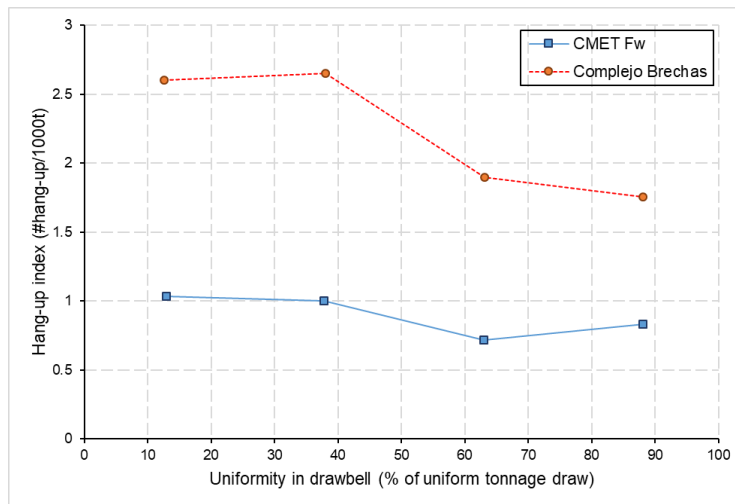
Figure 3.8 Hang-ups based on uniformity of draw [237]

Several studies have been carried out to quantify the effect of different variables on hang-ups, mainly through physical models [34], [84], [89], [238]–[240]. In these studies, the effect of PSD, stress, fine material, humidity and drawbell geometry have been analyzed. Also, other studies have used the back analysis of field data [45], [48], [83], [241]–[244]. Moreover, Brzovic et al. [243] proposes a predictive model to estimate oversize rocks based on the P32, the extracted height and the height of primary material.

Two types of hang-ups can be distinguished [41], [83], [245]: those formed by mechanical arches and those formed by the presence of cohesive material. The mechanical arches are generated by the rotation of the main stresses on rough walls [210], producing triangular stress distributions in the wall which make a stable structure. The main variables involved in the generation of hang-up events are [38], [41], [84], [240], [246]:

- Ratio between the drawbell volume and fragment volume

- Stress magnitude and distribution
- Fragment size distribution
- Geometry of drawbell and drawpoint
- Friction, Cohesion, roughness and shape factor of fragments
- Rock strength
- Fine material and presence of humidity
- Draw rate and draw strategies

The ratio between the drawpoint width and the fragment size is a key variable that influences hang-ups. In hang-ups of coarse arches, the ratio between the maximum particle diameter (d) and the opening width (D) is used to determine the flow condition. Various authors have defined a ratio D/d as is shown in Figure 3.9. These ratios determined from tests on silos and ore passes, define the importance between the ratio D/d, which could be extrapolated to drawpoints in block caving.
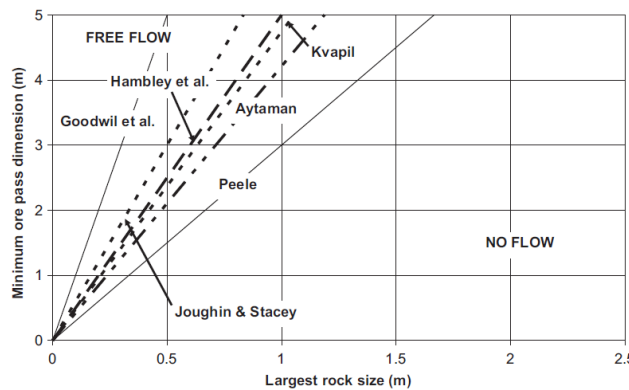
Figure 3.9 Granular material flowability based on ore passes studies [83]

Additionally, the ratio between the drawbell length or volume and the fragment size influence on hang-up events [240], as is indicated in Figure 3.10. The geometrical parameter between the drawbell and the fragments are relevant in gravity flow, but it has also been observed that the confinement strongly influences hang-ups [34], [84].
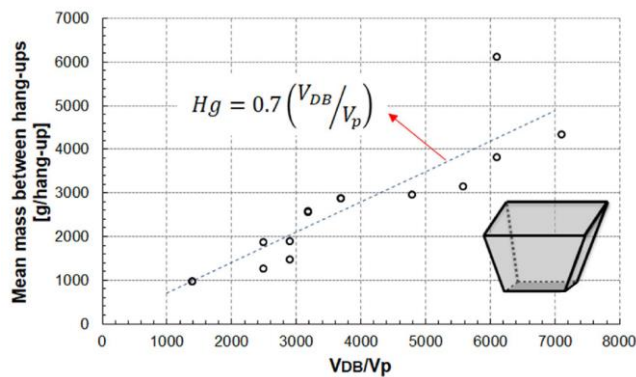
Figure 3.10 Hang-up frequency based on the volume ratio, between the drawbell and the rock fragments [240]

Tests carried out in physical models [41] and the empirical evidence [247], indicate that hang-ups can occur at any height above the extraction level in the flow zone. The sudden failure of large coarse arches on drawpoints can imply an air blast, causing serious damage to the mine sector. The quantification of hang-ups is an indirect way to observe fragmentation during the extraction.

3.3.1 Mine operational problems

Hang-ups involve various operation issues due to the ore flow interference. Consequently, hang-ups generate stagnant zones in the draw column, implying non-uniform draw as well as interventions in the drifts or areas in the extraction level to remove the hang-up. These interventions and the required secondary breakage have a great impact on draw rates [248]. In Premier mine South Africa, it was reported that hang-ups caused 66% of the drawpoints to be unavailable [249]. Additionally, Lopez & Castro [237] reported a significant impact of hang-ups on drawpoint availability in Esmeralda, El Teniente mine, Chile. Carrasco et al. [250] indicate that hang-ups should be included in planning stages. However, Ovalle [251] indicates that when caving breaks through to the surface, the hang-ups aren't the main constraint on productivity.

Hang-ups and oversize rocks are frequent at the beginning of ore extraction due to coarse fragmentation [45], [48], [247], [252], [253]. This suggests the use of high undercutting to improve productivity at the beginning stages [254]. Nevertheless, the rock mass fracture during caving depends basically on the open area and the rock mass strength [40]. Later, the hang-up events decrease as the extraction progresses due to the decrease in rock sizes. In more advanced caving stages, the hang-ups increased their height [247], which implies more complex removal tasks.

### 3.2.3 Hang-up detection

Hang-ups are commonly detected by visual observation; however, other hang-up-detection methods exist such as laser detection, radar, microwave reflection and ultrasound [245], [255]. Hang-up removal mechanisms can be classified as breakage or mechanical release [83], [247], [256]. For removal by breakage, explosives are often manually positioned using an adhesive patch in some rock fragment of the hang-up (using a bamboo or a bamboo-column [256]). A mechanized arm can also be utilized to place explosives and avoid worker risk [255], [257]. Other hang-up removal methodologies include firing a projectile and using a water cannon, all developed mainly to avoid worker exposure to hang-up risks [245], [247], [258], [259].

Before removing a hang-up, it is recommended to wait a certain period of time to stabilize the arch [260]. Some properties of the rock may facilitate natural hang-up removal. For example, a low friction angle facilitates material flow that can imply arch collapse [38]. Natural hang-up removal can also occur by extraction from the neighboring drawpoint of the same drawbell, as has been observed in physical models [84], [240].

The technique most used to remove hang-ups at drawpoints is the secondary breakage by blasting, which has proven to be an efficient and effective technique [247]. Although for high hang-ups, specialized equipment is required. In this cases, an explosive package is adhered to the hang-up without drilling. The explosive methods used to remove hang-ups are not recommended for cohesive

hang-ups, because blasting can cause greater adhesion and compaction of the material to be removed. Moreover, the cohesive arches can also be a potential hazard of mud runoff [254].

4 Summary of the literature review

Nowadays, there are physical and numerical models that simulate the gravity flow of fragmented material, as well as various fragmentation models applied to block caving. However, the interaction between the gravity flow and the rock fragmentation during ore draw haven't been modeled quickly and precisely.

During caving, rock fragmentation continually varies. Therefore, the rock size estimation depends on the caving stage, so the period in which the analysis is being considered must be defined. Hence, it is logical to ask the following questions due to the rock size evolution over time: What size distribution should be used to define the optimal extraction level design and equipment? Can an isolated draw be generated if the rock size decreases considerably over time? How does the fine material migration influence the flow zone geometries? How does the stress in the broken column affect the gravity flow and rock fragmentation? In order to address these and other questions, the present study in Block Caving is being carried out.

In this work, different studies are proposed in rock fragmentation and gravity flow to complement the understanding of block caving. Here, a secondary fragmentation model is analyzed under various rock types and travel distance to study the fragmentation in the broken column during draw. Additionally, the stress in the broken column influences during gravity flow and rock fragmentation. However, it is difficult to estimates the stresses in the broken column at mines scale during draw. Here, draw strategies are studied and its influence on induced stresses in the broken column. Then, this results are used to develop a numerical stress model for block caving environment. Finally, the fragmentation model, as well as the stress model are applied in a gravity flow simulator in which the rock size is a variable that influences gravity flow modeling. Thus, in a gravity flow simulator based on cellular automata, the effects of rock fragmentation, stress and rock type that take placed during ore draw in block caving are integrated.

5 Papers

The following articles were elaborated during this thesis:

5.1 Paper 1: *Comparison of normalized and non-normalized Block Caving Comminution Models.*
http://dx.doi.org/10.17159/2411-9717/1150/2021
Published in The Southern African Institute of Mining and Metallurgy.

This paper study the rock strength effect in a secondary fragmentation model. Additionally, defined the used of the normalized comminution model to block caving application.

5.2 Paper 2: *Experimental quantification of granular material fragmentation due to travel distance.*
https://doi.org/10.1007/s42461-022-00545-9
Published in Mining, Metallurgy & Exploration journal.

This paper analyzed the granular material fragmentation at different travel distances and the results are included in the previous secondary fragmentation model at mine scale.

5.3 Paper 3: *Experimental quantification of vertical pressures during gravity flow in block caving.*
https://doi.org/10.1016/j.ijrmms.2020.104237
Published in International Journal of Rock Mechanics and Mining Sciences.

This paper study the vertical stress induced in granular material due to ore draw, at laboratory scale. Here, different draw strategies are analyzed in terms of vertical stress distribution.

5.4 Paper 4: *Stress modelling using cellular automata for block caving application.*
https://doi.org/10.1016/j.ijrmms.2022.105124
Published in The International Journal of Rock Mechanics and Mining Sciences.

In this paper is presented a vertical stress model of granular material in cellular automata. The vertical stress model is calibrated using experimental data from paper 3.

5.5 Paper 5: *Fine material migration modelled by cellular automata.*
https://doi.org/10.1007/s10035-021-01173-8
Published in Granular Matter.

This paper summarized previous works and introduced a fine material migration model based on cellular automata. The migration model used the d_{50} as a key variable. This variable is modified due

to secondary fragmentation, based on papers 1 and 2. This size reduction also included the vertical stress estimated based on paper 3 and 4.

Paper 1: Comparison of normalized and non-normalized Block Caving Comminution Models

Gómez R, Castro R, Betancourt F, Moncada M.

Abstract

In block cave mining, rock fragmentation is a key parameter that influences the production level design and mine planning. Fragmentation is produced mainly by natural breakage during the caving process and in the draw column. In particular, the breakage that occurs within broken columns is known as secondary fragmentation. Secondary fragmentation has been successfully described using the Block Caving Comminution Model, which replicates the fragmentation mechanics between particles under drawn and vertical loads in a draw column. This model is based on a kinetic and population balance approach, in which non-normalized and normalized assumptions can be used depending on material and comminution system behavior. In this paper, the non-normalized and normalized approaches are applied and compared to laboratory data to determine which assumption should be used for a secondary breakage process in block caving. Approaches are compared graphically, with the mean square error and the Fisher Test with a false-rejection probability of 0.05. Based on a statistical analysis, results show that the normalized model can be applied to all the rock types tested.

Keywords: Block caving, breakage, comminution, population mass balance, rock, secondary fragmentation.

1 Introduction

The Block Caving method has been widely used in the mining industry for over 30 years. In this process, 3 stages can be identified: in-situ fragmentation, primary and secondary fragmentation. The rock size obtained after the secondary fragmentation has a strong influence on design stages, ore extraction and haulage, and mineral processing [40], [188], [192], [206]. Particularly, in cave mining, the process is also influenced by the geometry of draw zones that defines the drawpoint spacing, draw control, rate of draw and secondary breakage [40], [252]. During ore draw, the rock fragment size can generate operational problems such as hang-ups, oversized material, fine material migration, inrush of fines and mud-rush events. These are some of the main reasons to study and estimate the rock fragmentation in block caving mines.

During block caving, fragmentation of the ore column is produced mainly by natural breakage induced by mining or by blasting applied in the base of the ore column from the undercut level or production level [261]. Additionally, preconditioning can be used to create new fractures or expand existing ones by hydraulic fracturing, confined blasting, or both. However, the major rock fragmentation of the rock ore occurs during caving and ore draw. Of the three well-accepted fragmentation stages, in-situ fragmentation is the natural fragmentation in the rock mass previous to mining activity that can be modified using preconditioning [243]. Primary fragmentation occurs during caving where the rock around the cave back is fragmented and then falls. Secondary fragmentation occurs in the broken column during draw and is the last stage of fragmentation before drawpoint extraction. Here the rock is mainly fragmented due to compression and abrasion (splitting and attrition). Some authors also include impact fragmentation, which is highly influenced by the air gap height, as a mechanism of secondary fragmentation [88], [192], [206], [207].

The breakage of the granular material under stress depends on various factors such as particle size distribution (PSD), particle shape, state and trajectory of effective stresses, void ratio, material strength, presence of water, and extraction rate, among others [192], [262], [263]. Among these factors, strength is one of the most relevant. Low rock strength implies early breakage of the rock block under a stress arch [38]. Conversely, increasing strength decreases the amount of fragment breakage during a given stress [212]. Similarly, for an individual block, it is well known that strength decreases as size increases [171], [264], and particularly in block caving, where the presence of large volumes of rock is common, rock strength is a consequence of the intact rock

strength, the presence of discontinuities, and the deformation capacity [171]. In 2016, Dorador [88] observed that rock strength has more influence on fragmentation than parameters such as shape and size distribution. On the other hand, it has been reported that the strength ratio between large and small blocks plays an important role in crushing [214], [215]. Furthermore, strength has been shown to decrease in the presence of moisture as seen during crushing tests on individual particles [265]. An explanation for this phenomenon is that the infiltration of water in microcracks increases the pressure on the rock facilitating its rupture [213], [220], [221].

In terms of material shape, angular particles suffer greater breakage than rounded or cubic ones of equal size and under similar levels of stress [88], [213]. This behavior is explained by the load concentration in small areas of the particles, increasing the stress and facilitating its fracture [212]. Another possible explanation is that this occurs because angular particles fracture preferentially by the abrasion mechanism (breaking of the edges) while the rounded ones by compression, presenting a greater apparent resistance [218].

Breakage is also affected by fine material transported through the extraction column using the voids generated between the larger blocks with fines more concentrated towards the base of the mineral column [110], [211]. This fine material generates a cushioning effect on the coarse material, thus reducing the degree of breakage [192]. Such phenomenon occurs because the presence of fine material prevents direct contact between coarse blocks, increasing the number of contacts and reducing their probability of breakage by avoiding a high concentration of stresses in a reduced area of the block [216].

The extraction rate determines the residence time of the block in the column of broken material. Increasing the extraction rate decreases the magnitude of the shear stresses, thus reducing fragmentation [266]. At low extraction rates, the fracture of the material depends on the effective time in which it is under stresses associated with caving and/or under arc conditions [206]. Another relevant aspect in fragmentation is the material transport through the ore pass. The impact of the distance traveled has been quantified during transfer through the ore pass, where the average size d_{50} has decreased by 78% after traveling 257 m [225]. A similar result was obtained in Brunswick and Kidd Creek mines where the maximum particle size was reduced by 50% after traveling 300 m of vertical distance [226].

There are various models that estimate the fragmentation in block caving in particular the secondary fragmentation reported as the final fragmentation at drawpoint (e.g: [31], [54], [88], [197], [198], [204], [205]). The Block Cave Fragmentation (BCF [197]) is probably the most used in the industry. This approach estimates primary and secondary fragmentation based on empirical rules. The REBOP (Rapid Emulation based on PFC) secondary Fragmentation model is based on Bridgewater's attrition model [108]. Srinkant and Rachmandl [267] mixed CoreFrag2 to estimate primary fragmentation, and BCF for secondary fragmentation, obtaining good results in medium and coarse sizes (d_{50} and d_{80}). Dorador [88] divided the broken column in a far field, characterized by a plug flow, and a near field, characterized by a mixed flow to estimate secondary fragmentation. In the Block Caving Comminution Model [31], the rock flow is simulated considering compression and abrasion, the main fragmentation mechanisms during secondary fragmentation and it is validated through experiments. In this work we extend the model performed by Gómez et al. [31], by studying a hypothesis about the model and by performing experiments with different types of rock. In the Appendix section, an example is shown in which the extended model is applied to real data.

2 Block Caving Comminution Model

The Block caving method is widely used in massive underground mining because of the associated high production rates and low operational costs. With this method, rock fragmentation occurs naturally during ore extraction while caving propagates to the surface. Thus, fragmentation in this method is mainly determined by rock mass properties, stress fields and draw policies. Here we focus our analysis on a model used to estimate the secondary fragmentation presented as the Block Caving Comminution Model (BCCM [31]).

The BCCM in its batch version is determined by the following mass conservation equation:

$$\frac{df_i(t)}{dt} = -S_i f_i(t) + \sum_{j=1}^{i-1} b_{ij} S_j \qquad [1]$$

Where f_i is the solid mass fraction of size interval i, S_i is breakage velocity of the ith interval, and b_{ij} is the breakage function and represents the fraction of the primary breakage product of material in the jth interval, which appears in the ith interval after fragmentation. The extraction process in Block Caving is a continuous process that is usually modeled by a plug flow. Then, incorporating this plug flow assumption in Equation [1] and using the Reid solution for the batch population balance [268], we get

$$m_i = \sum_{j=1}^{i} A_{ij} e^{-S_j \tau} \qquad [2]$$

where m_i is the mass in the ith interval, τ is the residence time and A_{ij} is given by

$$A_{ij} = \begin{cases} 0 & \text{if } i < j \\ f_{i0} - \sum_{k=1}^{i-1} A_{ik} & \text{if } i = j \\ \sum_{k=j}^{i-1} \frac{b_{ik} S_k}{S_i - S_j} A_{kj} & \text{if } i > j \end{cases} \qquad [3]$$

where is the initial particle-size distribution.

In order to compute Equation [2], it is necessary to know the values of the functions B_{ij} and S_j. The common way to determine these functions is by assuming a constitutive parametric form and performing a back calculation from experimental data [269]. In this work we consider for S_j the parametric expression proposed by Herbst and Fuertenau [270] and later modified by Gómez et al. [31]:

$$S_j = S_1 exp\left\{ Z_1 ln\left(\frac{d_i}{d_1}\right) + Z_2 \left[ln\left(\frac{d_i}{d_1}\right)\right]^2 \right\} \sigma_v \qquad [4]$$

Here Z_1 and Z_2 are parameters depending on the material properties, and σ_v is a variable that represents the mean vertical load. It is common to use the cumulative fraction of breakage product $B_{ij} = \sum_{k=i}^{n} b_{kj}$ (instead of b_{ij}) as $b_{ij} = B_{i,j} - B_{i+1,j}$, the so-called *Normalized* expression for $B_{i,j}$ is given by

$$B_{i1} = \alpha_1 \left(\frac{x_i}{x_2}\right)^{\alpha_2} + (1 - \alpha_1)\left(\frac{x_i}{x_2}\right)^{\alpha_3} \qquad [5]$$

where α_1, α_2 and α_3 are model parameters ($0 < \alpha_1 < 1; \alpha_2 < \alpha_3$) and x_i is the mesh size for the ith interval and x_2, which corresponds to the second mesh size interval, is the normalizing parameter. We remark that in the

normalized expression Equation [5], it is assumed that all particles have a rupture distribution with dimensional similarity.

The *non-normalized model* raises this hypothesis, and is given by the expression [271]:

$$B_{ij} = \alpha_j \left(\frac{x_i}{x_j}\right)^{\alpha_2} + (1 - \alpha_j)\left(\frac{x_i}{x_j}\right)^{\alpha_3} \qquad [6]$$

where

$$\alpha_j = \alpha_1 \left(\frac{x_j}{x_1}\right)^{-\delta} \qquad [7]$$

and δ is a new parameter to be adjusted ($\delta > 0$) for $0 < \alpha_j < 1$.

For $i>j$, it must be noted that the *normalized* expression presented in Equation [5] is a simplified case of Equation [6] when $\delta = 0$ and $x_j = x_2$. According to the constitutive expressions selected in this work, the back calculation method yields a nonlinear optimization problem with 6 parameters (S_1^E, Z_1, Z_2, α_1, α_2, α_3) in the *normalized framework* and 7 parameters (S_1^E, Z_1, Z_2, α_1, α_2, α_3 δ) in the *non-normalized framework*.

In milling processes, normalized models are typically suitable [272], but in the Block Caving process, the normalization of the model has not been studied. The aim of this paper to compare the normalized and non-normalized model using statistical analysis of a variety of rock types to identify which approach should be used with block caving methods.

3 Methodology

3.1 Laboratory Setup

The confined-flow-model setup consisted of a steel cylinder able to retain rock fragments while vertical pressure was applied through a hydraulic press machine. The model geometry consisted of an inside diameter of 0.34 m, height of 0.70 m and steel width contour of 0.03 m. Here fragmented material was drawn from a drawbell at the bottom, emulating a block caving mine extraction system using a scaled LHD to draw the material. A constant vertical pressure was applied in each test.

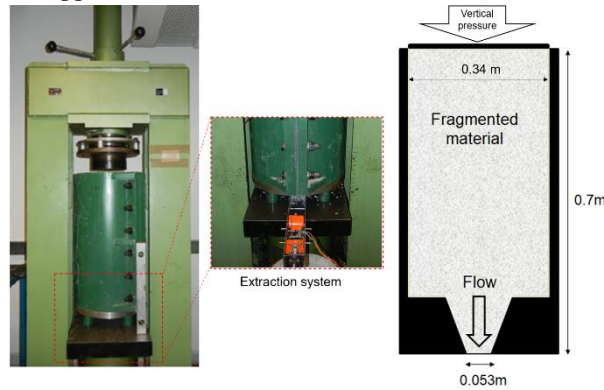**Figure 1 Confined flow system used In fragmentation tests (Left [31], Gómez et al. 2017) and a side view inside the model (right)**

Material was drawn from the bottom until its flow reached the top of the fragmented material (around 10 percent of the total fragmented material in over two hours). Then all material was homogenized, and the fragment size distribution was measured by sieving.

3.2 Mineral Materials

Four rock types were tested in the same confined flow system. Table 1 shows the rock density, IS,50 (point load index) and internal friction angle obtained through standard laboratory tests. Sphericity and roundness are determined using the methodology proposed by Cho et al. [273].

Table 1. Rock characteristic summary

Rock Type	Density [t/m^3]	Is,$_{50}$ [Mpa]	Sphericity	Roundness	Friction angle [°]
A	2.62	5.93	0.58	0.25	39
B	2.60	1.25	0.68	0.22	40
C	2.71	1.64	0.68	0.20	37
D	2.69	6.93	0.65	0.51	48

A: Primary sulfide composed of biotite and amphibole granitoid ore from Antofagasta, Chile.
B: Primary sulfide composed mainly of sericite ore from Calama, Chile.
C: Primary sulfide composed of quartz and sericite ore from Calama, Chile.
D: Gravel, quarry from Santiago, Chile.

3.3 Tests and data fitting

The four previously described materials with different initial size distribution curves were used with constant vertical pressures applied during the comminution tests:

- Rock type A (MPa): 0.8, 1.5, 3, 5.
- Rock type B (MPa): 2.
- Rock type C (MPa): 1, 2.
- Rock type D (MPa): 1, 1.5, 3, 6.

The *normalized* and *non-normalized* model parameters were adjusted using the fragment size distribution curves from the comminution tests. The trust-region-reflective least squares algorithm was used to obtain the model parameters [274], minimizing the square difference between experimental and modeled data.

$$min \sum_{j=1}^{m} \sum_{i=1}^{n} \left(f_{ij,exp} - f_{ij,mod} \right)^2 \qquad [8]$$

where $f_{ij,exp}$ and $f_{ij,mod}$ are the experimental and modeled mass fraction of size interval i at pressure j respectively. We note that the *non-normalized* case includes the δ parameter with the constraints ($\delta > 0$) for $0 < \alpha_j < 1$.

In order to evaluate if the addition of the parameter δ is relevant, an F test was performed. The null hypothesis is the *normalized* model with $\delta = 0$ is nearly equal to the *non-normalized* model with $\delta > 0$. The F value was calculated using Equation [9],

$$F = \frac{\frac{MSE_{\delta=0} - MSE_{\delta>0}}{k}}{\frac{MSE_{\delta>0}}{N-M}} \qquad [9]$$

where *MSE* is the mean square error, k is the number of conditions (here $\delta = 0$), N is the number of data points and M is the number of parameters of the model i.

4. Results

In this section we present the results of the parameter identification for the normalized and non-normalized approaches, the selection and breakage functions, and the Fisher test. In the Appendix section the full experimental data can be found.

4.1 Fitted Parameters

The *non-normalize*d model parameters obtained for each rock type are summarized in Table 3. In all cases the residence time τ is kept constant and equals the average residence time of the tests ($\sim 0.1\ day$).

Table 3. Normalized and non-normalized model parameters

Model	Rock type	τ	S_1^E	Z_1	Z_2	α_1	α_2	α_3	δ
Normalized	A	0.1	0.002	-19.521	-13.637	0.810	0.968	1.780	0.000
	B	0.1	0.744	-3.139	-2.310	0.098	0.569	0.779	0.000
	C	0.1	2.518	-1.762	-3.290	0.048	0.739	0.828	0.000
	D	0.1	0.190	-10.373	-14.080	0.859	0.588	0.598	0.000
Non-normalized	A	0.1	0.002	-19.517	-13.635	0.810	1.050	1.060	0.079
	B	0.1	0.744	-3.139	-2.310	0.467	0.779	0.789	0.096
	C	0.1	2.518	-1.763	-3.290	0.048	0.680	0.690	0.830
	D	0.1	0.182	-10.567	-14.265	0.683	0.588	0.598	0.102

In general, the *non-normalized* and *normalized* model parameters do not present significant differences: for example, rock types A and C present the same α1. These similarities between the models are also observed in the selection and breakage functions as shown in Figures 2 and 3.

4.2 Selection and breakage functions

Figure 2 shows the rate of breakage (S_i^E), and Figure 3 shows the breakage functions (B_{ij}) of different rock types: A, B, C and D.
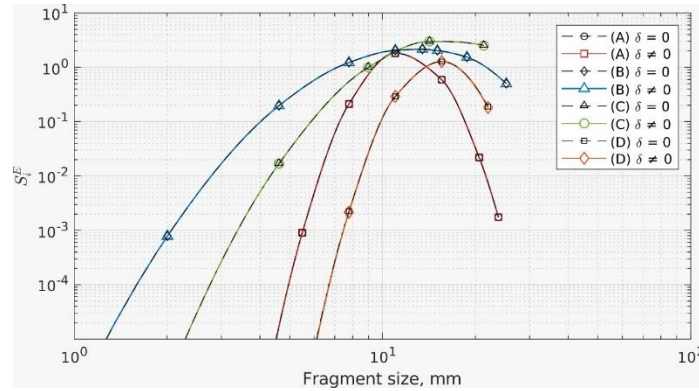
Figure 2 Selection functions

The influence on the rate of breakage of fragment sizes when modelling with $\delta = 0$ is not significant. Thus, α_i (Equation [7]) could be assumed constant depending on fragment size. This is also noticed in the breakage function in Figure 3 for $\delta > 0$, where for each rock type data point, the breakage functions follow the same resulting fragment size distribution, independent of initial fragment size (as modeled by the normalized BCCM presented in Gómez et al. [31]).
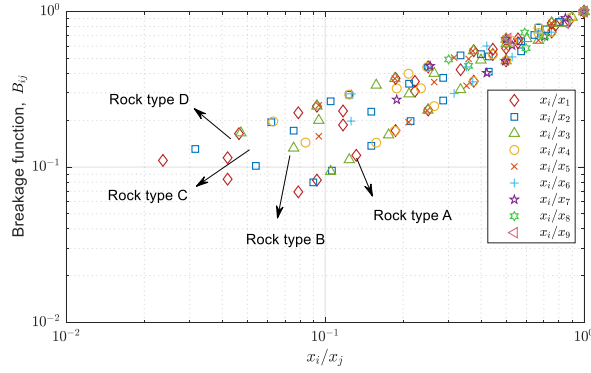
Figure 3 Breakage functions

4.3 Fisher test performed

Using a false-rejection probability of 0.05, the critical values of the F-distribution are presented in Table 4. Here, all the F values are lower than the respective critical values; therefore, the use of the simplified *normalized* model is recommended in these cases.

Table 4. Mean square error and F-test results

Rock type	MSE $\delta = 0$ (%^{2})	MSE $\delta > 0$ (%^{2})	F critical	F
A	10.62	10.35	3.97	2.01
B	2.49	2.46	18.51	0.03
C	1.03	0.96	6.61	0.27
D	3.44	3.43	3.98	0.22

5 Conclusions

The literature indicates that in milling systems the normalized model (Equation [5]) can be applied in almost all the cases; however, this assumption cannot be considered a priori in the Block Caving method since the mechanism of breakage differs from the milling process. The non-normalized model implies that in the breakage function, *Bij*, the resulting fragment-size distribution depends on the original fragment size. According to the experiments and parameter fitting, we found that the resulting fragment-size distribution is independent of the initial fragment sizes. Thus, for the materials and confined flow system examined here a simplified normalized model should be used, independent of the material.

It must be noted that abrasion and compression are the fragmentation mechanisms observed in the experiments, but compression is probably the dominant mechanism; this mechanism generates a narrow particle size distribution with low relative sizes of fine and large particles, which we speculate explains the results of this work. It is well known that the stress over the rock depends on the height at which it is located. In the present model, this stress is supposed to be constant throughout the column, which can lead to differences with respect to experimental data. In a later work, we will extend the present model by incorporating this dependence into the governing equations.

Appendix A: BCCM Applications

First, it is necessary to determine the parameters of the model (S_1^E, Z_1, Z_2, α_1, α_2, α_3) to apply the BCCM, by making an adjustment from experimental laboratory tests. Subsequently, it is possible to solve the governing equations of the model if we know the input curve (primary fragmentation), physical characteristics of the column, and the operational conditions.

The model was evaluated for 5 reported mine cases. The first fragmentation reported is considered as the primary fragmentation. The laboratory calibration parameters of the rock type A (Table 4) were used, which has a rock strength similar to the selected mine cases. The mean vertical stress in the broken column was estimated through the Janssen equation [142].

Table 5. Mine cases.

Mine-sector	Intact rock strength, MPA	Vertical load, MPa	Draw Height primary frag.
DOZ-Diorite [252]	111	3.2	Unknown
Esmeralda-B2 [31]	100-130	2.2	0-20 m
Reno-HW [31]	115	2.5	0-50 m
Teniente 4 Sur [45]	125	4.4	0-50 m
Ridgeway (Volcanic) [190]	130	3.5	0-25 m

The fragmentation rate is scaled with respect to laboratory experiments so that

$\tau_i S_i(lab) = \tau_i S_i(mine) = constant$	[10]

The residence time for all cases was estimated using

$$\tau = \frac{HA\rho}{D_r}$$	[11]

The results obtained using the residence time calculated by the previous equation show that the model overestimates the rock fracture. This behavior had already been reported in Gómez et al. [31]. These differences can be explained due to 3 reasons: i) the material suffers the greatest fractures at the beginning of the process; ii) the vertical forces are usually low close to the movement zones iii) the draw rate and vertical force is dependent on the height of the column, which changes over time. Figure 4 shows the results considering a residence time between 1.5 and 3.7% of that calculated by Equation [11]. In this case, the data provided by the model fit well to the real data of the cases studied.
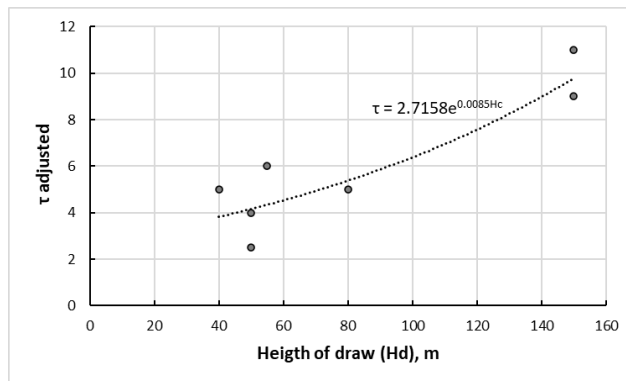
Figure 4 Residence time based on study cases

Figure 5 shows the fragmentation results using the model considering the real residence time (Equation [11], blue points in Figure) and the adjusted residence time (red squares in Figure). Importantly, we need to use a shorter residence time to obtain a good fitting. Also, the effect of the higher extraction height of the same mine can be observed in Figure 5 C and D and Figure 5 E and F.
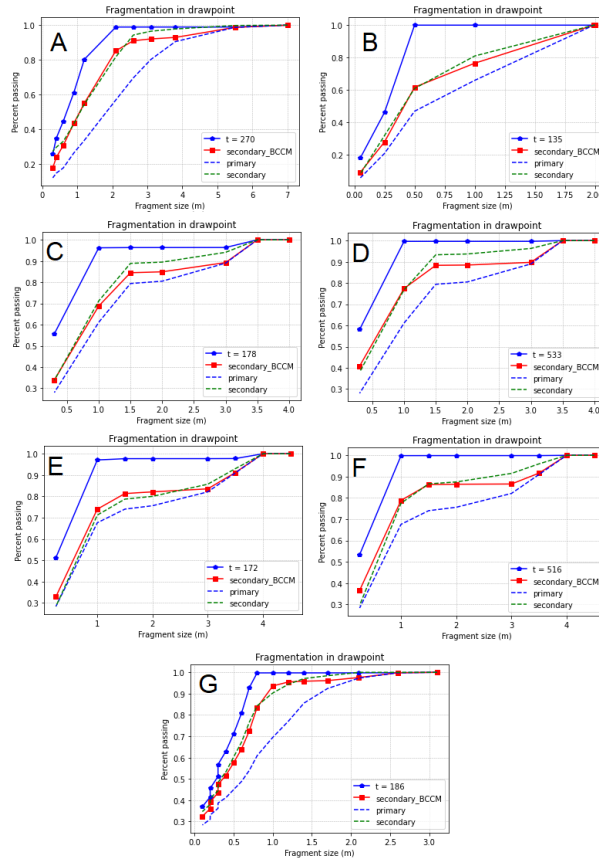
Figure 5 Estimation using BCCM at mine scale. A: DOZ-Diorite. B: eSMERALDA-B2, SECONDARY (0-60m). C: reno-hw, secondary (0-100 m). d: reno-hw, secondary (0-200 m). E: Teniente 4sur, secondary (0-100 m). f: Teniente 4sur, secondary (0-200 m). g: ridgeway-volcanic, secondary (0-75 m)

Paper 2: Experimental quantification of granular material fragmentation due to travel distance

René Gómez, Raúl Castro

Abstract

In underground mining, rock fragment size is a key variable for productivity because it impacts equipment selection and mining structure design, such as for drawbells and ore passes. During ore flow, those structures are usually affected by interferences such as hang-ups and issues associated with oversized rocks or fine materials. Fine materials could imply problems with mudrush and/or inrush of fines. The rock fragment sizes must be estimated, in particular, in block caving where fragmentation develops naturally while the broken ore is being drawn. Nowadays, estimation tools and models are available to estimate fragmentation, but some variables have yet to be studied to understand their effect on the fragmentation process. One such variable whose mechanisms have yet to be studied is the residence time, which in block caving directly depends on the distance that fragments travel from their original position in the broken ore to the drawpoint. A greater degree of fragmentation is expected for longer distances. In this study, granular material fragmentation was characterized during its flow to understand its characteristics and mechanisms. Tests were done using a laboratory setup built to emulate various heights where material is drawn. The fragment-size distribution was measured before and after tests for clay, concrete fragments, and gravel. It was found that for six meters of travel distance, fragmentation mainly occurs in minor sizes where d_{10} decreases by 4.7% for gravel, 6.2% for concrete and by 63.1% for clay. The breakage of fragment singularities occurred mainly within medium and smaller sizes, increasing fine material. Thus, the main fragmentation mechanism in experiments was identified as abrasion between rock fragments where fine material continuously increases as distance increases in spite of the high rock strength and the piston flow movement used. Then, in block caving mines, the higher the draw column, the more fine material is expected to be generated.

Key word: Rock, Fragmentation, Granular material, Mining, abrasion.

1. Introduction

In block caving, the rock fragment size is one of the parameters that defines the mine design, the equipment selection, and productivity [40], [275], [276]. Mining structures and equipment must be capable of managing a variety of fragment sizes. The material must flow through the mining structures minimizing interferences, such as hang-ups, while the equipment must be able to load this material. Fragment sizes that appear at production level must be accurately estimated to minimize issues that can halt production.

Different mechanisms influence rock fragmentation of particle aggregates. In particular, fragmentation in block caving that occurs in the broken ore is mainly generated by autogenous grinding between rock fragments during draw [192]. Abrasion and compression have been reported as the main fragmentation mechanisms due to draw under load [31]. Abrasion is the main breakage mechanism under low shear stress [54] and occurs when the energy applied on a fragment is lower than rock strength, but enough to break fragment singularities to thus generate fine material. The fine material cushions large fragments in a particle aggregate because stresses are distributed over more contact points between fragments [40], [277], decreasing fragmentation by compression.

The amount of rock fragmentation is highly dependent on the rock strength and the field stress. A high rock strength implies poor degree of fragmentation for different field stresses [278]. It is also known that rock strength is related to fragment size, such that larger-sized rocks have less strength than smaller-sized fragments [209], [262]. Additionally, other variables also influence rock fragmentation such as the particle shape, the amount of particle-to-particle contact in a particle aggregation [277], the particle gradation [279], the particle aggregate porosity, the rate of draw and the travel distance.

Some studies have attempted to observe the effect of these variables on fragmentation. For example, an angular fragment is broken more easily than a cubic or a spherical fragment because of its singularities [213]. In spherical fragments, the stresses are accumulated in the center [212]. Angular fragments can be round due to shear stress when fragments are under flow, generating fine material as a function of the angularity [219]. In another study of low porosity, particle forces applied over a large number of particles decrease tension on them [54]. The rate of draw also influences the shear stress so that under high rates the shear stress increases [266]. The rate of draw and the travel distance together define the time that fragments are under loads, also known as residence time. The fragments increase their probability of being broken over longer residence times [40] because being under load for longer allows internal cracks to be extended. Miura and Yamanouchi [221] observed that water increases the compressibility and decreases the shear strength under high pressures on sand.

In Brunswick and Kidd Creek mines, backfilling fragmentation was observed flowing through ore passes in which the maximum particle size was reduced by 50% after traveling 300 m vertically [225]. However, the literature review reveals a lack of previous studies on rock fragmentation generated during ore flow. This study aims to expand understanding of fragmentation behavior through a laboratory setup, which models the travel distance of fragments during abrasion, analyzing the rock fragmentation while the material flows through a vertical structure. The fragmentation was quantified and analyzed for different materials and distances.

2 Breakage measurement in granular materials

Breakage in a particle size distribution (PSD) can be difficult to quantify due to the different particle sizes involved. However, several authors have defined parameters to quantify the PSD breakage [88], [212], [213], [262], [280], [281]. Some of these studies only relate the breakage with a characteristic size [88], [212], [213] or the surface area (m^2/m^3 [221], [281]) without representing all the fragmented PSD.

Marsal [280] and Hardin [262] proposed breakage factors using the PSD before and after fragmentation. Marsal [280] defined the particle breakage, Bg, as the percentage by weight of the particles that have undergone breakage, as shown in Eq. 1

$$B_g = \sum_{i=1}^{n} \left(w_{i,b} - w_{i,a} \right) \quad for \quad w_{i,b} > w_{i,a}$$

(1)

where $w_{i,b}$ is the percentage by weight of the ith size interval before fragmentation, and $w_{i,a}$ is the percentage by weight of the ith size interval after fragmentation. On the other hand, Hardin [262] analyzed several PSD of soils before and after different crushing tests and defined the relative breakage, Br, to calculate the breakage in a PSD.

$$B_r = \frac{B_t}{B_p}$$

(2)

In Eq. 2, B_t is the total breakage defined by the area between the initial and final PSD (over 0.074 mm) and B_P is the breakage potential of the aggregate defined by the upper area of the initial PSD (over 0.074 mm). The B_r used all the size intervals (over 0.074mm) independently of whether the mass of the size interval increased or decreased as shown in Figure 1.
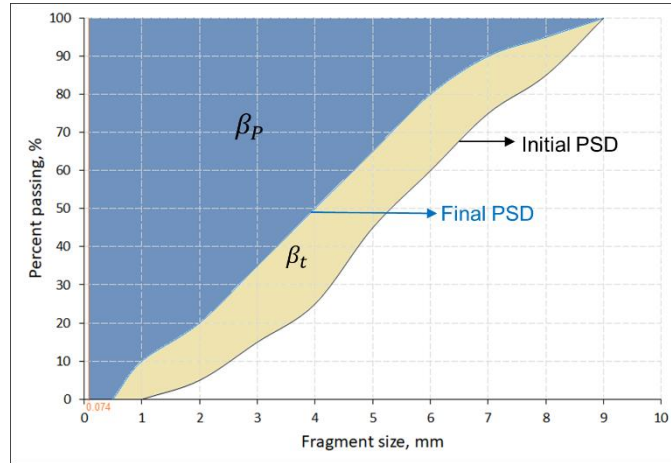
Figure 1. Hardin ¡Error! No se encuentra el origen de la referencia. **breakage parameters. Here parameter β**
$_P$ **contains all the blue area (including β$_t$) whereas β$_t$ is just the area between both PSD.**

3. Methodology

This study analyzes rock fragmentation under different travel distances when rock fragments flow through a vertical section. Three granular materials were tested in four experimental setups and the fragmentation of these materials was characterized and analyzed.

3.1 Laboratory equipment

Three polyvinylchloride (PVC) tubes were used of one, two and three meters in length (Figure 2A). These tubes were placed over a structure to keep them vertical. At the bottom, an extraction system was used to draw the material to keep a constant rate during tests. Figure 2 shows the equipment described and the tube's geometries.

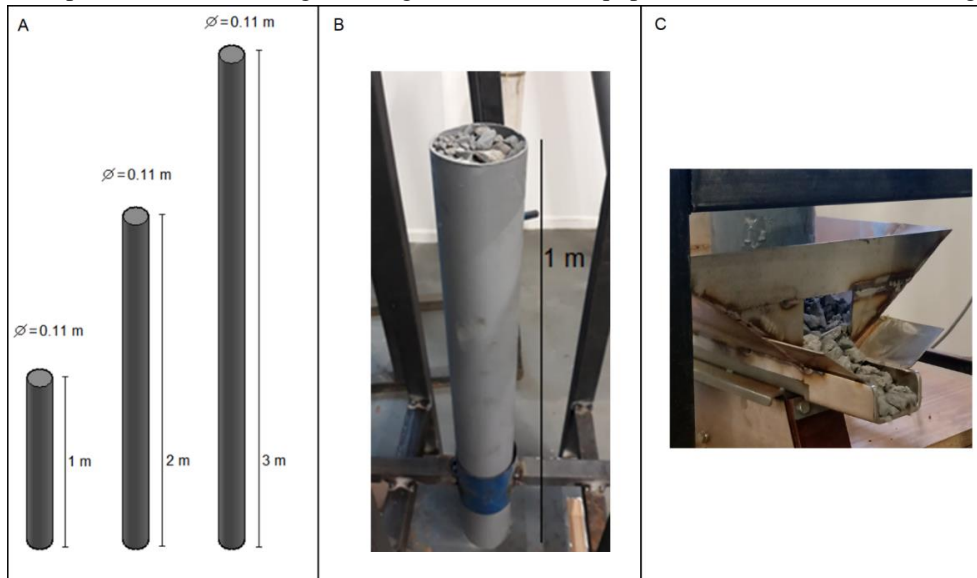**Figure 2. (A) The geometry of tubes used in tests. (B) Example of 1 m tube loaded before test. (C) Extraction system located at the bottom of the tubes.**

Gravel, fragmented concrete, and clay materials were tested using the same tubes. Before the flow tests, material was broken in crushers and then sieved to generate the initial PSD curves. The PSD curves and rock parameters are described in the following section.

3.2 Material characterization

Figure 3 presents the initial PSD of gravel, concrete and clay used in tests. The material was used just once for each test to avoid mechanical changes due to experiments. After flow tests, the final PSD were sieved to measure fragmentation degree. The gravel and concrete materials consisted of the same initial PSD, while the clay material used a smaller PSD.
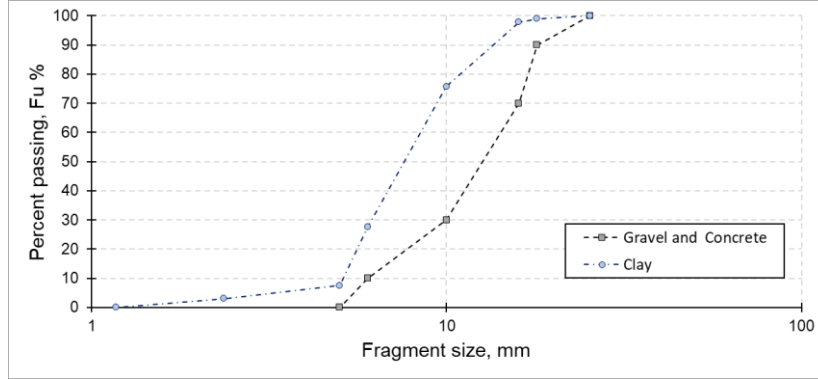

Figure 3. Particle size distribution before flow test.

A fragment size (d_{100}) at least five times smaller than the tube's diameter (D) was chosen to avoid hang-ups in tests; this criterion is based on ore pass studies [83], [241]. Given the width of the tube, d_{100} should be 2.2 cm to ensure gravity flow. In tests, this fragment size was in the larger size interval tested (between 2.54 cm and 1.82 cm). Hang-ups were not observed during flow tests.

Table 1 presents the characteristics of the materials used in these tests. Here, bulk density was determined directly in tubes based on real density. The internal friction angle was obtained using a standard shear test (10 x 10 cm^2 box area) [282]. The strength of the rocks was measured using standard point load test equipment, and the Uniaxial Compression Strength was calculated using the point load index [283]. The wall friction angle, between the material and the PVC tubes, was determined using the Nedderman [142] methodology. This methodology considers the sliding slope of the cohesionless samples. Sphericity and Roundness were determined using the methodology of Cho et al. [273].

Table 1. Summary of material characteristics

Parameter	Gravel	Concrete	Clay
Density [kg/m^3]	2,670±22	2,445±5	2,593±25
Bulk density [kg/m^3]	1,520	1,359	1,158
Internal friction angle [°]	39.0	52.1	44.4
Friction wall [°]	31	27.6	25
Coefficient of uniformity (Cu)	2.48	2.48	1.74
Coefficient of curvature (Cc)	1.12	1.12	0.85
Point load strength index ($Is_{(50)}$) [MPa]	11.24±2.85	2.34±0.27	0.26±0.04
UCS [MPa]	269.7	56.2	6.2
Porosity [%]	43.07	44.39	55.34
Sphericity	0.50	0.60	0.60
Roundness	0.70	0.32	0.21

3.3 Fragmentation tests

Four experiments were defined based on the travel distances of granular material. Materials were tested at heights of 1, 2, 3 and 6 m, for three rock types (gravel, concrete, and clay). For the 6 m experiment, the material flowed two times in the 3 m tube. The material was homogenized before filling. During tests, material was

drawn at a constant rate (20 cm/min) in all tests. All the material was extracted and then sieved to determine the PSD after tests. Each test was run twice to ensure its reproducibility.

4. Experimental results

Output PSD curves were determined with the mean of replicas for each test. The results of 3 and 6 meters of travel distance are presented in Figure 4. It was noted that the formation of small fragments increased when the travel distance of flow increased despite the low overload at laboratory scale. Also, more fragmentation was observed in clay, as was expected because of its lower strength.
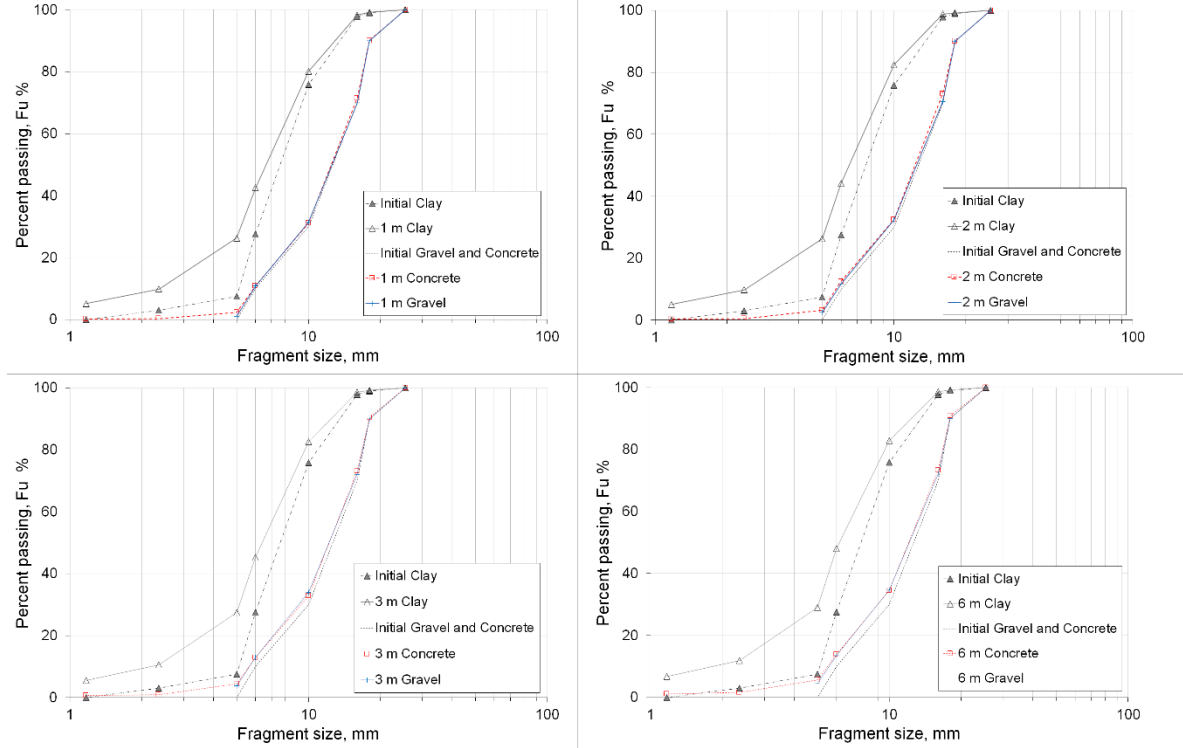
Figure 4. Particle size distribution before and after tests

In concrete and gravel, minimal fragmentation was observed in smaller sizes, while no fragmentation was observed in large sizes ($+P_{80}$). Clay material showed higher breakage, in both mean and large sizes (P_{50} and P_{80}). For d_{80}, the fragmentation was low, except for clay. The PSD shapes varied due to the appearance of smaller sizes, also noticed through the coefficient of uniformity, Cu (d_{60}/d_{10}), as indicated in Table 2.

Table 2. Coefficient of uniformity, d_{10}, d_{50} and d_{80} before and after tests.

Parameter	Material	Initial	Test 1 m	Test 2 m	Test 3 m	Test 6 m
	Clay	1.71	3.31	3.22	3.41	3.85
Cu	Concrete	2.45	2.50	2.52	2.54	2.56
	Gravel	2.45	2.45	2.46	2.47	2.49
	Clay	5.2	2.4	2.4	2.2	1.9
d_{10} [mm]	Concrete	6.0	5.9	5.8	5.7	5.6
	Gravel	6.0	6.0	5.9	5.8	5.7
d_{50} [mm]	Clay	8.1	6.8	6.6	6.5	6.2
	Concrete	13.3	13.1	12.8	12.8	12.6

	Gravel	13.3	13.1	13.0	12.7	12.6
	Clay	10.3	10.0	9.8	9.7	9.7
d_{80} [mm]	Concrete	17.0	16.9	16.8	16.8	16.8
	Gravel	17.0	17.0	17.0	16.9	16.9

5. Travel distance analysis of particle breakage

In the experimental setup, the granular material flowed as a plug flow, where few shear stresses were expected. However, fragmentation was observed due to travel distance as shown in Figure 5 through the relative breakage [262]. The relative breakage represents the fragmentation of the PSD and demonstrates that the travel distance influenced the degree of fragmentation in the materials tested.
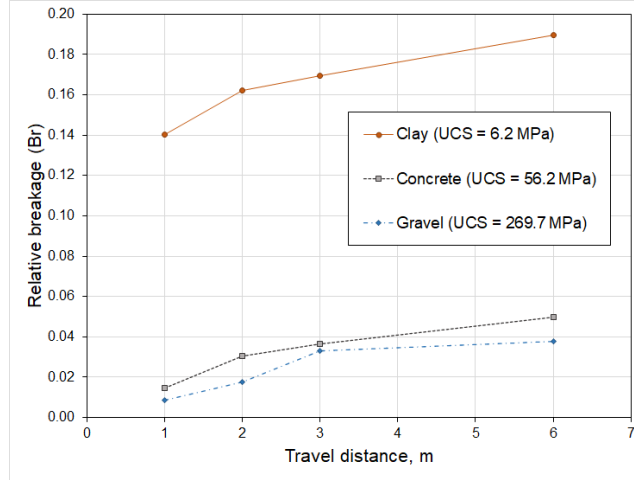

Figure 5. After-test PSD fragmentation at different travel distances

The particles were rounded during flow and their singularities were reduced. With fewer singularities, fragments cannot be broken under low stress conditions. This phenomenon is relating to the roundness effect of particles due to abrasion. Abrasion was the main fragmentation mechanism observed, with an important difference between the fragment strength and the stresses. Nevertheless, the fragmentation degree is directly related to the rock strength (UCS). The mean initial stress in granular material can be estimated through the formula proposed by Janssen [39] as presented in Eq. 3

$$\overline{\sigma_v} = \frac{R_h \rho_b g}{\tan(\phi_w)(1 - \sin(\phi))}\left(1 - e^{-\frac{\tan(\phi_w)(1-\sin(\phi))z}{R_h}}\right) \tag{3}$$

where $\overline{\sigma_v}$ is the mean vertical stress, R_h is the hydraulic radius (area/perimeter; 0.0275 m), ρ_b is the bulk density (kg/m³), g is the gravity constant (m/s²), ϕ is the interparticle friction angle, ϕ_w is the wall friction angle, and z is the depth (depending on the experimental setup 1, 2 or 3 m). The terms, $1 - \sin(\phi)$, represent the horizontal and vertical stress ratio, σ_h/σ_v, and these terms have shown good estimation with other experimental results[33], [70]. The differences between the initial vertical stress (in static condition) and the UCS of the three materials are presented in Figure 6.
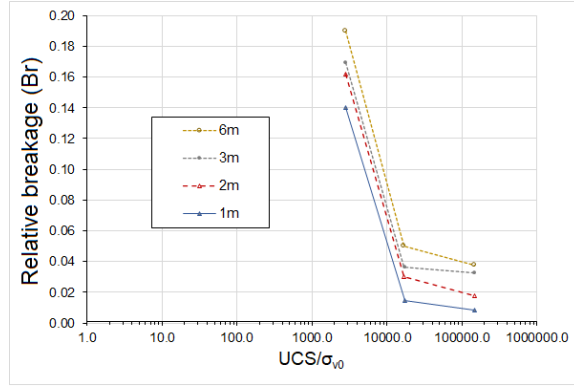
Figure 6. Relative breakage versus the strength stress ratio as measured in the experimental setup.

The Br is a function of the travel distance and the ratio between the strength (UCS) and the initial vertical stress (σ_{v0}). The stress decreases during draw, but large variations should not be expected due to Eq 3. In clay material (the smallest ratio), the Br highly increased compared with the concrete and gravel tested. Small differences in the Br are observed when the ratio of the concrete (UCS/σ_{v0} > 16,900) is exceeded.

The fine material generated can be observed through the d_{10} before and after tests. Figure 7 shows the ratio between the initial and the final d_{10} demonstrating no evident differences between the concrete and gravel materials. To obtain further information about longer travel distances, a test using concrete was repeated six times (18 m) and the material trend was maintained, where the fragmentation increased slightly with distance.
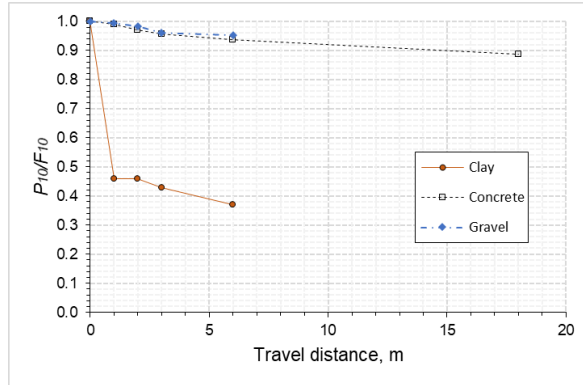

Figure 7. d_{10} ratio before (F_{10}) and after (P_{10}) tests as function of the travel distance.

Results showed that the final d_{10} decreases when fragment travel distance increases. In lower size fragments, breakage and minor angularities could be observed. It was also observed that the large sizes break singularities of smaller sizes. Then, it is assumed that two mechanisms are required to break large fragments: a high load point and/or fewer contact points among the fragments. However, large fragments have a high probability of being in contact with other particles. This result is similar to the test of a bimodal distribution developed by Bridgwater et al. [108], where under low shear stress, 90% of large particles kept their initial size. After testing, major sphericity and roundness in clay were observed, along with a greater presence of fine material for clay and gravel, despite the low loads within the physical model. Then, the main fragmentation mechanics observed in tests corresponded to abrasion that increased with the travel distance.

6. Fragmentation in Block Caving
In block caving, there are high broken columns where rock fragments can travel large distances. In these broken columns, fine material can be expected due to abrasion that could imply problems such as mudrush, in-rush of fine events, or cohesive hang-ups [61], [78], [111], [133]. On the other hand, a wider PSD is developed when

the fine material is increased. If there is a source of fine material (like waste rock of low strength) a wide PSD would delay the fine material migration of this source [16], [113], [284]¡**Error! No se encuentra el origen de la referencia.**.

In block caving mines with high economic columns, such as the North Parkes mine, the Grasberg Deep Ore Zone and the Deep Mill Level Zone mines, the Palabora mine, and the Cadia East mine [285], [286], when attempting to estimate the fragmentation, it is recommended to consider additional fine material generation during secondary fragmentation. In this section we present a mine example of how this additional fine material generation during draw can be incorporated applying a secondary fragmentation model introduced in [31]. This fragmentation model estimated the mass fraction in a size interval i, m_i, using Eq. 4.

$$m_i = \sum_{j=1}^{i} A_{ij} e^{-S_j \tau} \qquad (4)$$

A_{ij} is expressed as follow in Eq. (5), S_j is the selection function at which material undergoes breakage to the jth size interval, and τ is the residence time and denotes the time that material is under the breakage process.

$$A_{ij} = \begin{cases} 0 & if\ i < j \\ f_{ij} - \sum_{k=1}^{i-1} A_{ik} & if\ i = j \\ \sum_{k=j}^{i-1} \frac{b_{ij} S_k}{S_i - S_j} A_{kj} & if\ i > j \end{cases} \qquad (5)$$

In Eq. 5, f_{i0} is the initial particle size distribution. Therefore, Eq. 4 allows the size distribution of a fragmentation process to be predicted after b_{ij} (breakage function, Eq. 6) and S_j (selection function, Eq. 7) are determined.

$$B_{i1} = \alpha_1 \left(\frac{x_i}{x_2}\right)^{\alpha_2} + (1 - \alpha_1) \left(\frac{x_i}{x_2}\right)^{\alpha_3} \qquad (6)$$

In Eq. 6, α_1, α_2 and α_3 are model parameters ($0 < \alpha_1 < 1$; $\alpha_2 < \alpha_3$) and x_i is the mesh size for the ith interval and x_2, which corresponds to the second mesh size interval.

$$S_j = S_1 exp\left\{Z_1 ln\left(\frac{d_i}{d_1}\right) + Z_2 \left[ln\left(\frac{d_i}{d_1}\right)\right]^2\right\} \sigma_v \qquad (7)$$

Z_1 and Z_2 are parameters that depend on the properties of the materials used, and σ_v is a variable that represents the mean vertical load. The residence time (Eq. 4), τ, indirectly applies the travel distance through the height of draw. This effect was reported at mine scale in [287] in which the fragmentation increased when the height of draw was increased because a higher residence time was applied. Nevertheless, additional fine material generation was not estimated in relation to travel distance. However, a correction factor can be incorporated in the selection function to improve the adjustment of the rate of breakage [272]. Additionally, the breakage distribution defined by the breakage function can be calibrated at mine scale to generate more fine fragments during breakage events; an example is presented in Figure 8.
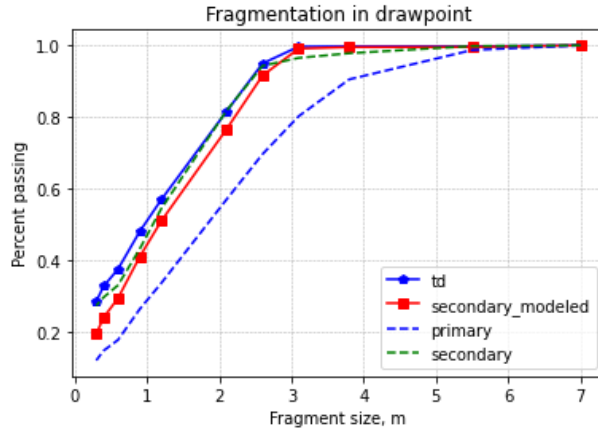
Figure 8. Travel distance effect at mine scale modelled with a secondary fragmentation model [31]. **Here, primary and secondary fragmentation are considered to be the PSD of a mine. The td curve represents secondary fragmentation estimated including the travel distance effect.**

7. Conclusions

This study quantified the rock fragmentation based on different travel distances of rock fragments. Abrasion related to travel distance was identified as one of the main mechanisms present during our experiments. Fragmentation was mainly observed in smaller fragment sizes despite the material strength and the low overload. This is also observed because the amount of fine material is increased in comparison with large size breakage. Abrasion was not found to generally affect larger sized particles because their singularities require abrasion from other larger particles and/or fewer particle-to-particle contact points to be broken. From our studies it could also be assumed that in the presence of ore passes and a high broken column in block caving, a significant amount of fine material generation would be expected that could imply operational problems, particularly in low strength materials.

Paper 3: Experimental quantification of vertical stresses during gravity flow in block caving

Raúl Castro, René Gómez, Matthew Pierce, Juan Canales

Abstract

Usually in block and panel caving mines, when the caving connects to the surface, monitoring of vertical stresses over production drifts is minimal due to the low probability of seismic events. However, when the stresses over the production level are related to an overburden by fragmented rock, the draw policies highly influence induced stress. In this context, we present an experimental set up using a laboratory-scale model to identify the role of draw strategy on induced vertical stresses in a block-caving layout. Here, three draw strategies are studied: isolated draw, panel caving draw, and block caving draw. Results show that induced vertical stresses can vary between 0.3 and 2.8 times their initial vertical value and are highly influenced by both the distance from the extraction front and the dimension of draw and non-draw areas. These findings provide useful information to support the system design in block caving or panel caving methods to decrease induced vertical stresses related to draw and define rules of extraction in an effort to avoid problems related to the maximum stress that can be expected on production-level pillars.

Key words: Caving mining, granular material, gravity flow; induced stresses, stress, rock.

Introduction

Current challenges in the mining environment include factors such as deeper deposits, harder rock, higher in-situ stresses, greater production demand and increased costs [153], [154]. One issue which can have consequences at greater depths is that the rock mass already subjected to high stresses suffers even higher induced stresses during mining activities. In particular, induced stress occurs during the caving propagation stage in the advancing undercut front [40], [155], [156], where damage has been observed and reported in several block caving mines [157]–[162], mainly related to drift convergence and pillar failure. Measurements of stresses, strain, crack extension and seismicity have been carried out at this stage [163]–[165], [288]. However, in caving mines with greater depths, the column height of caved rock also increases, and consequently, there is an overload on the production level.

Usually in block or panel caving mines, when the caving propagation connects to surface, vertical stress over the production drifts is not closely monitored because of the low frequency and magnitude of seismic events. Nevertheless, experience indicates that production drift stability can also be affected during ore extraction in productive areas [57]–[59], [166], [168] causing drift convergence, concrete slabbing at the walls, collapse and closure.

In granular material, such as caved rock ore, vertical stresses are significantly lower than total column weight because of the arching effect generated by shear stresses due to the rock friction. Janssen [39] initially postulated Eq. (1) that provides the mean vertical stress, $\overline{\sigma_{v,0}}$ (Pa) in certain depth, z (m), considering overload, Q_0, [143].

$$\overline{\sigma_{v,0}} = \frac{R_h \rho_b g}{\mu k}\left(1 - e^{-\frac{\mu k z}{R_h}}\right) + Q_0\left(e^{-\frac{\mu k z}{R_h}}\right) \tag{1}$$

Where R_h is the hydraulic radius (area/perimeter; m) introduced by [42], ρ_b is the bulk density (kg/m³), g is the gravity constant (m/s²), k is the friction parameter that represents the horizontal and vertical stress ratio, σ_h/σ_v, z is the depth of caved rock (m), Q_0 is the initial vertical overload (Pa) and μ is the friction between particles and model wall expressed usually by $\tan(\phi_w)$, where ϕ_w is the friction angle of bin walls (degrees). This equation gives a reasonable result in static conditions. However, one of the common problems is

determining the k parameter because of the high variability of stress in granular material. Different approaches have been used to define k such as [289],

$$k = 1 - sen(\phi) \tag{2}$$

Where ϕ is the material internal friction angle, the relation $\phi > \phi_w$ has been reported [42], [145], [289]. Other approaches to define k are presented in Eq. (3) and (4),

$$k = \frac{1 - sen(\phi)}{1 + sen(\phi)} \tag{3}$$

Eq. (3) is defined as an Active case, when $\sigma_h < \sigma_v$ and Eq. (4) is defined as a Passive case, when $\sigma_h > \sigma_v$ [290].

$$k = \frac{1 + sen(\phi)}{1 - sen(\phi)} \tag{4}$$

Walker [143] introduces in Eq. (5) a general relation for k using the Mohr-Coulomb circle considering that horizontal and vertical stresses are not necessarily the principal stresses.

$$k = \frac{1 - sen^2(\phi)}{1 + sen^2(\phi)} \tag{5}$$

The equations above were developed in physical models to quantify the magnitudes and distribution of stresses in static and dynamic conditions [39], [42], [62], [141], [143], [145], [289]–[293]. Eq. 2, 3 and 5 have shown good correlation under static conditions. In dynamic conditions, different results have been reported for k and μ parameters in physical and numerical models [289], [294]–[296], mainly as a function of the granular material's height. However, granular materials used in these studies (e.g. bean, corn, sand, wheat, barley and coke) are different from material found in the mining environment, where wide particle size distributions, high strength, major internal friction angles and angular fragment shapes are common. Few physical models emulating mining conditions have been developed [33], [117], [238].

When granular material is under flow, at least two main zones − the movement zone and the stagnant zone – can be identified. In the movement zone (or draw zone), porosity increases and vertical stresses decrease due to flow, while in the stagnant zone (or non-draw zone) vertical stresses increase. Experimental measures have shown that stresses can be transferred from the movement zone to the stagnant zone during flow [33]. Then, induced vertical stresses over the production drift depend on the movement of gravity flow zones. In the same way, Lorig [69] postulated that stresses in the isolated movement zone (IMZ) tend to be lower than in surrounding stagnant material. This may occur because stresses are transferred through shear forces acting on boundaries between flow and stagnant material. Furthermore, it was concluded in [54] that the mean magnitude of forces acting inside the IMZ is independent of the column height and weight.

Pierce [54] proposed applying the tributary area theory to determine the mean vertical stresses in the stagnant zone, $\overline{\sigma}_v^S$, as:

$$\overline{\sigma}_v^S = \frac{\overline{\sigma}_{v,0}A - \sum_{i=1}^n \overline{\sigma}_{v,i}^M A_i}{A_s} \tag{6}$$

Where $\overline{\sigma}_{v,0}$ is the mean vertical stress before draw (initial condition, Pa), A is total area (m²), $\overline{\sigma}_{v,i}^M$ is the mean vertical stress of the movement zone i calculated using Eq. 1 and Eq. 3 (Pa), A_i is the area of the movement zone i (m²) and As is the area of the stagnant zone (m²). Areas are where the caved material is placed in a plan view.

In caving mines, the draw is different in each case. For example, block caving extracts material in a different way than panel caving. Information on the influence of different kinds of draw on induced vertical overloads on the production level is, thus, generally lacking. Then, the objective of this investigation is to use laboratory-scale experiments to quantify the role of draw strategy on induced vertical stresses over pillars located in the production levels to define draw policies that minimize induced stress in critical areas. In particular, nowadays a number of active or planned block and panel caving operations are subjected to greater depths such as El Teniente and Chuquicamata's Underground Project in Chile, the Deep Ore Zone and Deep Mill Level Zone in Indonesia, Resolution Copper and the Henderson mine in the United States and Cadia East in Australia.

2 Experimental methodology

Here a physical model for studying the vertical stress behaviour under flow conditions was constructed representing different draw strategies used in block and panel caving.

2.1 Similitude analysis

The focus of this work is to quantify stresses on granular material for block caving applications using laboratory-scale experiments. For this reason, the geometric similitude is kept constant both in the physical model and the granular material with a length scale factor, λ_l, of 1:200. Furthermore, following conditions of similitude, cohesionless material is used to study stresses on granular material [33] to avoid adhesive forces such as Van der Wall's forces, liquid bridges and electrostatic effect at laboratory scale. Then the material used must be dry and include fragment sizes larger than 0.06 mm [297]. On the other hand, the gravity, bulk density and residual friction angle scale factors are the same in the model as at mine scale, respectively $\lambda_g = \lambda_\rho = \lambda_\phi = 1$. Then, the scale of stresses is equal to the length scale factor, $\lambda_\sigma = \lambda_l$. This geometrical scale considered (length scale, $\lambda_l = 1/200$) ensures representation of the induced stress phenomena. According to the scaling laws [33], the similitude's parameters are shown in Table 1. Here physical variables are based on the length scale used.

Table 1 Scale factors based on length scale

Variable	Factor	Scale factor	Value
Length	λ_L	λ_L	0.005
Area	λ_A	λ_L^2	0.000025
Volume	λ_V	λ_L^3	0.000000125
Time	λ_T	$\lambda_L^{0.5}$	0.0707
Weight	λ_W	λ_L^3	0.000000125
Stress	λ_S	λ_L	0.005
Friction angle	λ_ϕ	1	1
Density	λ_ρ	1	1

The following assumptions and simplifications were made to study the stress behaviour in block caving through physical modelling: (1) It is assumed that the rock mass has caved to surface, forces in the system are due to the material's weight, and in-situ stresses are not present. (2) The granular flow occurs in a 3D environment. (3) The rock breakage mechanism related to secondary fragmentation is not considered. (4) The geometries of the flow zones in the physical model are comparable as long as the materials have equal friction angles and particle shapes. The influence of friction in the model's container walls is discussed in section 2.2.

2.2 Physical model

The physical model represents a section of a mine operated by Block or Panel caving with the following dimensions: 140 m length, 46 m width and 480 m column height (see Figure 1). The scale was chosen to represent a high column height where vertical stress at the bottom would be significant. In the production level, we selected El Teniente's 30 m x 15 m layout.
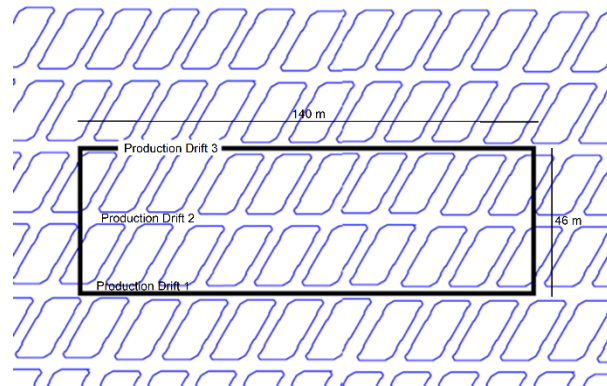
Figure 1. Mine area represented in the physical model.

The mine section corresponds to three production drifts and nine extraction drifts, which represent a total of 36 drawpoints (Figure 2 and Figure 3-a). Figure 2 shows the dimensions of the production level in the physical model. Fine material was glued on the crown pillar over the production drifts to represent the rock friction over pillars and the flow zones' geometries, simulating 3D drawbells.
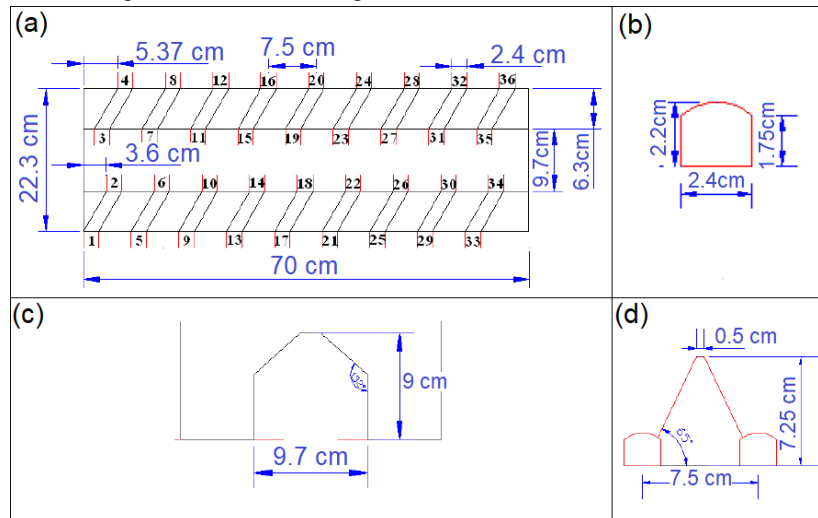

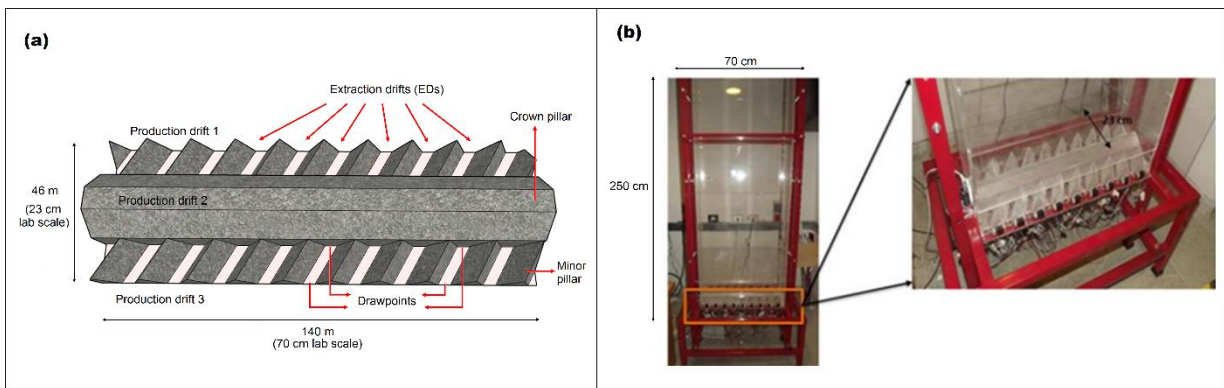**Figure 2. Geometry of production level represented at the physical model scale.**

Figure 3. (a) Sector studied in experiments and main structures, plan view (b) Physical model of plexiglass used in laboratory.

The walls of the physical model as shown in Figure 3-b were made of plexiglass. The plexiglass allows movement zones to be observed in the model. This material also increased vertical stress compared with horizontal stress because of the low friction between plexiglass and granular material. For minor frictions, shear forces decrease between the model wall and granular material, then more weight is transferred to the bottom (increasing vertical stress estimated there). For example, we can calculate a vertical stress of 1.35 MPa applying Eq. 1, considering a depth of 500 m, an internal friction angle of 39º, a hydraulic radius of 16.9 m, a bulk density of 1.4 t/m^3 and a wall friction angle of 25º. If we considered a higher friction angle, like the internal friction angle of 39º, a hydraulic radius 74% higher gives us the same vertical stress. For this reason, in this study vertical stress results, σ_v, will be analysed as a function of their initial value, $\sigma_{v,0}$, using the ratio $\sigma_v/\sigma_{v,0}$.

Up to six load cells were located within the model over the crown pillar for vertical stress measurements. Each load cell has a precision of $\pm$ 0.039 kPa (8 g), a length of 11.5 cm and an area of 20 cm^2. The position of load cells over the crown pillar depends on the purpose of the experiment. Thus, load cell location is shown with the results for each test in Section 3 (Figures 6, 9, 12 and 15).

2.3 Model media

Tests used crushed sulphide ore with a high aspect ratio (sphericity 0.58 and roundness 0.25, Cho et al. [273] methodology), which is representative of caved rock. The particle size distribution was obtained by scaling (1:200) the primary fragmentation curve expected for Chuquicamata Underground Block caving project (see Figure 4). The ore characteristics are shown in Table 2.
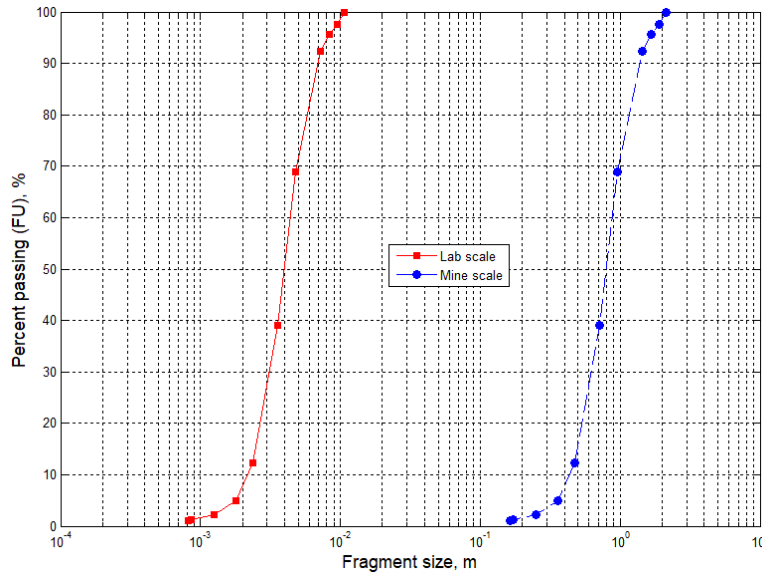
Figure 4. Fragment size distribution curve used in experiments scaled from a real Block-caving size distribution curve.

Table 2 Ore characterization

Parameter	Value	Unit
Mean size, d_{50}	4.0	mm
Coefficient of uniformity, Cu	2.0	
Point load index, IS_{50}	6.2 ±1.6	MPa
Density	2.6	t/m3
Bulk density	1.42	t/m3
Porosity	44	%
Friction angle	39	°
Repose angle	29	°

Sulphide ore corresponds to a biotite and amphibole granitoid, showing metallic mineralization of pyrite, chalcopyrite and bornite. Potasic and propilitic alteration can be seen in the rock samples and mafic minerals, respectively.

2.4 Experimental set-up and procedure

The main objective of this work is to study the stresses induced by ore draw, considering common draw practices applied in Block and Panel caving mines. Undercutting development, in Block and Panel caving, is the principal difference between them. Block-caving undercutting is performed in just one stage, or block, at a time (Figure 5-a), whereas panel-caving undercutting is performed over time by opening drawbells monthly (Figure 5-b). These differences usually imply that at the beginning of block caving extraction, all drawpoints of one block could be available. However, for different operational reasons, unmoved zones without extraction or overdrawn zones may also exist. On the other hand, in panel caving, it is common to find open drawpoints, closed drawpoints, and drawpoints with differences in their extraction percentage.
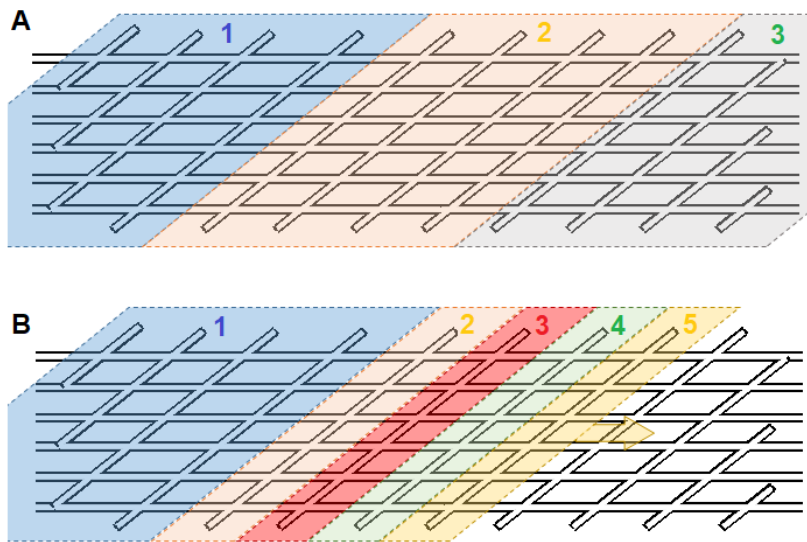

Figure 5. Plan views (a) Block caving strategy: in blocks 1, 2 and 3 the extraction begins at different periods. Each block should be drawn uniformly. (b) Panel caving strategy: in panels 1, 2, 3, 4 and 5 the extraction begins consecutively. Panels have different extraction percentages; greater percentages are in the first panels.

Table 3 lists the four experimental set ups with their objectives, as well as the draw strategy and the procedure chosen. To observe and quantify result variability, two tests (A and B) were carried out with each experimental set up (Tests 0, 1, 2 and 3) for a total of 8 experiments. We defined different draw strategies in each test then grouped results according to the draw strategy used for analysing them: isolated draw (base case), panel caving and block caving draw strategies, respectively.

Table 3: Experimental set-up of gravity flow draw strategies

Test	Name	Objective	Procedure
0	Isolated draw	To measure IMZ and vertical pressures over the crown pillar for a single drawpoint.	Extraction was carried out from one drawpoint (from Extraction Drift (ED5)) next to the crown pillar. Twenty kilograms of ore drawn at 2.5 kg/h.
1	Panel caving	To measure vertical pressures over the crown pillar considering a panel caving draw scenario.	Extraction was done from ED1 up to ED7. In total, one kg were drawn per drawpoint. During test EDs 1 and 2 were closed and EDs 6 and 7 opened. Test draw rate ~5 kg/h.

| 2 | Block caving – 60 m of unmoved zone | To measure vertical pressures over the crown pillar with an intermediate non-draw area, following a block-caving draw scenario. | ED 1 to 3 and ED 7 to 9 were drawn at the same rate until flow zones reached the surface. Afterwards, extraction was done in ED 4 to 6. Test draw rate ~6.5 kg/h. |
| 3 | Block caving – 30 m of unmoved zone | To measure vertical pressures over the crown pillar with a smaller intermediate non-draw area. | Extraction was conducted in all EDs except ED5. At the end of the experiment, extraction was conducted in ED5. Test draw rate ~6.5 kg/h. |

For each test, the load cells were located based on the point of interest defined by the draw strategy. The material described in the Model Media section, previously homogenised, was then loaded in the physical model to the top (2.5 m). The draw strategy defined for the test was then programed through a servo-assisted motor. In block caving draw strategies, all drawpoints were drawn at the same time until near the end of the tests when active drawpoints were stopped and drawpoints located under the unmoved zone were drawn. For the panel caving draw strategy, the extraction was carried out through a group of extraction drifts continuously until 1 kg per drawpoint was extracted; the drawpoints were then incorporated and/or closed depending on the period of extraction following a panel caving scenario. In this work, the effect of rate of draw was not studied because the stresses measured in the load cells changed almost instantly in all extraction policies observed regardless of extraction velocity.

2.5 Initial stress conditions

Initial vertical stresses were measured in all tests as the following: 14.8 ± 3.2 kPa in Test 0, 17.8 ± 1.8 kPa in Test 1, 27.7 ± 3.7 kPa in Test 2, 18.3 ± 3.7 kPa in Test 3 and the initial vertical stresses based on Eq. (1) is 18.7 kPa. Here the mean vertical stress is based on the material characteristics defined in Table 2 and assuming $k = 0.37$. The initial vertical stress ranges are expected for physical measurement of granular material due to arching, as reported by other studies [33], [117], [238], [292].

3 Draw test results

In this section vertical stress measurements are presented during draw condition. In the first test run, the extraction from one drawpoint defines the IMZ geometry of granular material used. Then, panel and block caving draw strategies are tested showing the influence of the extraction strategy on induced stress.

3.1 Test 0: Isolated draw

In this test, ore draws from just one drawpoint located in the middle of the model (see Figure 6). Figure 6-b indicates the load cells' location over the crown pillar. The evolution of the IMZ geometry is according to the kinematic theory normalized by d_{50} $w = 3.42\sqrt{h}$ [64], where w is the IMZ width and h is the IMZ height presented against results in Figure 7.
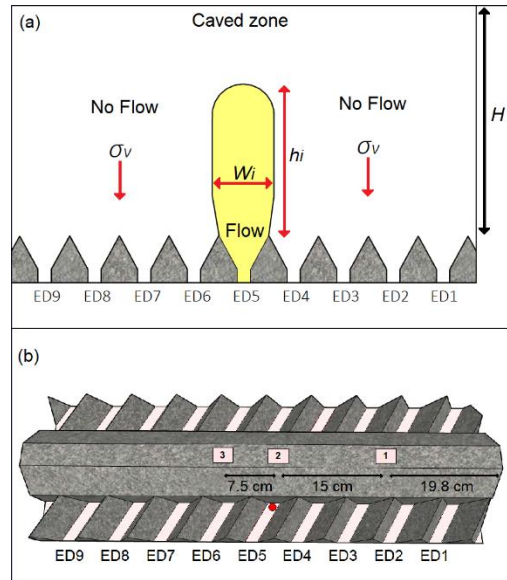
Figure 6. (a) Isolated draw strategy configuration (front view) and (b) Load cell location over crown pillar.
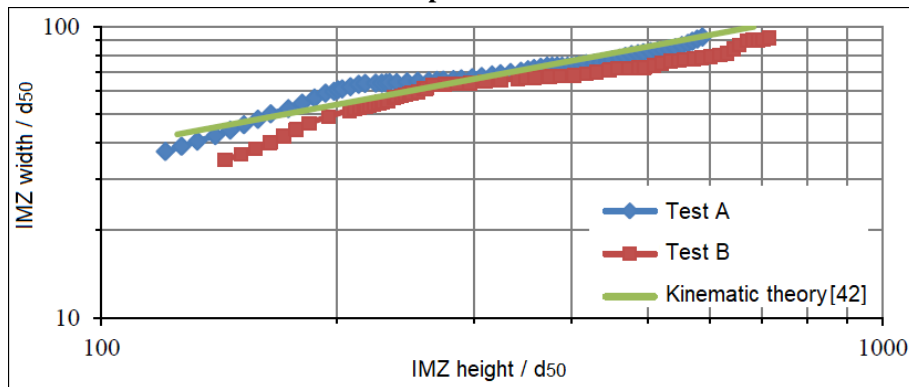
Figure 7. Isolated movement zone geometry evolution.

During this test, the IMZ radius reached 7.8 cm when 0.7 kg of material were extracted (Figure 8, right vertical axis). Here, load cells 2 and 3 were below the shadow of the flow zone. Then, the IMZ radius reached 16 cm when 14.6 kg of material were extracted, over load cell 1 (located at 15.8 cm from the active drawpoint).

65
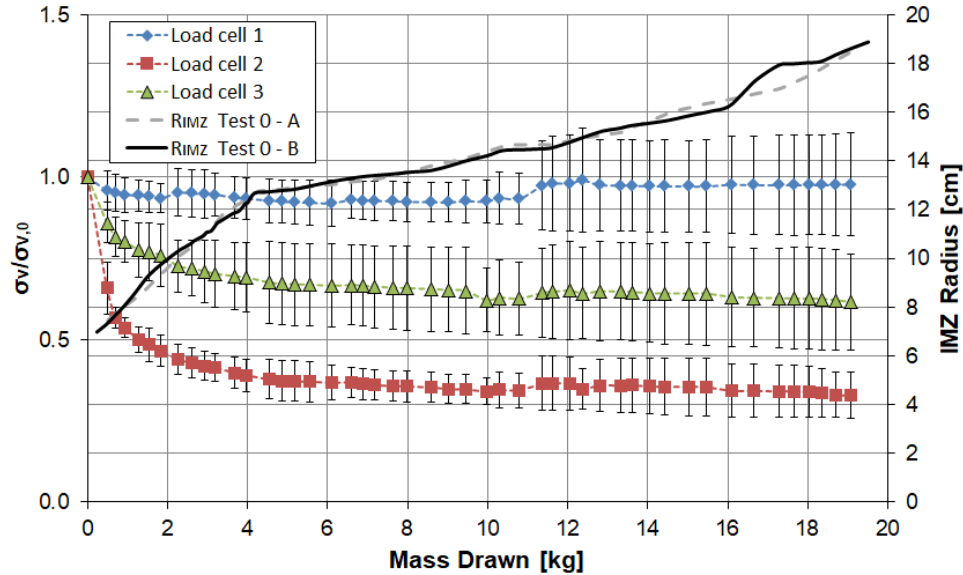
Figure 8. Induced vertical stress by mass drawn and IMZ radius evolution under mass drawn. Isolated draw. Here, σ_v: vertical stress, $\sigma_{v,0}$: initial vertical stress, R_{IMZ}: IMZ radius (for tests A and B). The error bar shows the vertical stress variability (between tests A and B).

We observed that vertical stress decreased in load cells closer to the drawpoint under extraction (load cells 2 and 3). Load cell 2 decreased 0.4 times its initial value, whereas load cell 3 decreased its initial value 0.6 times. Load cell 2 is closer than load cell 3 to the drawpoint under extraction; then a distribution of vertical stress into the IMZ can be assumed increasing from the IMZ's centre. It is known that greater (higher) porosity in granular material flow is generated next to the extraction point. In draw zones, the bulk density is decreased due to greater porosity. Greater porosity also implies fewer contact points to transfer stresses in the granular material, which increases the stress transfer on more compacted material, which in this case is the material found in the non-draw zones.

On the other hand, load cell 1 showed no major variation from its initial load condition. It can be seen that inside the IMZ, vertical stress was lower than initial stress, as expected, and decreased closer to the drawpoint. In the non-draw zone, overstress (on load cell 1) was not observed. Possible reasons for this are its proximity to the flow zone, the ratio between the draw and non-draw zones, and/or a shadow effect cast by the IMZ. Further experiments could be done to identify the cause or causes of this effect.

3.2 Test 1: Panel caving draw strategy
In test 1, various drawpoints were opened based on the panel caving strategy defined in section 2.4. Extraction drifts were drawn one by one from right to left (Figure 9-a), in accordance with a common production plan. Experiments here show a mass flow zone (interactive draw between drawpoints under extraction). The extraction drifts (ED) were added from ED1 to ED7, between 27.1 and 47.7 kg ore was drawn from ED1 to ED5, between 47.7 and 67.5 kg ore was drawn from ED3 to ED6, and between 67.5 and 78.2 kg ore was drawn from ED3 to ED7.
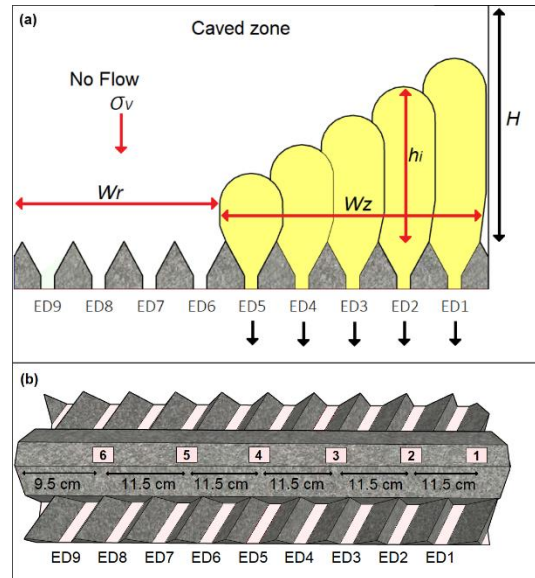
Figure 9. (a) Panel caving draw strategy configuration (front view) and (b) Load cell location over crown pillar.

Figure 9-b shows the locations of the six load cells. This distribution allows vertical stress measurements in draw and non-draw zones during extraction. Here, the addition of extraction drifts caused the formation of an unmoved zone in front of the extraction front. Figure 10 shows the test's evolution, in which the width of the non-draw zone (defined by Wr) continuously decreases while new EDs begin extraction. Induced vertical stress in a non-draw zone will necessarily increase if its area is decreased, as observed in Figure 11.
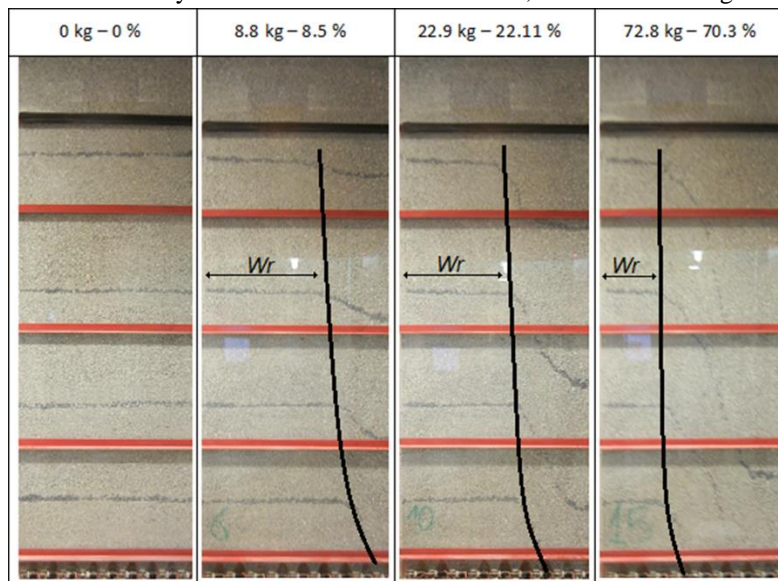
Figure 10. Test 1 draw evolution during Panel caving draw strategy.

Figure 11 illustrates results for all load cells. The stress measurements show overloads in the non-draw zone (also known as stagnant zone) and under-loads in the draw zone (movement zone). Stresses recorded by cell 1 (Figure 11-a) decreased rapidly when extraction started because this cell was below the flow zone, 0.30 $\sigma_{v,0}$. When 40 to 50 kg of ore was extracted, drawpoints of ED 1 and 2 were closed, this increased the induced vertical stress to 1.36 $\sigma_{v,0}$. Load cell 2 showed similar behaviour with stress variations between 0.26 $\sigma_{v,0}$ below the flow, increasing to 0.54 $\sigma_{v,0}$ when EDs were closed. Load cell 3 was located in the stagnant zone at the beginning of extraction. The vertical stresses showed no change in value until drawpoints near (ED4) were

extracted; at which point, induced vertical stress decreased to 0.26 $\sigma_{v,0}$ (Figure 11-a). Vertical stresses on load cells 4, 5 and 6, located initially in the stagnant zone away from drawpoints under extraction, continuously increased due to the extraction (Figure 11-b). In these cells, vertical stresses increased even though the mass in the model was continuously decreasing. Then, vertical stress on load cell 4 decreased to 0.36 $\sigma_{v,0}$ when the load cell was below the flow zone at the end of the test. In this test, load cell 6 reached the maximum value observed of 1.77 $\sigma_{v,0}$.
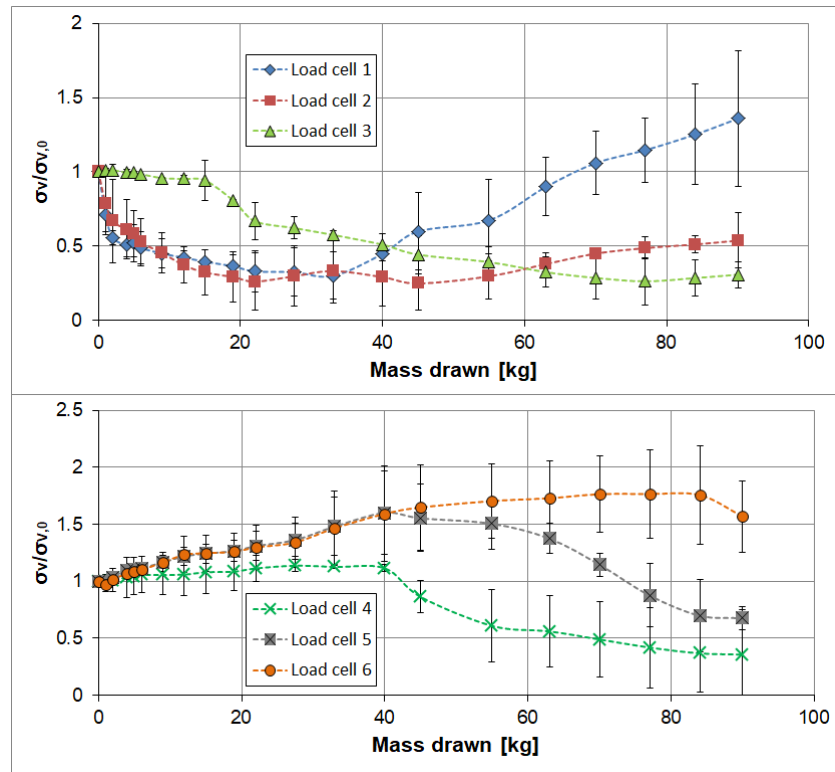
Figure 11. Induced vertical stresses by mass drawn (a) Results from Load cells 1, 2 and 3 and (b) Results from load cells 4, 5 and 6. Here, σ_v: vertical stress, $\sigma_{v,0}$: initial vertical stress.

In the non-draw zone, a direct relation was observed in load cells 4, 5 and 6, between the vertical stress and the stagnant zone width (*Wr*), such that when the stagnant zone decreased, the vertical stress increased.

3.3 Test 2 and 3: Block caving draw strategies
In tests 2 and 3, ore was extracted from the drawpoints in the outer areas at the same time. For those drawpoints located in the middle of the model, ore was not extracted until the end of the tests.

3.3.1 Test 2: Non-ideal draw with 60 m of unmoved zone
The outer area extraction drifts (EDs) were drawn together while three EDs were not drawn in the middle (see Figure 12). The flow zone evolution indicates that initially the flow zones interact among EDs 1 and 3 and, separately, among EDs 7 to 9, leaving an unmoved zone, which has a width (*Wr*) observed in Figure 13.

Figure 12. (a) Block caving draw strategy configuration with high non-draw zone (front view) and (b) Load cell location over crown pillar

When extraction progressed, the flow zones of each group of extraction drifts interacted in height, leaving just a small portion of unmoved volume at the ore bottom. After approximately 95 kg extracted, draw strategy changed as EDs under draw (ED 1, 2, 3 and 7, 8, 9) were stopped and drawing was started from ED 4, 5 and 6.

Figure 13. Test 2 draw evolution in Block caving draw strategy (60 m)

Vertical stress measurements are shown in Figure 14. The load behaviour observed was as follows:
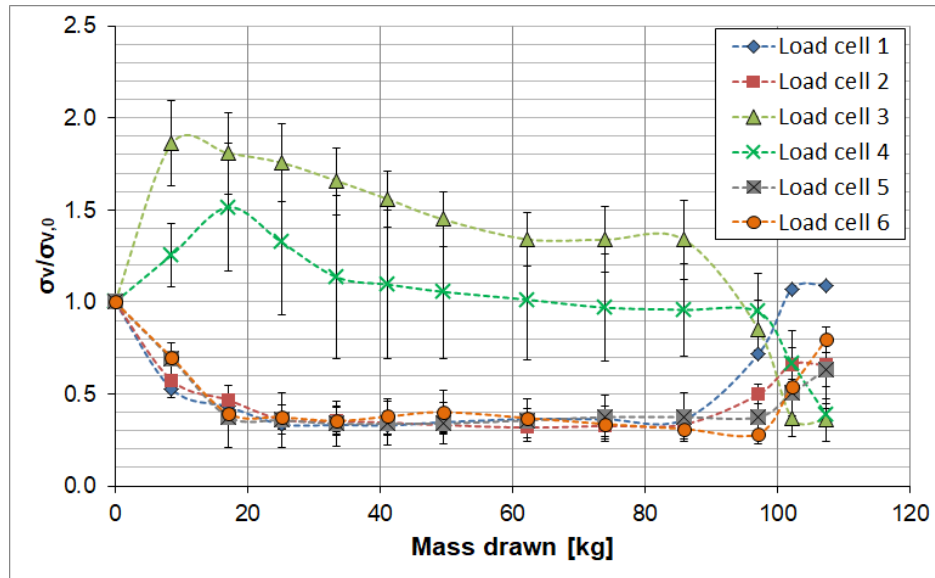
Figure 14. Induced vertical stresses by mass drawn load cells 1 to 6. Here, σ_v: vertical stress, $\sigma_{v,0}$: initial vertical stress.

Load cells 1, 2, 5 and 6 were placed within flow zones. When extraction began, vertical stresses in these cells decreased to 0.31 $\sigma_{v,0}$ and were maintained at that level until draw strategy changed.

For Load cells 3 and 4, located under the stagnant zone (*Wr*), vertical stresses were increased to 1.86 $\sigma_{v,0}$ and 1.51 $\sigma_{v,0}$, respectively. The difference could have occurred because load cell 4 was closer to a movement zone. Afterwards, as the moving front approached the location of the cells, the load decreased as much as 0.9 times from its original value. At the end of the experiment, when drawing from extraction drifts 4 to 6 started, the vertical stress of these cells decreased 0.36 and 0.39 times from their original value, respectively.

At the end of the experiment (around 95 kg), extraction from the EDs 1 to 3 and 7 to 9 was stopped and EDs 4 to 6 were drawn. A subsequent increase of vertical stresses on these cells was observed, reaching 0.6 to 1.1 of their initial value.

Load cell 3 registered the highest vertical stress on this test. It was placed in the middle of the stagnant zone. In this case, induced vertical stresses increased up to 1.86 $\sigma_{v,0}$ and decreased continuously due to the mass removal from the system. Then, when extraction drifts 4 to 6 were drawn, the induced vertical stress decreased to 0.35 $\sigma_{v,0}$.

3.3.2 Test 3: Non-ideal draw with 30 m of unmoved zone
In this test, the same strategy as test 2 was used, but with a minor unmoved zone to quantify higher induced vertical stress, and the relation between the draw and non-draw areas as indicated in theory [39]. Here, only ED5 was not drawn (Figure 15), while other EDs were under draw. A small pillar was induced with draw strategy. One load cell was located within the non-draw zone (load cell 3 in Figure 15-b, through ED5 considering the El Teniente layout), while the other four load cells were located in draw zones over the crown pillar.
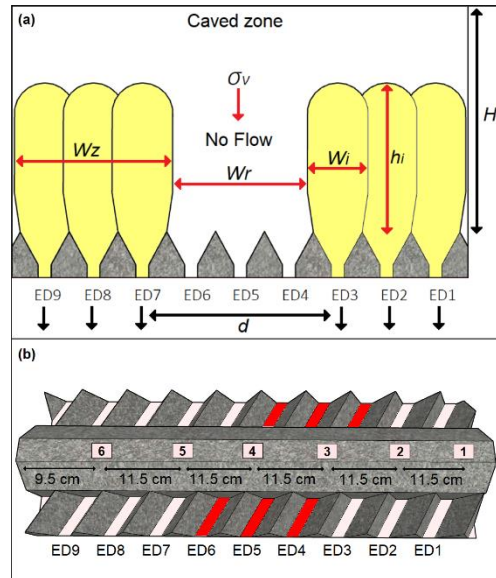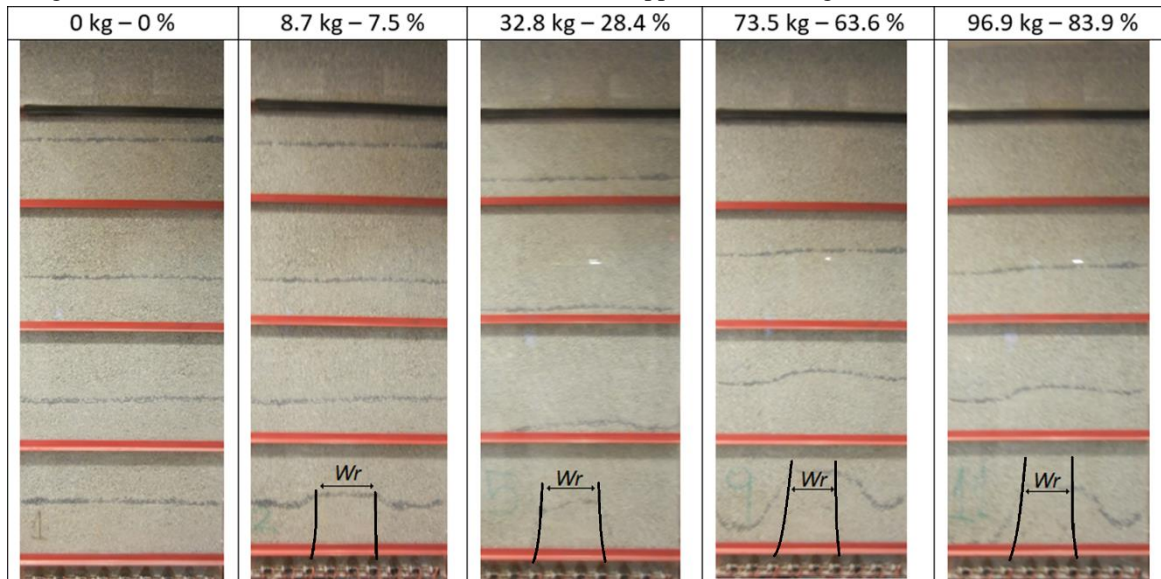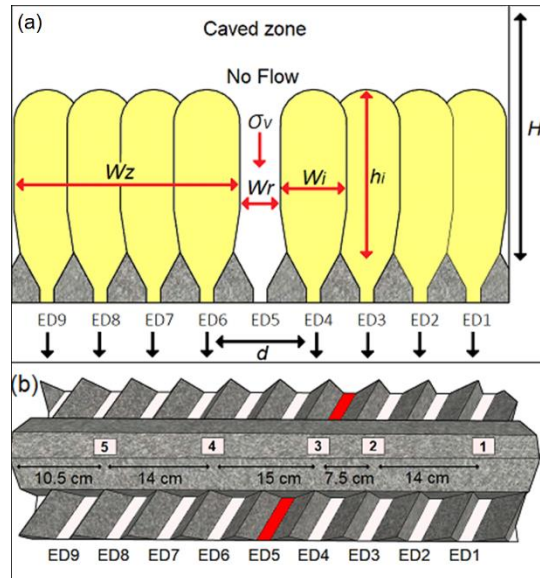
Figure 15. (a) Block caving draw strategy configuration with high non-draw zone (front view) and (b) Load cell location over crown pillar.

The evolution of flow zones showed that the no-flow zone rapidly disappeared as flow zones interacted leaving only a small, unmoved zone. In Figure 16 it can be seen that the flow zones from both draw areas are interacting.
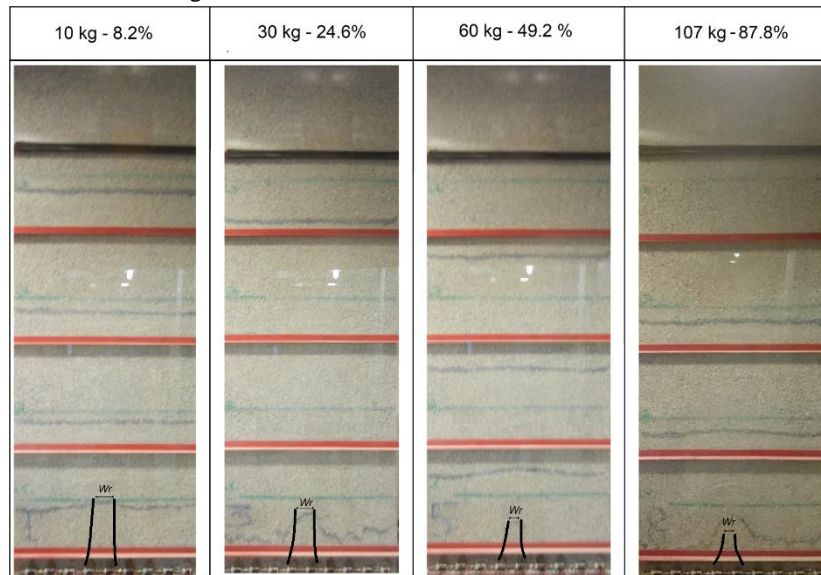
Figure 16. Test 3 draw evolution in Block caving draw strategy (30 m).

From the measurements of load cells shown in Figure 17, the vertical stress behaviour was as follows:
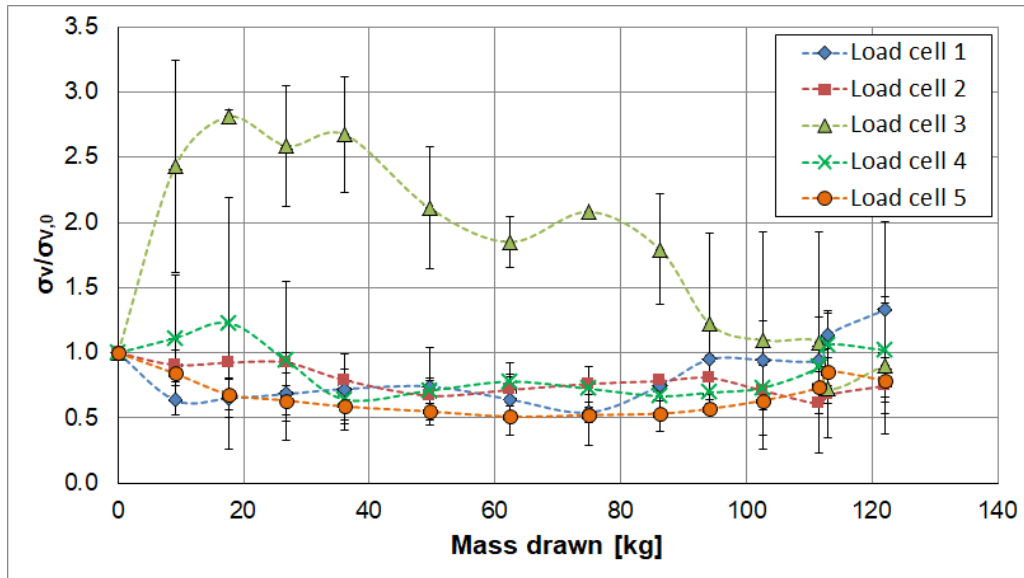
Figure 17. Induced vertical stresses by mass drawn on load cells 1 to 5. Here, σ_v: vertical stress, $\sigma_{v,0}$: initial vertical stress.

Load cell 3 was located in the permanent unmoved zone. In this case the induced vertical stress increased up to 2.81 $\sigma_{v,0}$. After 20 kg of continuous draw, the movement zones overlapped over cell 3. The stress here then decreased but was still higher than at its initial value (see Figure 17). At the end of the experiment, after 100 kg of extraction, an extraction drift below this cell was opened, and drawing started. In this case, the stress decreased as much as 45% from its original value.

Load cells 1, 2, 4 and 5 were placed below the flow zone and all these cells showed a decrease in their stresses. The induced vertical stress of these cells decreased by around 45% from their original values. When extraction drift 5 was opened, the other extraction drifts were closed, and induced vertical stress in these cells increased from 0.8 to 1.4 $\sigma_{v,0}$.

4 Discussion

This study quantified the effect of key variables on induced vertical stresses in granular material. These variables are the presence of unmoved and moved areas, mass drawn, and distance to the extraction front from any point in the unmoved and moved zones. Although previous studies have suggested a relationship among the variables studied, few physical models have been used to actually measure the effects of these variables on induced stresses on granular material related to draw policies. Our study also took into consideration different draw strategies commonly used in block and panel caving mines.

Figure 18 shows the induced vertical stress measured in the stagnant zone, $\sigma_V(SZ - exp)$, and in the movement zone, $\sigma_V(MZ - exp)$, from Test 1: Panel caving draw strategy. Here, Eq. 6 is used to compare induced stress estimated with vertical stress measured in the movement zone, showing a good correlation with a standard deviation of 2.3. Additionally, the vertical stresses in the movement zone are calculated with the Janssen approach presented in Eq. 1 [39]. A good fit is obtained considering k as $(1-sen\phi)$ and u as 2.6, i.e. vertical stress is higher than horizontal stress on the movement zone of this experiment. In addition, a good fit can also be obtained using Eq. 3. Figure 18 shows results until 22 kg to avoid variation on stresses due to loss of weight.
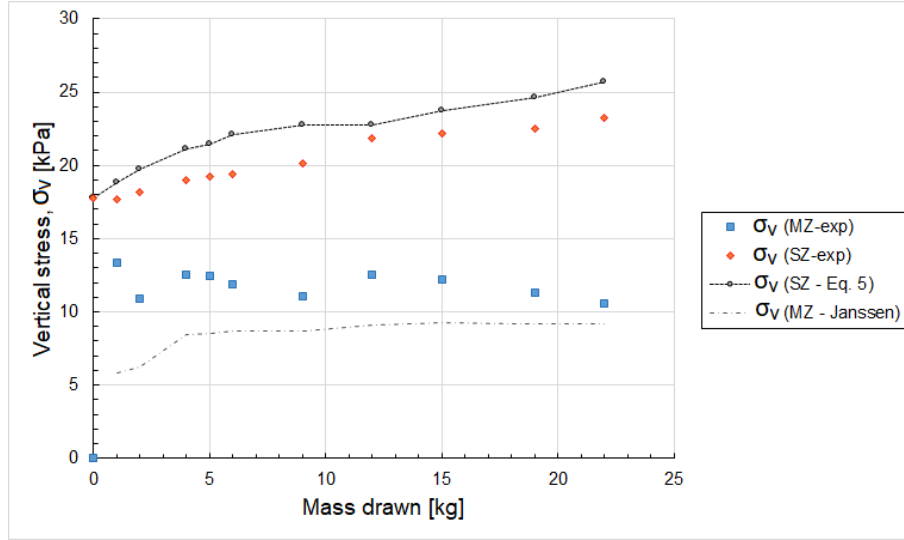
Figure 18. Induced-vertical stresses in movement and stagnant zones.

To analyse the induced vertical stress in block caving strategies and compare this with the results obtained in panel caving strategies, induced vertical stress in the stagnant zone, σ_v^{SZ} is calculated rewriting Eq. 6 and normalizing it by the initial vertical stress, σ_{v0} as,

$$\frac{\sigma_v^{SZ}}{\sigma_{v0}} = \left(A_T - \frac{\sum \sigma_v^{MZ} A_{MZ}}{\sigma_{v0}} \right) \frac{1}{A_{SZ}} \tag{7}$$

Where σ_{v0} is the initial vertical stress, A_T is the total caved area, σ_v^{MZ} is the vertical stress in the movement zone, A_{MZ} is the area of the movement zone and A_{sz} is the area of the stagnant zone. It should be noted that the induced vertical stress in the stagnant zone increases when the area of the stagnant zone decreases. Additionally, in the stagnant zone the induced vertical stress depends on the vertical stress in the movement zone. This relation between the induced vertical stress in the stagnant zone and its area is shown in the draw test in Figure 19.
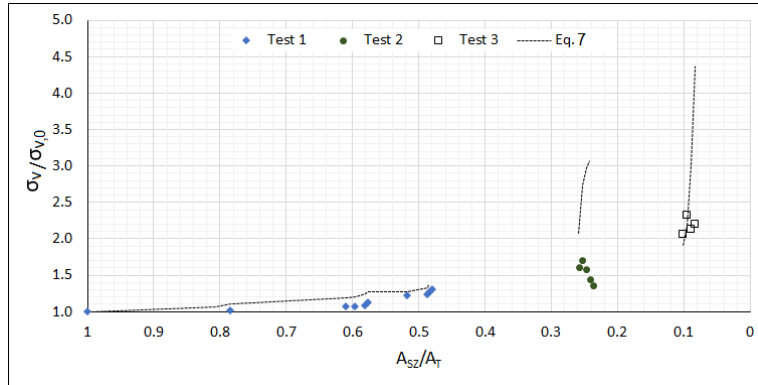
Figure 19. Induced-vertical stresses over stagnant zone relative to total area

Figure 19 shows the vertical stress measured in the stagnant zone in Test 1, 2 and 3, and the induced vertical stress calculated using Eq. 7, which used vertical stress measured in the movement zone of tests. As observed previously in Figure 18, induced stress correlates well with the panel caving strategy in Figure 19. However, in block caving tests, Eq. 7 overestimates the induced vertical stress. The overestimation of induced stress may occur because when both movement zones are in contact, the stress related to the initial density of the material is decreased in the stagnant zone.

The results obtained from this experimental set up can be used to define extraction policies to alleviate induced vertical stresses within caved materials. Based on our results, one such strategy would be to increase the unmoved area proximal to drawpoints to allow vertical stress to act on a larger area. Another strategy would be to draw from unmoved zones to decrease stress.

Many other interesting variables were not included in our study whose main objective was to quantify induced stress due to ore draw under controlled conditions. It would be useful in future studies to observe the effects of variables such as humidity, draw rates and uniformity of draw on induced stress. Furthermore, findings from this study suggest other related studies. For example, future set ups could be constructed to more deeply analyze production pillar stability and the influence of shear zones during ore draw.

5 Conclusions

In the flow zones of the different draw strategies, lower vertical stresses were measured, and consequently, as expected, there were higher vertical stresses under no-flow zones. The size of the unmoved or moved areas influenced the magnitude of the induced vertical stresses. While the unmoved zone width decreased, the vertical stresses increased here, and this was observed both in block caving and panel caving draw strategies.

In block caving strategies, it was found that vertical stress could increase between 2 and 3 times its initial value when different unmoved zone widths were tested. On the other hand, with regard to panel caving, the maximum vertical stress measured was found to be a function of the distance to the front of the draw zone and could reach values close to 2 times initial values. Knowing these magnitudes, not only can extraction policies be used to alleviate induced stress but also the maximum stress that can be expected on the production-level pillars can be estimated in the beginning stages of a project. Then, support systems could be designed according to these requirements, thus avoiding problems like those described by Sahupala et al. [57], Bravo [168], Pierce [59], and most likely in various other unpublished cases.

Paper 4: Stress modelling using cellular automata for block caving applications

René Gómez, Raúl Castro

Abstract

In underground mining, rock mass stress is commonly modeled as a continuum. However, in block cave mining discrete modelling should be used to properly represent the stress over the extraction level in the broken column where there are high rock columns of large rock fragments. Unfortunately, we lack methods that use discrete modeling of stress in the broken column at block caving scale. In this work, we propose a vertical stress model of granular material to simulate static and dynamic flow conditions. The model is developed within a gravity flow simulator based on cellular automata to simulate the scale of the problem and flow conditions. The vertical stress model proposed is calibrated through four experimental models for the static condition. Then, based on the results from experimental testing, the dynamic condition is calibrated and compared with different flow scenarios. The results show that the proposed model can correctly simulate the vertical stresses in static conditions as well as dynamic conditions under the different flow setups tested. This vertical stress model with its flow simulator based on cellular automata has the potential to be applied at block caving scale once calibration parameters are defined.

Key words: Caving, cellular automata, granular material, gravity flow, stress modelling.

List of symbols
2D: Two dimensions
3D: Three dimensions
β_i: Weight distribution function
ϕ_w: Friction wall [°]
σ_v: vertical stress
σ_{v0}: Initial vertical stress
γ_i: specific gravity
CA: Cellular automata
DEM: Distinct element method
d_{ij}: distance between cell i and j.
B: Stress model parameter in stagnant zone
B_{min}: Stress model parameter in movement zone
H: Model height
h_i: Height of movement zone
IMZ: Isolated movement zone
MZ: Movement zone
n: number of cells in vertical axis
P_i: Weight
P_T: Total weight
P_V: vertical weight transmitted
R: Relaxation parameter
s: Stress model parameter (in stagnant and/or movement zone)
V: Cell volume
W_r: Stagnant zone width
W_i: Movement zone width

1.- Introduction and literature review

Studies of stress in granular material have been carried out for many years due to this material's importance in many industries (i.e. Food[136], Pharmacy[137], Mining[138]). In block cave mining, the granular material is composed of large rock fragments within a broken column of hundreds of meters. Thus, a soil mechanics approach has been proposed to estimate stress in the caved column [33], [54], [59], [261], using the corrected classic Janssen approach[39] as an initial stress estimation. Nevertheless, the stress modeling of a broken

column is more complex when different rock types, draw strategies, and complex cave geometries have to be considered.

A common tool used to study complex granular media problems is the distinct element method (DEM; [180]), frequently used in stress studies (e.g: [150], [298]–[303]). DEM has also been used in mining studies[50], [52], [55], [83]. However, in cave mining studies[50], [52], [55], the problems have been limited to a drawbell, a short column height and simplified shape fragments because of the problem of scale. As an example in [50], a draw simulation of a cylindrical model of 0.7 m height and 0.34 m diameter takes between a week and a month to complete. Other numerical tools are used for large scale problems that quickly simulate the ore flow without considering dynamic interaction between particles, such as PCBC[304], CAVESIM[9], FLOWSIM[10], and REBOP[54].

Stress has also been measured in the extraction level of block cave mines [163], [169], [170] with different techniques for field stress measurement such as stress cells, over-coring, the Flat Jack test, and hydraulic fracturing [305], [306]. Rojas et al. [163] used stress cells in the Esmeralda mine (within the El Teniente mine) and identified the need for production pillar rehabilitation after abutment stress to provide support during ore extraction. Xia et al. [170] also studied the stability of the extraction level before and after undercutting in the Tongkaungyu mine using over-coring. In this mine, the stability problems mainly occurred during the undercutting, but stability problems were also reported during ore extraction. Additionally, indirect techniques have been applied. Martin et al. [172] proposed stress model calibration based on the drift damage and the depth of failure, while Gonzales et al. [173] used the damage observed in borehole cameras to model stress. In the Deep Ore Zone mine, they measured production drift convergence [174], where stress concentration during ore extraction was observed. Another indirect technique was proposed by Xia et al. [175] to estimate stress in the extraction level through the thin plate theory.

During ore extraction induced stress is, directly or indirectly, observed in the extraction level. Moreover, damage from stress has been reported in this level [57]–[59]. Stress measurement is useful during mining; however, it would also be useful to estimate stress in previous stages. DEM are not preferable yet for full block cave scales because of the time required for simulation. Thus, in this work we propose to incorporate a vertical stress model in a gravity flow simulator based on cellular automata (CA) that will be able to quickly model vertical stress in high draw columns under different draw scenarios.

2.- Stochastic stress model through Cellular Automata

Granular media can be described by stochastic interactions [2] mainly due to their random shapes, sizes, contact points and contact forces [3]. However, this randomness follows a degree of regularity, which has allowed stochastic models of granular material flow [2], [4]–[6], [181] and stress in granular material [307]–[309]¡**Error! No se encuentra el origen de la referencia.** to be developed.

In mining, the stochastic rules used for gravity flow have been applied through Cellular Automata (CA) [7]–[16]. Gravity flow modelling with CA is based on the void diffusion mechanism [97]. This mechanism has been identified in Block and Sublevel caving mines [18]–[20], [22], [44], [190], including in fine material fragmentation (< 0.4 mm [24]). CA have also been used for a wide variety of complex matter in models such as rough annular shear cells, lattice-gas, lattice-grain, hybrid models, movable CA, elasto-plastic rock failure, Continuous-discontinuous CA and [25]–[30], [310]–[312].

In granular materials, the stresses are transmitted by chain forces due to the media inhomogeneity [307], [313], that generates stochastic stress distribution. Liu et al. [307] and Coppersmith et al. [308] proposed stress modeling in granular material by CA, through stochastic weight transmitted downward between particles, without considering the coordination number. Then, Hemmingsson et al. [309] applied force vectors to model the vertical forces transition reporting favorable results in silo and heap geometries of granular material.

In this work, we applied the weight transition through cells in a CA to simulate gravity flow in caving mines [11], [16]. The gravity flow propagated during ore extraction was simulated using the void diffusion concept. The voids are inserted in draw points and have a probability of moving upwards and exchanging location with a non-void (granular) cell. Inversely, the weight of a (granular) cell is distributed randomly among lower cells (as shown in **Figure 6** in 2D). The weight is distributed only over non-void cells. In **Figure 6**, a cell in the *i*

level distributed its weight, P_i, over a lower cell in the j level. The weight is a function of the specific gravity, γ_i, and the cell volume, V. Additionally, shear forces (by friction) and horizontal forces could be considered. However, in this work only vertical force transmission was modeled. The vertical stress model was applied in a cubic lattice of cells where a cell distributed its weight over 9 lower cells (in 3D).
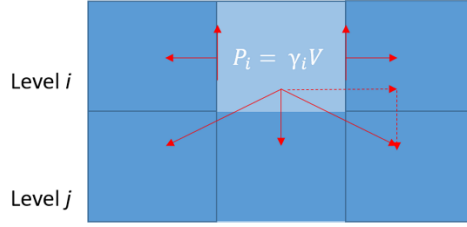
Figure 6 Profile view (2D) of weight transmission in a cell lattice, the red arrows represent the force transmissions of a cell.

The vertical forces in the model are the weight components (by gravity) and the shear components (by friction). The shear components support part of the individual cell's weight. Here, we simplified the weight transmission introducing a buoyant parameter, E, that represents the weight fraction of a cell that is distributed to lower cells. Then, $1 - E$ is the cell's weight fraction that is supported by friction. The cell's weight distributed to lower cells is represented by Eq. 1.

$$\gamma_i - \gamma i \cdot (1 - E) = \gamma i \cdot E \qquad E = \{0,1\} \tag{1}$$

Then, the weight of a cell in level j is its weight plus the weight fractions of the nine upper cells (in 3D; Eq. 2).

$$P_j = \gamma_j V + E \sum_{i=1}^{9} P_i \beta_i \tag{2}$$

P_j is the weight of cell j and βi is the weight fraction of the cell i transmitted to cell j. βi is defined by the multinomial probability distribution in Eq. 3,

$$\beta(x_j) = \frac{n!}{\prod_{j=1}^{k} x_j!} \prod_{j=1}^{k} p_j^{x_j} \tag{3}$$

where $k = \{1, \ldots, 9\}$, $x_j = d_{ij}$ is the distance between cells i and j, n is the sum of the nine distances as $n = \sum_{j=1}^{k} x_j$, and p_j are the initial probabilities of the nine cells defined here as an inverse function of the distance (Eq. 4), similar to the void diffusion rule used in the flow simulator [11].

$$p_j = \frac{\left(1/d_{ji}\right)^s}{\Sigma\left(1/d_{ji}\right)^s} \tag{4}$$

In Eq. 4, s is a model parameter that must be calibrated. The influence of this parameter on the force distribution (β_i) is shown in **Figure 7** as a function of the distance between cells.

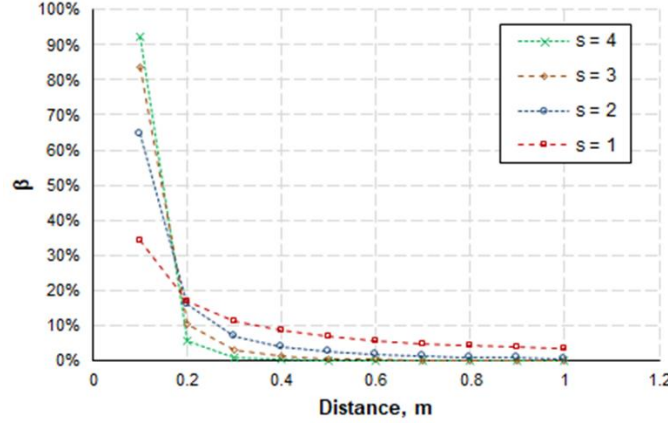**Figure 7 Effect of *s* on the force distribution parameter.**

As can be observed in **Figure 7**, the weight fraction received from upper cells decreased for larger distances between cells. The weight fraction distributed near the model boundary is omitted as was proposed by Hemmingsson et al. [309] because the wall friction (at the boundary) generates equal force in opposite directions. Additionally, the weight supported by nearby cells increases when *s* increases. Higher variability could be added to the model using a random *s*. However, this variability should not highly influence the mean vertical stress calculated in a level.

2.1 Cell lattice influence

The gravity flow simulator used a cubic cell lattice (**Figure 8**A), in which the cell weight is transmitted level by level through the Y direction applying the buoyant parameter *E*. Then, the cell size and the total height both influence the vertical stress transmitted to the next lower level for a specific E value. This influence is shown in **Figure 8**B for a fixed height (*H*). There is a cumulative effect of the *E* parameter when the cell weight is transmitted: the total weight, P_T, transmitted at the very bottom is decreased based on the number of cells in the vertical axis due to the parameter *E*.
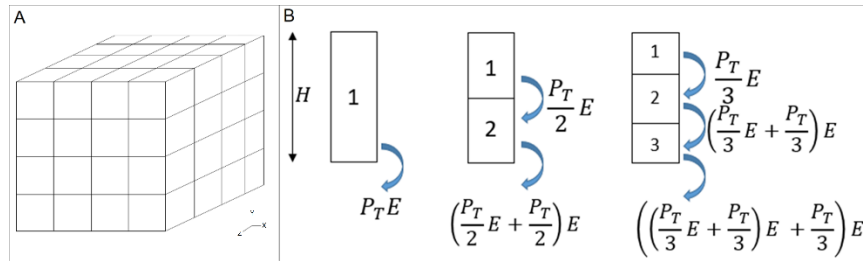
Figure 8 A: Cubic cell lattice. B: Cumulative effect of parameter *E* as function of the cell lattice and model height.

Using the stress model, the weight calculated at the bottom, P_V, can be related to the total system weight, P_T, and to the number of cells in the vertical axis, *n*, as shown in Eq. 5.

$$Pv = \sum_{i=1}^{n} \frac{P_T}{n} E^{(i)} \xrightarrow{n \to \infty} P_T ln\left(\frac{1}{1-E}\right) = P_T \frac{E}{n} \frac{1-E^n}{1-E} \tag{5}$$

2.2 Stress modelling during gravity flow

The proposed stress model is defined for static granular material. However, as we have seen in previous studies, vertical stress increases in the stagnant zones and decreases in the movement zones when gravity flow begins due to ore extraction [33], [52], [54], [70]. One reason is that the movement zones have less bulk density [217], [314], [315], decreasing the contact points between particles for force transmission. In our stress model, we introduce a relaxation parameter, *R* (between 0 and 1), to model the weight distribution between the movement and stagnant zones. This parameter should depend on the rock properties and system geometry. The *R* parameter

decreases the probability of weight distribution over the movement zone when there is a cell (or more) located in the stagnant zone (**Figure 9**). The weight distribution of a cell, defined by Eq. 3, over a cell in the movement zone is multiplied by R to decrease the weight transmitted over this cell. The weight distribution defined by β_i must sum 100% to avoid weight losses for this rule, assuming that $P_1 + P_2R = 100\%$ (in **Figure 9** example for 2D). The weight is distributed mainly over the stagnant zones by including this R parameter.

Figure 9 Profile view (2D) of mass transmission in a six-cell arrangement with stagnant and movement zones (cells)

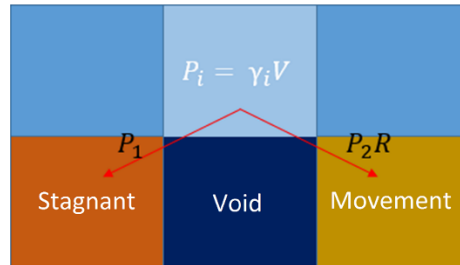Additionally, the height of the model influences E (as described in section 2.1). Thus, the movement zone height also influences E. Then, we defined E_{min}, for the buoyant parameter in the movement zone that depends on the movement zone height. Finally, the parameters R and E_{min} are used to model stress under flow conditions.

3.- Experimental methodology
Four physical models were simulated in the gravity flow simulator applying the stress model. The vertical stress measurements obtained from the physical models were then used to calibrate the parameter E in the static condition. The physical model of Castro et al. [70] was selected to calibrate the parameters E_{min} and R because in this model different flow scenarios were tested. Finally, the numerical model calibrated in static and dynamic conditions was compared with different flow scenarios. Python V3.7 was used in this work to build the CA stress model.

3.1 Physical models
The data obtained from the physical models were used in this study to calibrate the stress model. Three of the physical models were selected because stress for block caving applications had previously been measured [33], [70], [238]. Additionally, a fourth physical model (Seditest) was used in this work to vary the effect of the wall friction and material properties.

The setup of the Seditest model consists of an acrylic column shown in Figure 5, with a height of 50 cm and 10 x 8 cm^2 square-cross section. At the bottom of the column a load sensor (Danfoss MBS 4510-060G2418) is located. A feeder is used to fill the column with the granular material (Fig. 5-B). Glass spheres and gravel were used as granular material. Additionally, three materials were used in the model walls to modify the wall roughness: paperboard, a fine sandpaper, and a coarse sandpaper.
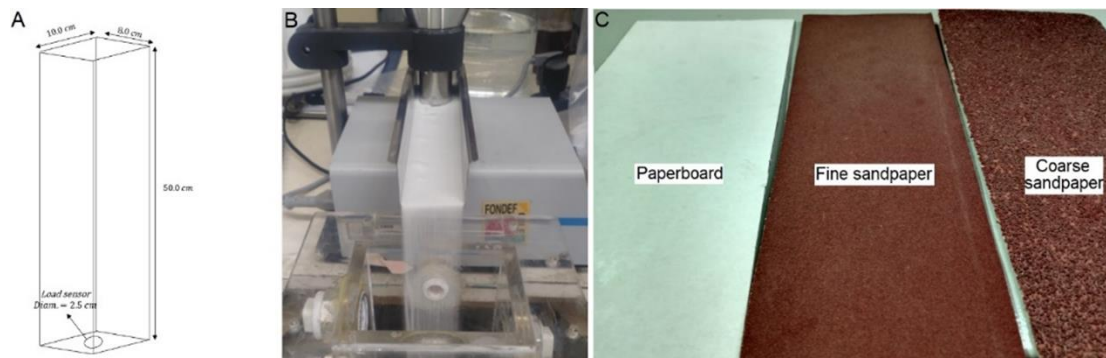

Figure 10 A: Column model dimensions. B: Feeder system used to fill the model. C: Wall's material.

The other three physical models used to calibrate the stress model are presented in **Figure 11**. In these models, the vertical stress was measured in the base around drawpoints or over drawbells. All experiments demonstrated high variability of stress measurements. **Table 1** indicates the physical model dimensions and granular media used.
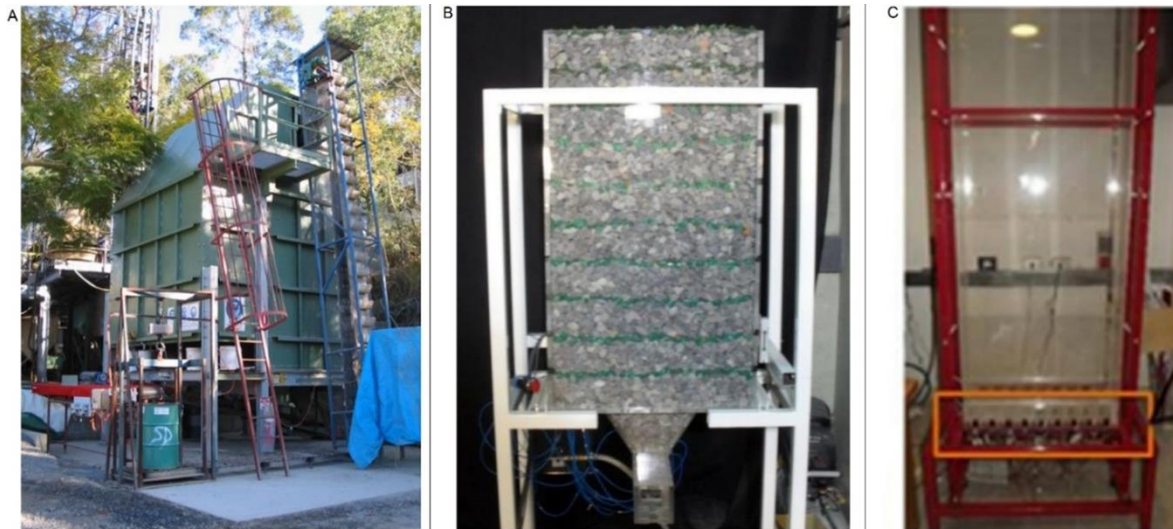
Figure 11. Physical models used in this study. A: Castro [33]. B: Orellana [238]. C: Castro et al. [70].

Table 1 Model dimensions

Dimension	**Castro [33]**	**Orellana [238]**	**Castro et al. [70]**
Height [m]	2.4	1	2.5
Width [m]	3.4	0.54	0.7
Length [m]	3.3	0.35	0.23
Granular material	Gravel	Gravel	Sulphide ore

Table 2 indicates the material characteristics used in the models of **Figure 11** and the Seditest. In the Seditest, two granular materials were used: glass spheres and gravel. The gravel was previously fragmented and sieved. The real density and bulk density of the material were measured [316]. A simple shear test using a shear box (10 x 10 cm^2) was used to measure the undrained shear properties [282].

Table 2 Summary of granular material properties

Parameter	**Castro [33]**	**Orellana [238]**	**Castro et al. [70]**	**Glass sphere**	**Gravel**
Real density, kg/m^3	2700	2690	2600	2500	2670
Bulk density, kg/m^3	1900	1610	1420	1150	970
Particle size, mm	[4-14]	[7-35]	[0.8-11]	0.6	[2.36 - 4.7]
Internal friction angle, °	39	ND	39	27.2	37.9
Angle of repose, °	ND	28.9	29	21.1	40.1

ND: No data

The friction between the granular materials and the wall materials, ϕ_w, was measured using the tilting methodology proposed by Nedderman [142]. It is assumed that this value is the static friction wall angle parameter for the maximum angle before sliding. Table 3 shows the friction wall angle obtained for the material used in the Seditest model. The friction wall angles increase as wall roughness increases for all granular materials tested as was expected. The friction wall angles were also reported to be 25° [70] and 19.7° [238], respectively. The friction angle between the wall and the material is higher than the internal friction angle of

the glass spheres when coarse sandpaper is used and is also higher for gravel when fine and coarse sandpapers are used.

Table 3 Friction wall angles (º) in the Seditest model

Materials	Paperboard	Fine sandpaper	Coarse sandpaper
Glass spheres	19.0±0	24.0±0.2	31.5±0.7
Gravel	32.3±0.6	41.3±2.3	42.7±1.5

In the Seditest model, the filling time per test was 2 minutes. After filling the column, the vertical stress was measured for 10 minutes, during which no changes of vertical stress measurement were observed. A total of 6 combinations of wall and granular materials were used, each combination was repeated 3 times for a total of 18 tests.

3.2 Stress data
The stress data reported in Castro [33], Orellana [238], Castro et al. [70] and Seditest are shown in **Table 4**. Here the mean vertical stress measured in the static condition (i.e. before flow) is presented.

Table 4 Vertical stress reported in physical models

Test	Model	Mean vertical stress [kPa]	Standard deviation [kPa]
1	Castro [33]	32.49	15.57
2	Orellana [238]	8.4	6.98
3	Castro et al. [70]	19.65	5.58
4	Seditest gravel (ϕ_w = 32.3°)	0.48	0.07
5	Seditest gravel (ϕ_w = 41.3°)	0.38	0.05
6	Seditest gravel (ϕ_w = 42.7°)	0.36	0.08
7	Seditest glass (ϕ_w = 19.0°)	0.68	0.01
8	Seditest glass (ϕ_w = 24.0°)	0.62	0.03
9	Seditest glass (ϕ_w = 31.5°)	0.54	0.01

In the Seditest model, the vertical stress was also measured during filling at different heights. A Janssen effect was observed in all tests. Figure 12 shows the results of the glass spheres and gravel for all wall materials. The vertical stress measured on glass spheres increased during filling. The effect of the wall roughness is observed between the paperboard and coarse sandpaper material wall. The results of the fine sandpaper showed a high variability; however, the mean stress values fall between the other wall materials. The gravel showed lower vertical stress than glass spheres. The gravel and glass spheres have a similar bulk density (970 and 1150 kg/m³, respectively), but the glass spheres have lower friction wall angles, which could explain why glass spheres demonstrate higher vertical stress.
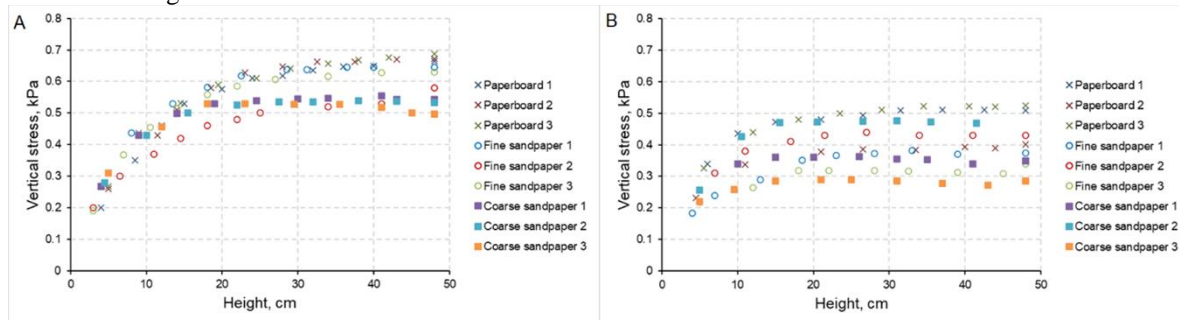
Figure 12 Vertical stress reported in the Seditest model, 3 replications per test. A: Glass spheres and B: Gravel.

3.3 Stress model calibration

The physical models presented in section 3.1 were simulated numerically to calibrate the stress model. The parameter E (Eq. 2) was calibrated through the mean vertical stress reported whereas the parameter s (Eq. 4) was calibrated through the standard deviation of the vertical stress reported. The mean square error was minimized to calibrate both parameters (E and s) between the vertical stress from experiments and numerical simulations, using Eq. 6 [274].

$$min \sum_{j=1}^{m} \left(\sigma_{v,exp} - \sigma_{v,sim}\right)^2 \qquad (6)$$

Here, $\sigma_{v,exp}$ is the experimental mean vertical stress, and $\sigma_{v,sim}$ is the simulated mean vertical stress in the CA model. Ten simulations were run per test as shown in **Table 4**. The cell size used is 2x2x2 cm^3 in all tests except in test 1 [33], in which the cell size used was 10x10x10 cm^3. The simulation time for the static condition is less than 1 minute and approximately five minutes for the draw condition (varying depending on the draw scenario).

First the block model for each test is created which includes the model size and the cell properties (such as cell ID, cell state, cell density, d$_{50}$). Then, the stresses are calculated in the static condition using the cell densities and equations 1 to 4, in which the equations' parameters are calibrated with experimental data. In the flow condition, gravity flow is simulated first, and then the stresses are calculated as mentioned above.

4.- Results

4.1 Before flow: Static calibration

Table 5 shows the experimental and simulated results, as well as the calibrated parameters E and s. Here, the parameter s was modeled using a normal distribution function (Eq. 7; [317]) to obtain the experimental variability of vertical stress. The parameter E increased with the height of the model (H), decreasing its effect as indicated in section 2.1.

$$p(x) = \frac{1}{\sigma\sqrt{2\pi}} exp\left(-\frac{1}{2}\left(\frac{x-\mu}{\sigma}\right)^2\right) \qquad \forall x \in \mathbb{R} \qquad (7)$$

In this Eq. 7, μ is the mean and σ is the deviation, commonly denoted by $N(\mu, \sigma)$.

Table 5 Numerical model calibration: static condition

Parameter	Castro [33]	Orellana [238]	Castro et al. [70]	Seditest Gravel			Seditest Glass Spheres		
				$\phi_w = 32.3°$	$\phi_w = 41.3°$	$\phi_w = 42.7°$	$\phi_w = 19°$	$\phi_w = 24°$	$\phi_w = 31.5°$
Mean vertical stress (experimental)	32.49	8.63	19.65	0.48	0.38	0.36	0.68	0.62	0.54
Mean vertical stress (simulated)	32.44	8.65	19.51	0.48	0.38	0.36	0.68	0.62	0.54
Standard deviation (experimental)	15.57	6.99	5.58	0.07	0.05	0.08	0.01	0.03	0.01
Standard deviation (simulated)	15.62	6.37	5.37	0.08	0.07	0.09	0.05	0.04	0.04
E (%)	99.54	97.21	98.95	54.0	41.8	38.5	71.8	69.1	64.6

s	N[8,7]	N[50,49]	N[4,3]	N[2,0.1]	N[2,0.1]	N[2,0.1]	N[2,0.1]	N[2,0.1]	N[2,0.1]

Figure 13 shows the results of the three models (Test 1, 2 and 3) with the calibrated parameters in static condition. The simulated vertical stress increased with depth (Y axis) under a stochastic behavior between cells. In the plan views of **Figure 13** (Plane XY), high vertical stress variability is observed as was expected from experimental results.
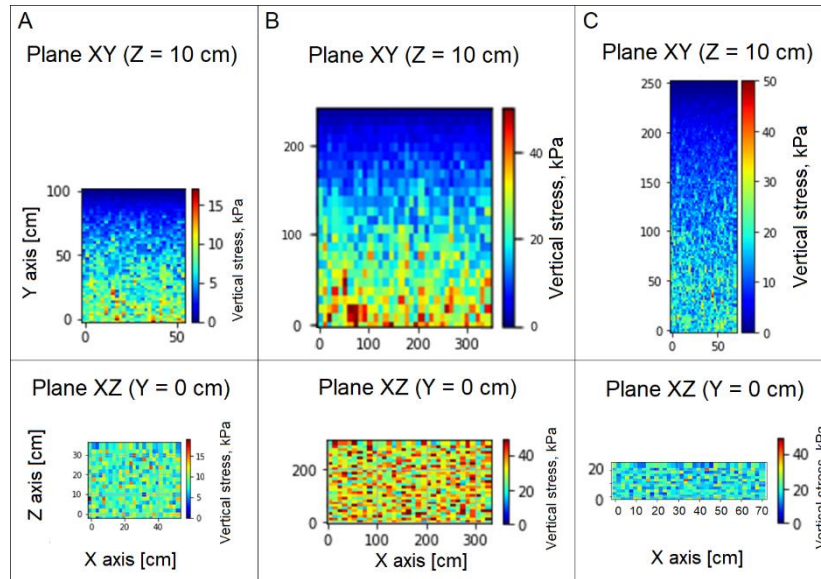
Figure 13 Simulated vertical stress (color legend in kPa) for tests 1, 2 and 3. A: Test 1. B: Test 2. C: Test 3.

Figure 14 shows the numerical calibration of the Seditest. The *E* parameter also depends on wall friction at least for a small hydraulic radius. This effect can be observed in **Figure 15**, where *E* is related to geometrical parameters (*Rh* and *H*) for gravel and ore materials, which have similar friction angles (37.9º - 39º).
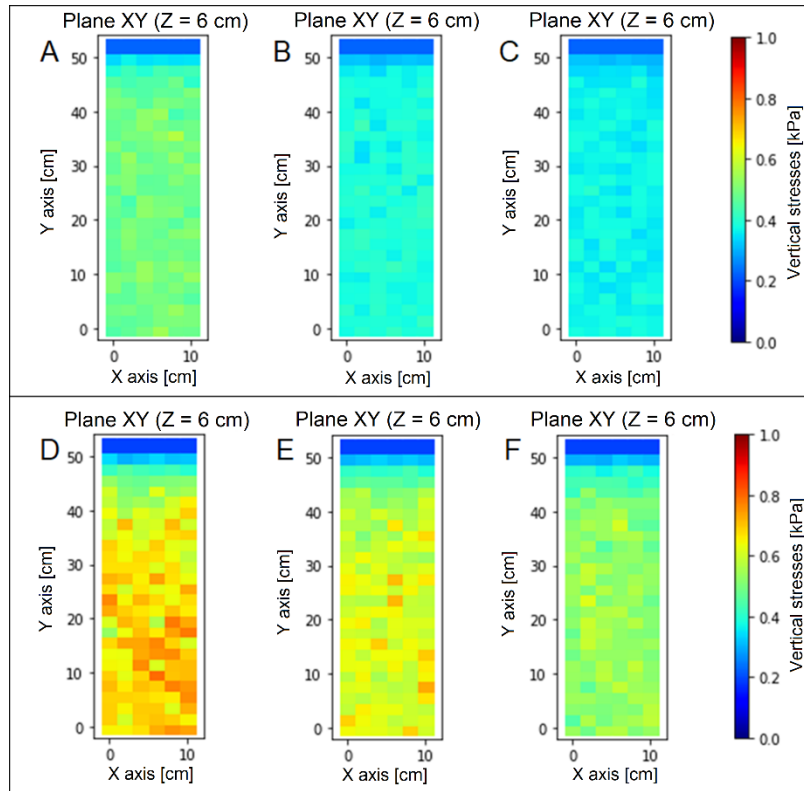
Figure 14 Simulated vertical stress for the Seditest with gravel in A: Test 4. B: Test 5 and C: Test 6, and glass spheres in D: Test 7. E: Test 8 and F: Test 9.

The parameter *E* increases asymptotically to 100% when *Rh* and *H* increased in the geometries modeled. In **Figure 15**, the wall friction influenced *E* (Test 7, 8 and 9), decreasing *E* when the wall friction increased. The different *Rh*H* of the Seditest were obtained based on different granular material heights during filling.
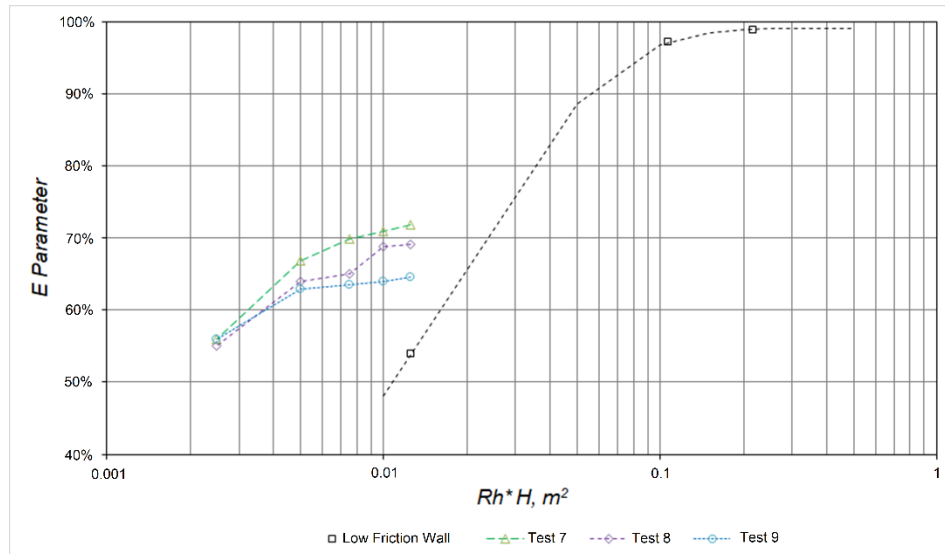
Figure 15 Model geometry and wall-friction effect on *E*. The low friction wall markers correspond to the physical model of Figure 6.

4.2 During flow: Isolated movement zone calibration.

In this section, the parameters E_{min} and R are calibrated as described in Section 2.2. These parameters are calibrated based on Test 1 reported in Castro et al.[70], where isolated extraction was simulated. The calibrated parameters are determined minimizing the error between simulated and experimental vertical stresses (Eq. 6), using the parameter $E = 98.95\%$ previously determined. **Figure 16** shows the physical experiment used, and the calibration of the flow zone geometry (diameter and height) simulated in the gravity flow simulator.
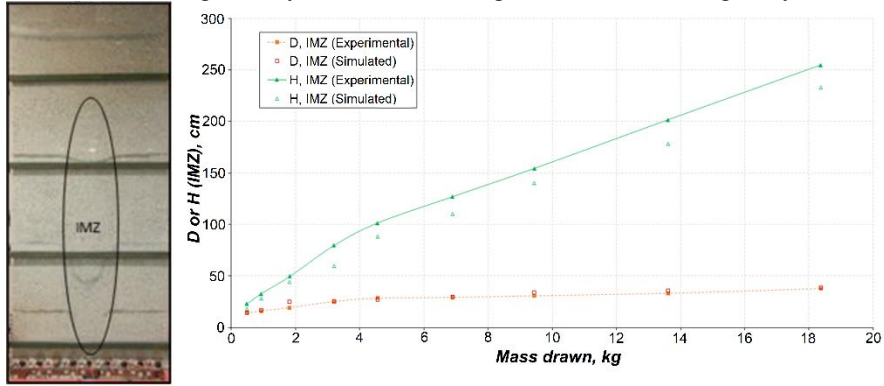
Figure 16 Isolated extraction used to calibrate numerical parameters during flow [70]**.**

The calibrated model of vertical stresses is presented in **Figure 17**. Here the growing of the isolated extraction zone (IMZ) can be observed due to ore extraction from the base of the model. The vertical stress decreased in the movement zone (blue ellipse). On the other hand, vertical stress concentrations are observed in the boundary of the IMZ implying more weight transmission to stagnant zones.
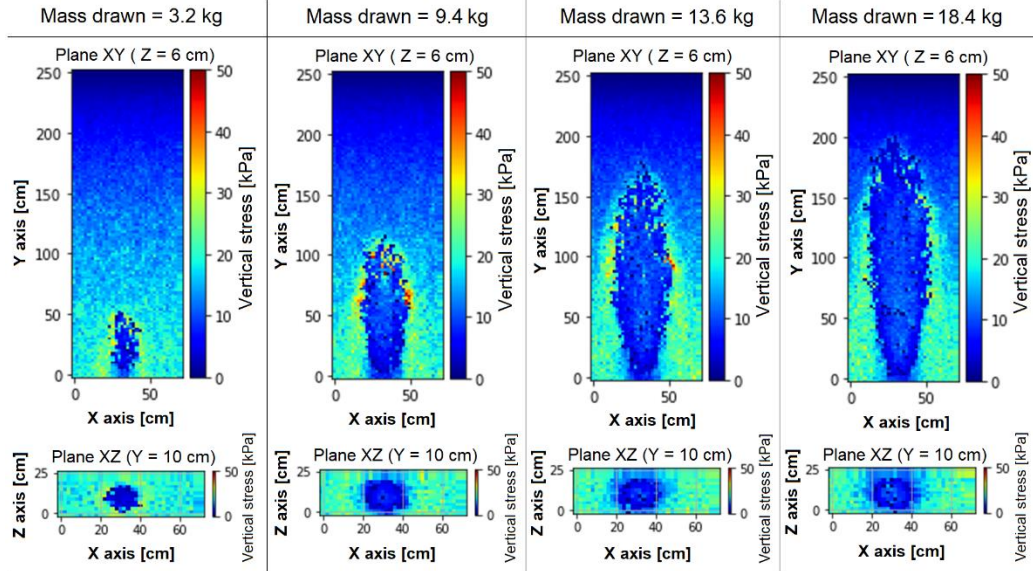
Figure 17 CA simulation of vertical stresses during isolate draw.

This calibration allows the evolution of E_{min} to be determined as function of the height of MZ (**Figure 18**) of this setup. The calibrated parameter R is 0.29. Then, it is possible to evaluate the stress logic under different draw conditions using this experimental setup. In Castro et al. [70] different flow scenarios were reported that can be simulated with the calibrated model, $E = 98.95\%$, $R = 0.29$ and E_{min} based on **Figure 18**.
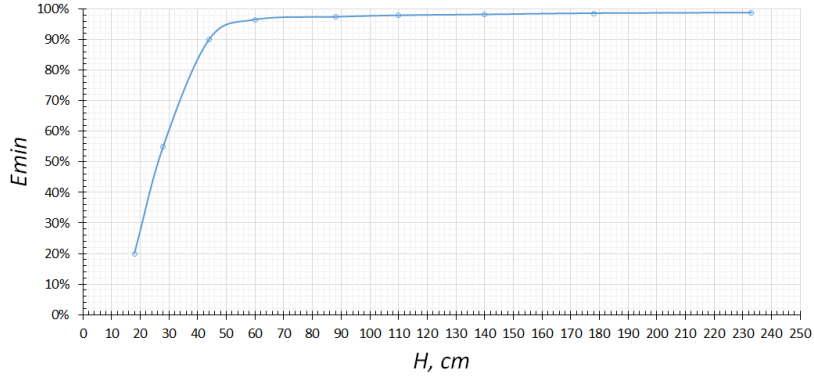
Figure 18 E_{min} **based on IMZ height obtained from isolated experiment by** [70].

5.- Experimental validation

Three flow setups were simulated numerically using the stress model, applying the parameters (E, s, E_{min} and R) calibrated in Section 4. These flow experiments included a Panel Caving draw, a Block Caving draw with non-flow zone of 30 cm (spacing between drawpoints), and a Block Caving draw with a non-flow zone of 15 cm, reported in [70]. In the Panel Caving draw, the granular material was extracted continuously from different drawpoints (Figure 19A). In the Block Caving draw with a non-flow zone (stagnant pillar) of 30 cm, the material was drawn from side drawpoints while the central drawpoints were not extracted (Figure 19B). In the Block Caving draw with a non-flow zone (stagnant pillar) of 15 cm, the material was also drawn from side drawpoints with a smaller non-flow zone (Figure 19C).
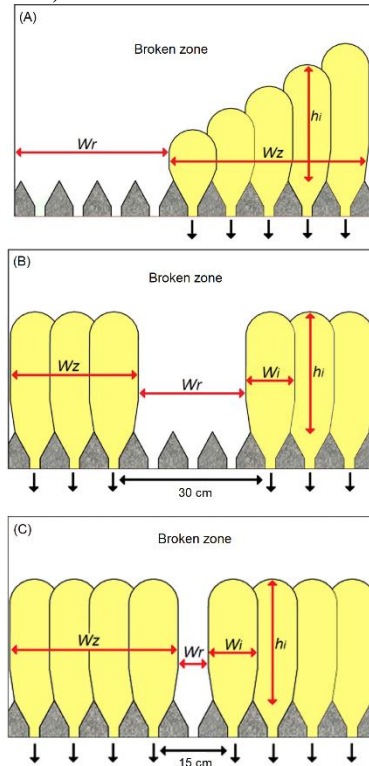
Figure 19 Experimental setup of different draw strategies (modified from [70]**). A. Planel caving strategy. B: Block caving with 30 cm of pillar. C: Block caving with 15 cm of pillar.**

In **Figure 19**, the movement zones generated are indicated in yellow. These zones grow continuously due to ore extraction. The width of the movement zone is denoted by W_Z. W_i is the width of the IMZ, H_i the height of the IMZ, and W_r is the stagnant pillar width. In these experiments, the vertical stresses were measured over the drawbells.

The simulated result of the Panel Caving scenario is presented in **Figure 20**. Lower vertical stress is observed (blue color) in the cells located at the top of the model and in the movement zone, while higher stress concentration can be observed in the stagnant zone.
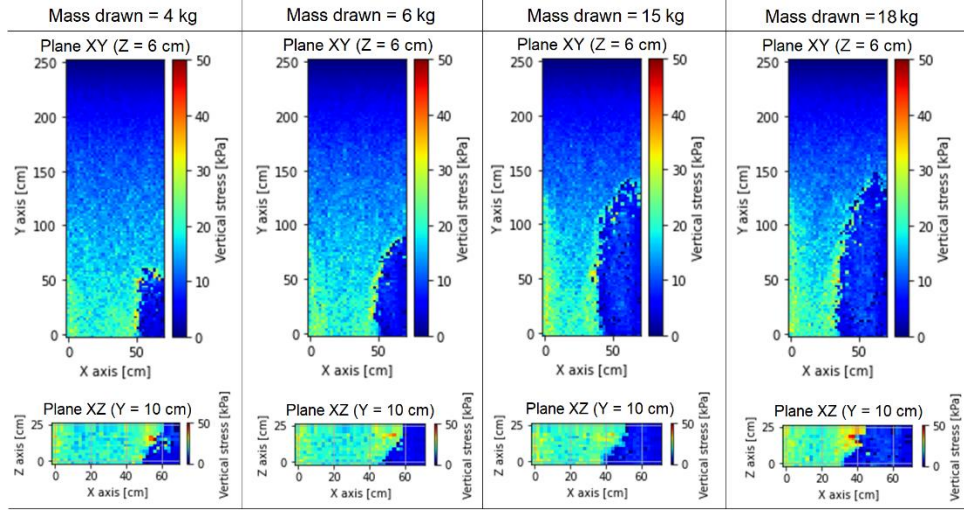
Figure 20 Vertical stress simulation for panel caving draw strategy.

The mean vertical stress is compared between experimental and numerical simulations to analyze the stress model. The mean vertical stress in the numerical model was determined based on five replications per test. The vertical stress in the physical experiments was measured using load cells. The same location of the load cell was used to measure the vertical stress in the numerical model. Figure 21 shows the experimental and numerical results through the ratio between the vertical stress of each cell at this moment of mass draw (σ_v) and the initial vertical stress (σ_{v0}), for six load cells in the Panel Caving scenario. Here, the stress in the movement zone quickly decreased due to draw (load cells 1 and 2) in both the experimental and simulated models. Similarly, the vertical stress is decreased within the movement zone, and this is reflected when the movement zone reaches load cells 3, 4, and 5. On the other hand, the vertical stress is increased in the stagnant zone, until that zone is transformed into a movement zone. This last behavior has also been reported in DEM simulations [52], [55].
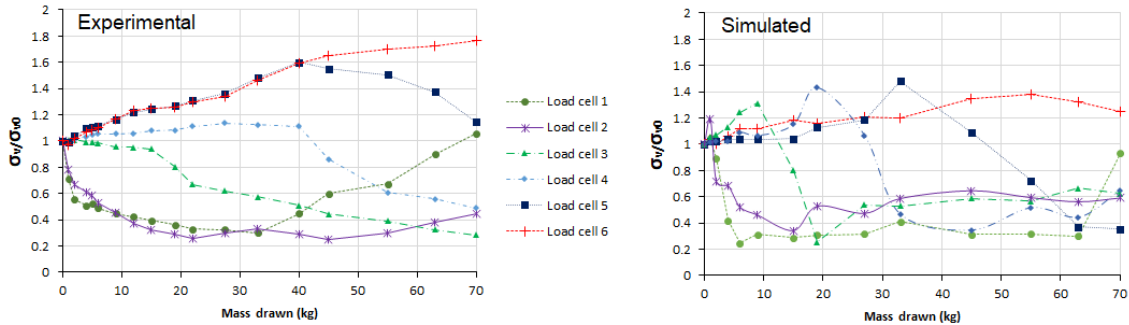
Figure 21 Experimental and numerical simulation of Panel Caving draw scenario.

Figure 22 shows the vertical stress simulated in Block Caving scenarios with a stagnant pillar in the center. The vertical stresses in the movement zones (both sides) decreased during draw, similar to with the Panel Caving draw. On the other hand, in the stagnant zone, the vertical stress increased due to the weight transferred from the movement zones (by parameter R). This weight was transferred to the stagnant zone and continued to the bottom of the model. There are higher stress concentrations in a smaller area when a non-flow zone of 15 cm is utilized (**Figure 22**B; Plane XZ: mass draw 26.9 and 36.1 kg). Then, the vertical stress in this zone decreased because the cells are reached by the movement zone (**Figure 22**; mass draw 49.6 kg).
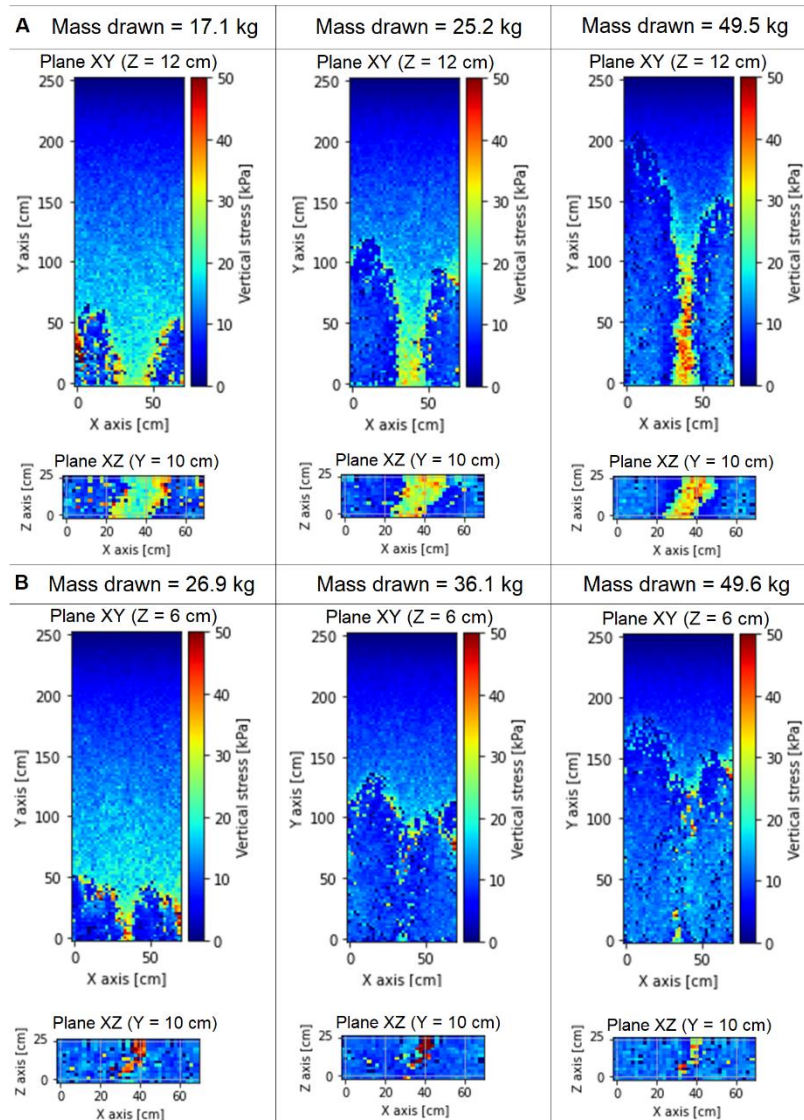
Figure 22 Vertical stress simulation of Block Caving draw strategy. A: 30 cm of spacing and B: 15 cm of spacing.

Figure 23 shows the experimental and numerical results using the ratio between the vertical stress at the moment of draw and the initial vertical stress of the Block Caving scenarios. Here, six load cells were used in the experiment with a stagnant pillar of 30 cm, while five load cells were used in the experiment with 15 cm. In the Block Caving scenario with 30 cm of non-flow zone (Figure 23A), there are two load cells located in the stagnant zone: load cells 3 and 4. These load cells showed higher vertical stress at draw in comparison to their initial vertical stress in both the numerical and experimental models. Likewise, in the Block Caving scenario with 15 cm of non-flow zone (Figure 23B) — with only one load cell located in the stagnant zone: load cell 3 — this load cell had higher vertical stress at draw compared with its initial vertical stress in the experiment and also in the numerical model. The simulated vertical stress in the stagnant zones of both scenarios were of a smaller magnitude than what was experimentally measured. On the other hand, the vertical stress of the movement zones of the experiments and simulations is similar, decreasing due to draw.
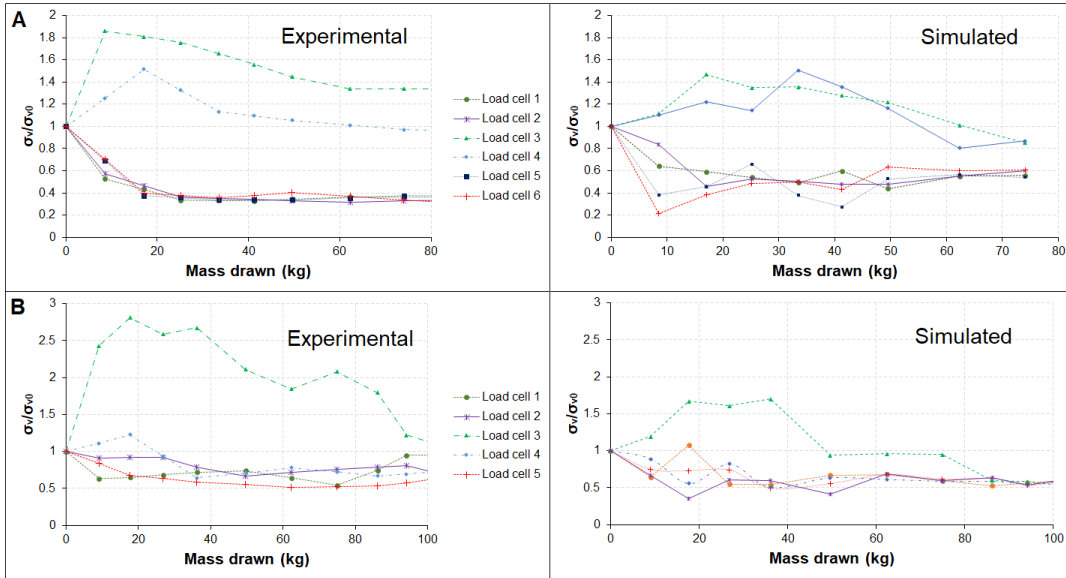
Figure 23 Experimental and numerical simulation of Block Caving draw scenarios. A: 30 cm of spacing and B: 15 cm of spacing.

The mean errors between the experimental and simulated vertical stress are 1.53 kPa, 2.16 kPa and 5.18 kPa, respectively. These errors are assumed to be acceptable by the authors because of the natural stress variability in granular media and the experimental variability (5.58 kPa). The Block Caving draw scenario with a non-flow zone of 15 cm showed the highest error mainly due to the differences in load cell 3. In that scenario, load cell 3 did not simulate high vertical stress probably because the experiment used to calibrate the parameter R did not demonstrate stress concentration in the stagnant zone. However, the stress model can replicate vertical stress concentrations in the stagnant zones and — with even more accuracy — stress relaxation in the movement zones.

6.- Conclusions

In this work, a stress model is presented to simulate vertical stress in granular materials using a CA. The CA used allows gravity flow to be simulated quickly and precisely in large scale models as required by cave mining. Then, the stress in static and dynamic flow conditions can be simulated at large scale when modeled though a gravity flow simulator based on CA. The proposed stress model was calibrated with different experiments at laboratory scale in which a high level of accuracy was observed for different material media and model geometries in static conditions. The parameter E is constant for the same type of material, problem geometry and mesh selected (cell sizes). However, this parameter increased when the height of the model is increased as in cave mining during caving propagation. The stress model also simulated flow conditions through the parameters R and E_{min}. These parameters were calibrated and compared under different flow scenarios, showing good results based on the expected variability of the experimental setup used. Then, our vertical stress model with the flow simulator based on CA has the potential to be applied at block caving scale once the model parameters are defined.

Paper 5: Fine material migration modelled by cellular automata

Castro Raúl, Gómez René, Arancibia Lenin

Abstract

Fine material migration occurs in cave mining during ore extraction and is often associated with ore dilution, which, in the worst case, can cause drawpoint closure. Additionally, the migration of fine material can imply safety issues, such as inrush of fines and, when mixed with water, mudrushes. Nowadays, there are empirical and numerical tools used to study fine material migration; however, in cave mining a large number of rock fragments have to be simulated during flow based on a production plan, and simulations are even more complex when fine rock fragment is involved. Here, a new fine material migration logic based on cellular automata is presented to improve the calculation of this phenomenon according to the literature. The key variable used is the size ratio between the rock fragments of the broken column. The mean size, d_{50}, is used to represent a characteristic rock size and calculate the coarse and fine fragment ratio. The logic presented is calibrated using experimental data from a physical model and is then compared at mine scale. The results show that use of d_{50} to classify the size fragments during gravity flow allows experimental conditions to be replicated. Moreover, if the particle size distribution of coarse material is known, it can be used to adjust a calibration parameter of the migration logic in the flow simulator. We conclude that incorporating the d_{50} to characterize the granular material in gravity flow logic using cellular automata provides an accurate and quick fine material migration estimation.

Key words: caving, cellular automata, dilution, migration, percolation, gravity flow.

1 Introduction

In mining, gravity flow is studied to estimate flow zone interaction for mine design purposes, maximize ore recovery, minimize dilution entry, and avoid risk conditions such as stresses in non-draw zones, air blasts, and mudrushes [32], [60]. Knowledge of gravity flow in cave mining is used to simulate the production plan [54], [76], [318] and to estimate rock fragmentation within the broken column [31], [54], [197], dilution entry [112], and stresses within the broken column [59], [70]. The first studies in granular material flow for mine application were developed through physical modelling [34], [36], [40], [41], [84], [104], back-analysis from mines [45]–[47], [319], and numerical modelling. These numerical modelling approaches mainly used discrete element methods (DEM; [52], [320], [321]) and cellular automata (CA; [7], [9], [10], [49], [322]).

In block caving, during gravity flow, fine material percolation can occur (usually waste material), implying dilution, material segregation and reduced ore recovery [110], [189]. Mine dilution occurs when the waste material mixes with ore thus decreasing ore grade [40], [116]. This phenomenon can result in lost reserves because of early drawpoint closure [112] and can also produce safety problems such as inrush of fines [61] and mudrush events [111], [133].

Dilution due to fine material of low grade is a blending mechanism known as particle percolation [323], [324]. Particle percolation occurs because of shear strain and/or differences in particle size and particle density [113], [284], [324]. Moreover, the particle-size ratio between coarse and fine particles has been found to represent the most important variable in particle percolation [79], [113], [284].

In the broken column, some mines have observed large differences in fragment sizes [45], [252], [319], mainly because of the natural rock fragmentation. This difference in fragment sizes can generate more rock-particle percolation in cases where there is fine material present. In these cases, smaller particles percolate through spaces between larger particles [110]. Initial dilution estimations in block caving are between 10 % and 25 % of the total extraction column [325], even reaching 30 % when the column is exploited over its economic height

[112]. This problem can be estimated through gravity flow simulations, but at caving-mine scale, it is not possible nowadays using DEM. However, there are numerical tools that can simulate a production plan at mine scale, such as Cavesim [9], REBOP[54], Mflow [12], CA3D [326] and Flowsim [10], [76]. These models consider the fragmentation in the geometry of the flow zones, but they do not apply preferential flow of fine material based on fragment size, which is one of the main percolation variables as previously indicated.

In this study, fine material percolation in cave mining was examined with a gravity flow simulator using Cellular Automata (CA). These CA models cannot simulate dynamic interaction between rock fragments; however, once these models are calibrated, they can obtain good results in a short time for large geometries. In this study, our aim is to develop a methodology to simulate percolation mechanics using CA.

2 Gravity flow modelling using cellular automata

Granular material can behave between solid and fluid at the macroscopic level [1], especially during flow. At microscopic level, the particles can be described by stochastic interactions [2] mainly due to their random shapes, sizes, contact points and contact forces [3]. However, this randomness follows a degree of regularity, which has allowed the development of stochastic models to model the flow of granular material [2], [4], [5]. The stochastic theory in gravity flow can be applied using the CA method.

The CA method was introduced by Von Neumann [327] in which a domain is arranged by cells where a transition function defines material movement. In gravity flow, these cells represent the granular material that can be moved using the void diffusion logic. Litwiniszyn [2] applied a cell arrangement to simulate granular material (where cells represent voids and granular material). The first mine application was developed by Jolley [7] to determine drawpoint spacing and a production plan. In that work, void cells moved upwards to change places with cells representing ore and waste material in an effort to simulate gravity flow.

In this work, we used a 3D cubic cell arrangement to represent granular material, while the material flow is generated as void cells moving upwards starting from drawpoints. The void cells are exchanged with upper granular cells. Each upper granular cell has a probability, P_i, of being selected to exchange (see Figure 1) based on its distance as follows [10]:

$$P_i = \frac{d_i^{-n}}{\sum_{k=1}^{9} d_k^{-n}} \tag{1}$$

Where di is the distance between the void cell (k level, Figure 1A) and one of the nine cells i ($k+1$ level, Figure 1B), and n is a function parameter that depends on rock properties such as fragmentation. Studies have shown that for the cell size 2x2x2 (m^3), the parameter n calibrates between 3 and 10 depending on rock properties, and $n = 3$ or $n = 4$ are most frequently used for coarse fragmentation; for smaller rock fragments, n is increased, linked to the width of the flow zone [11], [44], [75], [76], [184]–[186]. Additionally, a minimum number of adjacent voids are required to interchange cells. Therefore, when a cell void is evaluated to move up, the amount of void cells, Cv, around it are calculated (Eq. 2).

$$Cv = \sum_{k=0}^{1} \sum_{j=-1}^{1} \sum_{i=-1}^{1} (c_{ijk}), \qquad \forall c_{ijk} > 0 \tag{2}$$

Where, $c_{ijk} = 1$ if there is a cell void and 0 if not. Then, the void cells flow up if

$$Cv \geq C_v^{threshold} \tag{3}$$

where $C_v^{threshold}$ is the minimum void cells to propagate the flow using Eq. 1. The first mine validations of this logic were developed in 2009 for El Salvador and El Teniente mines [11]. In these simulations, the flow simulator emulated not only the blending of ore and waste, but also the overall ore recovery.
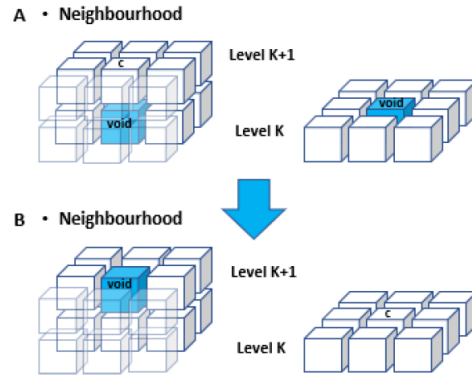
Figure 24 Representation of the descent of a superior block into a void available from a k + 1 level to a k level [11]**.**

The flow simulator emulates an ore deposit through a block model subdivided in cubes of 2x2x2 m³. These cubes represent a volume of broken ore that can flow if they reach the movement zone (MZ) of the draw column. The cells represent a rock fragment distribution characterized using the mean rock size d_{50}.

The interparticle percolation mainly depends on the rock fragment size ratio and particle-size distribution (PSD). Then, a better representation of the percolation process in a broken column would be to use the mean rock size (d_{50}). Rock size differences are common in caving mines due to primary and secondary fragmentation [192] or preconditioning. Moreover, the rock size trace is key information at drawpoints for mine planning. Eq. 4 is the updated version of the flow probability (Eq. 1).

$$P_i = \frac{d_i^{-n} d_{50,i}^{-m}}{\sum_{k=1}^{9} d_k^{-n} d_{50,k}^{-m}} \tag{4}$$

In this equation, d_i is the distance between the void cell and one of the nine cells i ($k+1$ level, Figure 1B) in meters, $d_{50,i}$ is the mean rock size of cell i in meters and n, m are function parameters. The new equation was implemented and evaluated in Synthetic tests.

2.1 Migration logic implementation

Eq. 4 was evaluated in a test model shown in Figure 2A. The model has coarse material at the bottom and fine material on the top. The material density was 2,700 kg/m³, while the model dimension is indicated in Figure 2A and has a drawbell center at the bottom. The cell dimension used is 2x2x2 m³. The function parameter m was tested from 0 to 10 to observe its influence on flow. In Figure 2B the effect of m and d_{50} on probability are presented (Eq. 4) for some combinations. When $m = 0$, the rock size or migration logic is not applied. Depending on the m, n, di values and d_{50} ratio (R_{50}; $d_{50, large fragment}/ d_{50, small fragment}$), there is a maximum m, which is around $m = 3$ in this example. Here, when m = 3 the flow probability of coarse material ($d_{50} = 1$ m) tends to zero while the probability of fine material ($d_{50} = 0.1$ m) depends mainly on the cell location, and even if we keep increasing the m parameter, it does not generate major differences.
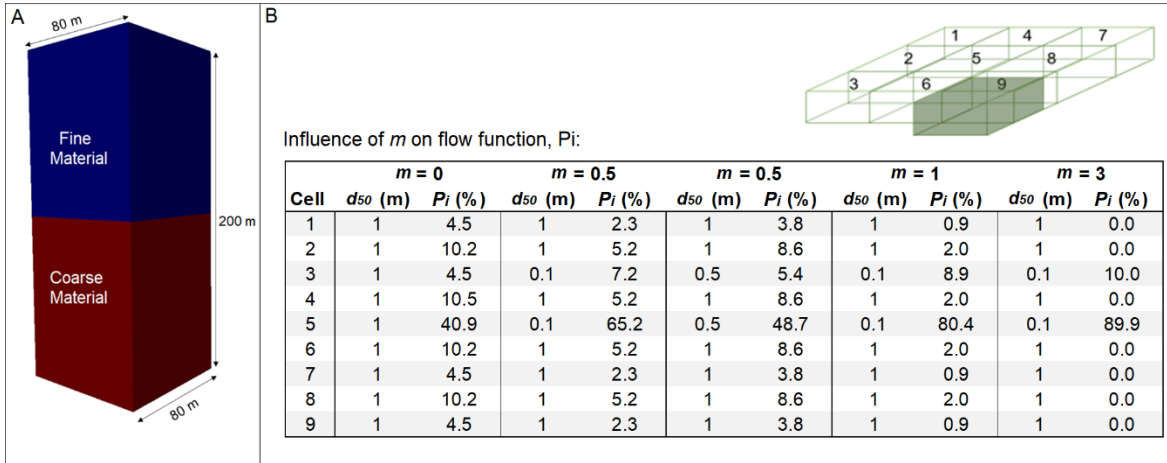
Figure 25 Test model built in simulator to evaluate Eq. 4.

The probability of cell movement with a small d_{50} increases if the m parameter increases. This increase in m implies an increase in fine material migration during flow. Figure 3 shows the effect of the m parameter during flow in the test model built (Figure 2A). Here the total mass drawn included coarse and fine material. In Figure 3, the cell dimension is 2x2x2 m³, and $n = 4$, $d_{50,coarse} = 1.15$ m, and $d_{50,fine} = 0.95$ m.
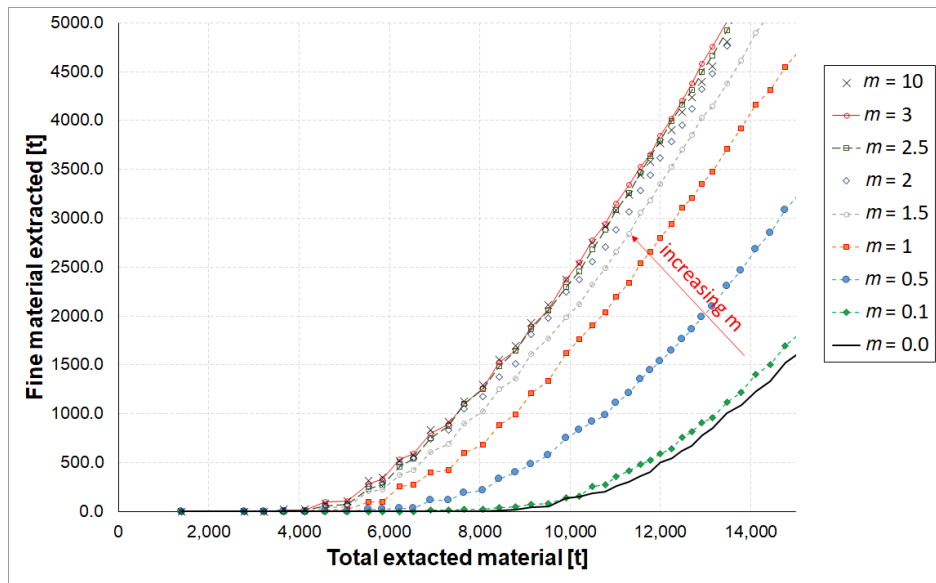
Figure 26 Influence of m on fine material migration during draw.

The m parameter has maximum and minimum values. For $m = 0$, the d_{50} does not change the cell probabilities (Eq. 4), meaning that the migration logic has not been applied. With $m > 0$, the migration logic is activated, and cells with values of less than d_{50} have a higher probability of movement, i.e. the lower the $d_{50,}$ the higher the probability of exchange. It should be noted, however, that the value of d_{50} is not the only variable considered; cell distance is also figured into the equation linked to the width of the flow zone. The higher value of m depends on the rock size ratio, R_{50}, and the location of the lowest d_{50} over the ascendent void cell as noted above. In the example presented in Figure 3, it can be seen that $m > 2$ does not generate major differences in the fine material extracted.

2.2 Synthetic tests

In Stage 1, tests were developed to study key variables during fine material migration under draw through the proposed method. In the test model presented in Figure 2A, a layer of coarse material was placed under a layer

of fine material. Tests included varying the size ratio of materials, $R_{50} = d_{50,coarse}/d_{50,fine}$ and the boundary between the coarse and fine material. The experimental setup of Stage 1 is presented in Table 1. The function parameters of Eq. 4 were kept constant in all tests ($n = 4$ and $m = 1$). The cell dimensions were 2x2x2 m^3, with material density of 2,700 kg/m^3. The d_{50} of coarse material was also kept constant at 1 m, whereas d_{50} of fine material was varied in different test setups to study the effect of varying R_{50}.

Table 1. Experimental setup used in stage 1

Test	# active drawpoints	Coarse material height (m)	Fine material height (m)	$d_{50,fine}$ (m)	Description
1	1	0-200	-	-	Base case, without migration logic ($m = 0$).
2	2	0-200	-	-	
3	1	0-60	60-200	0.1	Migration logic activated to study the effect of the R_{50}, $R_{50} = 10$, $m = 1$.
4	2	0-60	60-200	0.1	
5	1	0-60	60-200	0.2	Migration logic activated to study the effect of the R_{50}, $R_{50} = 5$, $m = 1$.
6	2	0-60	60-200	0.2	
7	1	0-60	60-200	0.5	Migration logic activated to study the effect of the R_{50}, $R_{50} = 2$, $m = 1$.
8	2	0-60	60-200	0.5	
9	1	0-60	60-200	0.8	Migration logic activated to study the effect of the R_{50}, $R_{50} = 1.25$, $m = 1$.
10	2	0-60	60-200	0.8	
11	1	0-40	40-200	0.1	Migration logic activated to study the effect of the boundary height, $R_{50} = 10$, $m = 1$.
12	2	0-40	40-200	0.1	
13	1	0-60	60-200	0.1	Migration logic activated to study the effect of the boundary height, $R_{50} = 10$, $m = 1$.
14	2	0-60	60-200	0.1	
15	1	0-80	80-200	0.1	Migration logic activated to study the effect of the boundary height, $R_{50} = 10$, $m = 1$.
16	2	0-80	80-200	0.1	
17	1	0-100	100-200	0.1	Migration logic activated to study the effect of the boundary height, $R_{50} = 10$, $m = 1$.
18	2	0-100	100-200	0.1	

Tests 1 and 2 are used as base cases in which the migration logic has not been activated. The ore is extracted from one or two drawpoints per setup. Tests from 3 to 10 studied the influence of the R_{50} on the fine material migration during flow while tests from 11 to 18 studied the influence of the fine material location on migration during flow. Each test was simulated 5 times and mean results are reported. A total of 90 simulations were run.

2.2.1 R$_{50}$ Influence on fine material migration

The difference between the d_{50} of rock fragments affects the probability of flow based on the probabilities given by Eq. 4. If R_{50} is high, the small fragments increase their probability of flow compared with large fragments. Here, tests were used to quantify the effect of R$_{50}$. The d_{50} of fine material was varied from 0.1 m to 0.8 m, while the d_{50} of coarse material was kept constant (1 m) along with the boundary (in height) between coarse and fine materials (60 m). As expected, the MZ width is slightly wider for extraction from two drawpoints of the same drawbell, increasing from 34 m to 46 m.

The R_{50} influence on fine material migration can be observed in Figure 4, which shows the results of extraction from one drawpoint (A) and two drawpoints (B). The R_{50} highly influences the fine material migration reported in drawpoints as expected in theory. When R_{50} increased, the fine material also increased the probability of flow. Likewise, when R_{50} decreased, the probability of flow of fine material also decreased with less dilution entry observed at drawpoints.
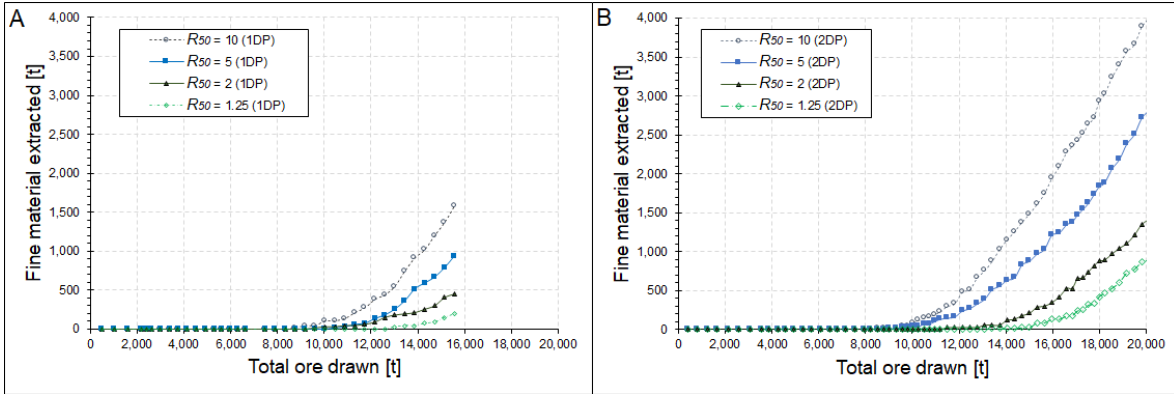
Figure 4: Cumulate fine material extracted from drawpoints (DP) versus total mass (coarse and fine materials) extracted from drawpoints. A: Extraction from one drawpoint. B: Extraction from two drawpoints.

2.2.2 Coarse material height Influence on fine material migration

In this section, tests from 11 to 18 are reported. In these tests, the R_{50} was kept constant while the boundary between coarse and fine material varied from 40 m to 100 m. The migration logic in the flow simulator appears when void cells reach the fine material, based on the void diffusion mechanisms that are used in the simulator. As expected, the height of coarse material influences the amount of fines extracted, with lower heights of coarse material resulting in the extraction of more fine material at the drawpoints.

The effect of height is quantified through the fine material extracted from drawpoints. Figure 5 shows the results of fine material observed in drawpoints at different heights of the coarse material. Results presented in section 2.2.1 and 2.2.2 show the migration logic of the flow simulator agrees with the expected values. However, it is the *m* parameter that is shown to have the greatest influence on the migration logic, and thus it was necessary to calibrate the *m* parameter using the experimental database described in section 3.
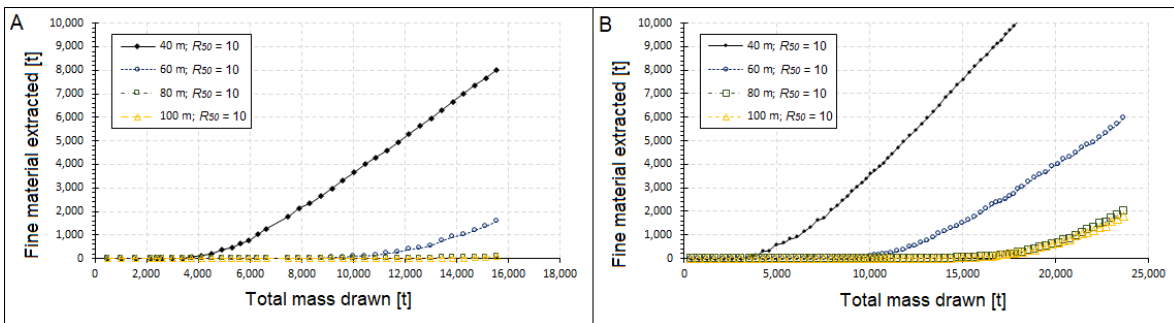
Figure 5 A: Extraction from one drawpoint. B: Extraction from two drawpoints.

3 Calibration using physical experiments

In Stage 2, a physical model used to study fine material migration [79] was emulated in the flow simulator to calibrate the migration logic.

3.1 Physical model

Figure 6 shows the physical model. In this model, eight experimental setups were carried out to quantify the fine material extracted in drawpoints. The model was built in acrylic, with a drawbell at the base and two drawpoints. The geometric scale is 1:50. The dimensions of the physical model are shown in Figure 6-A, and the drawbell dimensions are shown in Figure 6-B. Coarse and fine granular materials were placed in the model to be extracted at the drawpoint. The extraction from drawpoints was conducted using a scaled extraction system to simulate the ore draw of block/panel caving operations. The fine granular material was placed over the coarse granular material as shown in Figure 6-C.
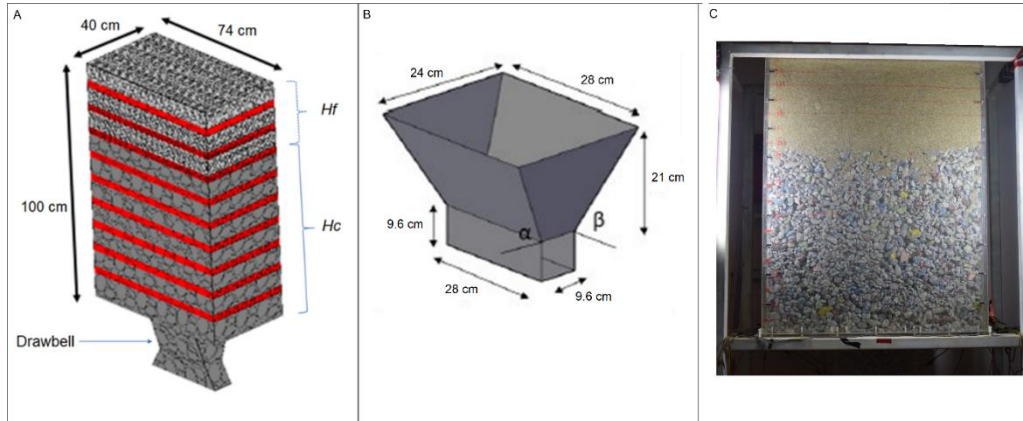
Figure 6 Physical model used in fine material migration for Block Caving [79]**. A: Model dimension (Hf: height of fines material and Hc: Height of coarse material). B: Drawbell dimensions ($\alpha = 71.1^o$; $\beta = 90^o$). C: Experimental test example before material draw.**

The experimental setup was designed to study the effect of R_{50}, the height of fine material, and the PSD of coarse material in fine material migration. Additionally, markers were placed in the granular material (coarse and fine materials) to measure the extraction zones. A total of 788 markers were placed in the gravity flow model. Markers recovered during extraction were used to model the extraction zones after experiments.

The granular material used was ore rock composed mainly of quartz and sericite and obtained from the Chuquicamata Underground Mine. The rock fragment characteristics are summarized in Table 2. The sphericity and roundness were determined based on the methodology of Cho et al. [273]. The point load index was estimated through a point load test [283]. The internal friction angle was determined through a simple shear test in drained samples using a shear box of 10x10 cm^2 [282].

Table 2. Summary of material characterization

Parameter	Value	Unit
Sphericity	0.68	Dimensionless
Roundness	0.20	Dimensionless
Point load index	1.66	MPa
Fine bulk density	1,900	kg/m^3
In-situ density	2,540	kg/m^3
Internal friction angle	37	$^\circ$

3.2 Experimental plan

Table 3 shows the experimental setup design detailed in [79]. The experiments in the physical model were simulated in the flow simulator to calibrate the parameter m of Eq. 4. In the numerical model the following variables were replicated: physical model geometry, d_{50} of coarse material, the d_{50} of fine material, the heights

of coarse and fine materials and the mass extracted per drawpoint. The coefficient of uniformity (*Cu*) was not included in the logic of fine migration, but we hypothesized that Cu should influence *m* because higher Cu implies fewer voids between rock fragments. We tested this in the calibration stage as described below.

Table 3. Experimental setup of fine migration at physical, laboratory scale (mine scale in parenthesis 1:50) from [79]**.**

Exp.	D P	Coarse Height cm	d_{50} coarse mm	Cu coarse	d_{10} coarse mm	d_{50} fine mm	Fine Height cm
1	1	65(32.5m)	23.1(1.15m)	1.5	17	1.8(0.09m)	35(17.5m)
2	2	65	23.1(1.15m)	1.5	17	1.8(0.09m)	35(17.5m)
3	2	65	23.1(1.15m)	1.5	17	1.8(0.09m)	35(17.5m)
4	2	65	23.1(1.15m)	1.5	17	1.8(0.09m)	20(10m)
5	2	50(25.m)	23.1(1.15m)	1.5	17	1.8(0.09m)	50(25m)
6	2	50	23.1(1.15m)	1.5	17	1.8(0.09m)	50(25m)
7	2	65	19(0.95m)	2.6	9	1.8(0.09m)	35(17.5m)
8	2	65	19(0.95m)	3.8	6	1.8(0.09m)	35(17.5m)

The experimental results from the physical model were scaled to mine size, considering the length scale factor, λ_L, of 50. Then, the lengths of the physical model and rock fragments were scaled using Eq. 5.

$$L_i = L_j \lambda_L \tag{5}$$

The mass extracted in the experiments is scaled by volume, considering the length scale factor, i.e. $\lambda_L{}^3$. Here, the density factor is assumed to be the same because the laboratory and mine are under the same gravity force [328]. Then, Figure 7 presents the experimental results [79] to be compared with simulations.
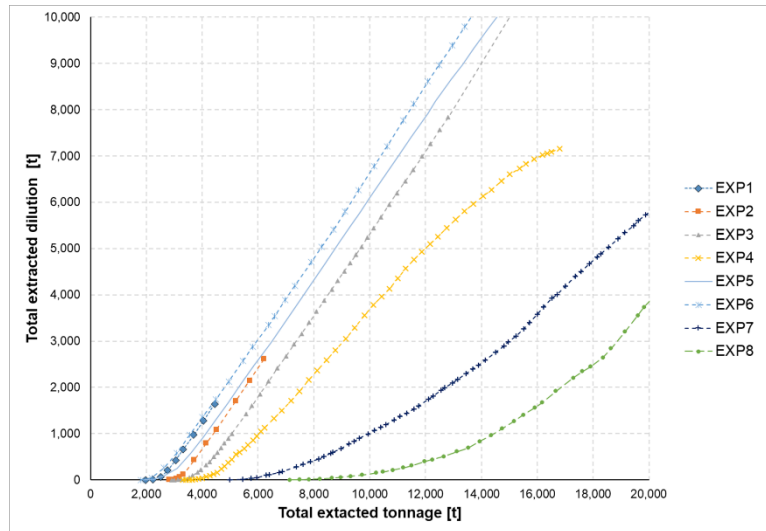
Figure 7 Experimental results of fine migration (scaled from [79]**)**

4 Flow simulator results

The simulations described in Section 3 of the modified migration logic are presented here. Experimental tests of fine material migration during draw [79] were used to calibrate the parameter *m* in Eq. 4. The physical model introduced in Figure 6 was replicated in the flow simulator at mine scale (1:50). The physical experiments are scaled using the length scale factor, λ_L, described in section 3. Figure 8 shows the experimental results from [79] as well as the simulated results. The *m* parameter in the simulation was selected based on the minimum root-mean-square error (*RMSE*) of the physical and numerical experiment of best fit (in Table 4).

$$RMSE = \frac{1}{N} \sum_{i=1}^{N} \left(y_{i,exp} - y_{i,sim} \right)^2 \qquad (4)$$

Here N is the total number of extractions, $y_{i,exp}$ is the dilution in terms of mass reported in the physical experiment (t), and $y_{i,sim}$ is the dilution reported in the flow simulator (t). The numerical model emulated each experimental setup of the physical model (described in section 3). The isolated extraction, Exp 1, shows the greatest differences between the physical and numerical model. The remaining experiments all show good correlation as can be seen in Figure 8.
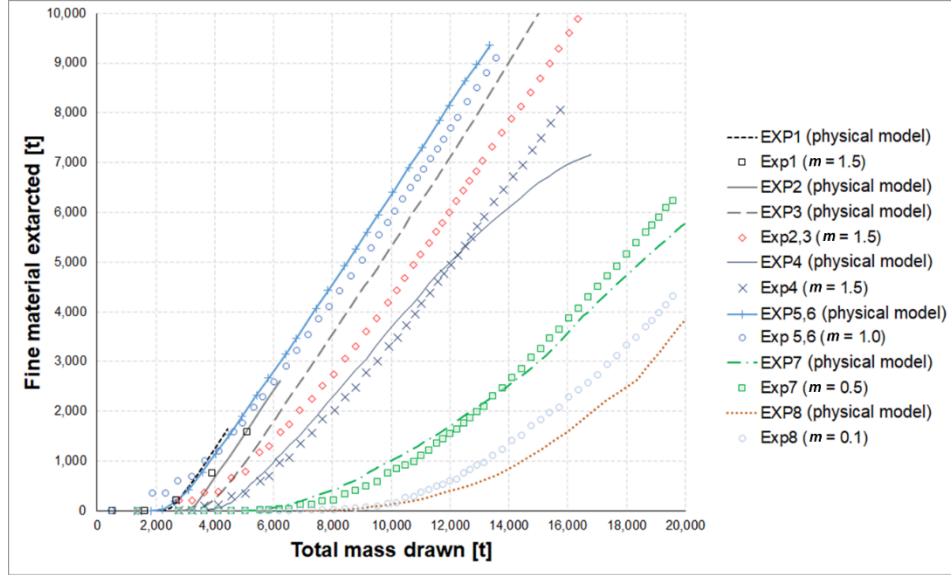
Figure 8 Numerical simulation (markers) calibrated using the physical experiments from [79]**.**

When the input parameters of d_{50} and boundary conditions (i.e., block model geometry, heights of coarse and fine materials, and mass drawn) are considered, the migration logic as introduced in Eq. 4 can replicate the experimental results [79]. Although other variables of interparticle percolation not studied here, such as rock friction, shear strain and rock density, could also have an effect on m, the experimental data presented here show the main granular material property that influences m is the Coefficient of uniformity (Cu).

Table 4. *RMSE* between physical and numerical experiment of best fit

Experiment	*RMSE* [t]	*m*
1	707.2	1.5
2	510.0	1.5
3	875.0	1.5
4	545.0	1.5
5-6	539.3	1.0
7	462.6	0.5
8	39.8	0.1

There is a correlation between the PSD of the coarse material and the adjusted parameter m of Eq. 4. Experiments 3, 7 and 8 have the same experimental setup except for the PSD of coarse material. Then, if we use the Cu to identify each distribution, the following correlation is observed:

$$m \sim \frac{1}{Cu} \tag{5}$$

This correlation is expected because we know that if m decreases, the probability of flow of smaller fragments also decreases. On the other hand, if the Cu increases, indicating a wide PSD, the particle percolation decreases because the granular material is well packaged. However, more experimental data are needed to define a formula to identify the relationship between these parameters.

5 Evaluation of migration logic using mine data

As described above, the m parameter was calibrated previous to using the migration logic. The calibration stage included the experimental procedure presented in this work, using controlled experiments with the granular material to be simulated. As observed in this study, the m parameter depends on material properties, such as the PSD of coarse material, PSD of fine material, friction, cohesion, humidity, elastic moduli, shape factor, densities, stresses. Furthermore, we found that the m parameter is inversely proportional to the Cu for the material used.

Once the m function parameter was calibrated, we evaluated the migration logic of the flow simulator with mine data. The Inca Central Este sector from El Salvador mine in Chile was used for the mine-scale evaluation. The block model dimensions were 290 m x 410 m x 800 m (width, length, and height), in which 107 drawpoints were located.

Ore extraction data were available from 2003 to 2007 including dilution (fine material) reported in drawpoints. The dilution was identified through the geological tracer, shale rock. The ore rock has $d_{50,ore} = 0.7$ m, $d_{10} = 0.35$ m and $Cu = 3.1$ [329]. The shale mean size, $d_{50,shale}$, is approximately 0.1 m. The function parameters n and m are 3.4 and 0.4 respectively. The n parameter was determined by Valencia [75], while the m parameter was interpolated based on the results in Section 4. Figure 9 shows the simulated results along with the mine data of dilution reported in drawpoints.
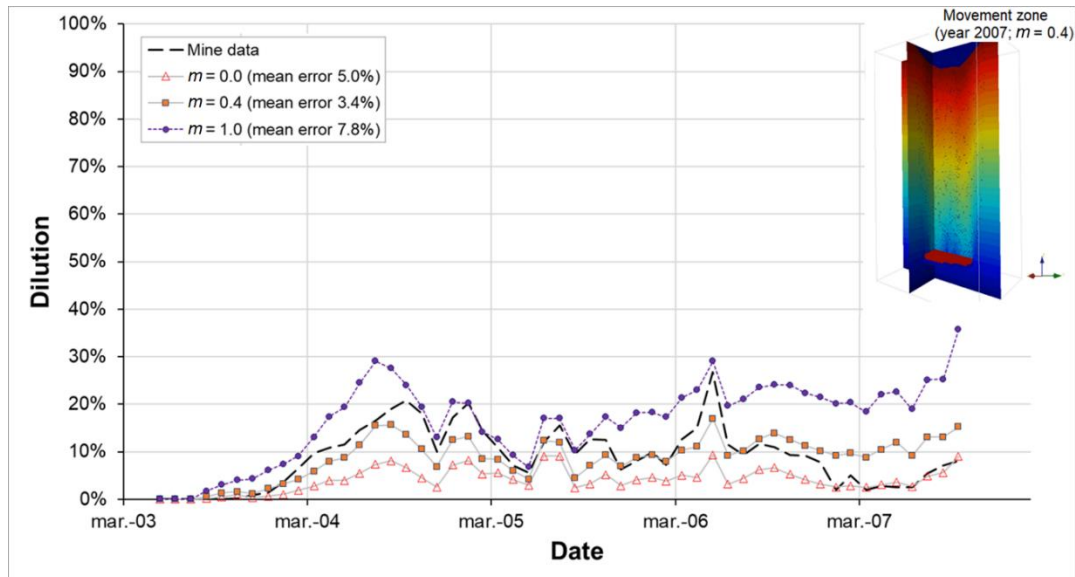
Figure 9 Simulated dilution reported in drawpoints compared with mine data. MZ at the end of simulation is added.

The migration logic implemented in the Flow simulator has good correlation with the mine data used. Additionally, in Figure 9 simulations are presented without the migration logic ($m = 0$) and with a high probability of fine material flow ($m = 1$) to observe the effect of m at mine scale. The minimum error between the simulation and mine dilution was obtained by the m value defined by the calibration stage, $m = 0.4$. These results imply that the m parameter calibrated through the physical experiment of fine migration is representative of the percolation process during flow in block caving. At mine scale, a scaling effect could appear when m is calibrated from laboratory experiments. However, in our mine simulation this effect was not observed.

6 Conclusions

In this paper, a fine migration logic implemented in a granular flow simulator model based on cellular automata was tested including rock size using d_{50} as a key parameter. The rock size used for estimating fine material migration in mining was chosen given its theorical justification based on a literature review. The results show that including rock size in the migration logic reflects the fine material migration reported with physical experiments. In those experiments, the PSD of coarse material was shown to highly influence fine material migration. Likewise, in the numerical model, this can also be represented by calibrating the function parameter related to the rock size. We also found that the migration logic implemented in the Flow simulator had good correlation when actual mine data was used. We conclude that, based on experimental results of fine material migration, the use of the d_{50} as a rock characteristic size in the flow probability function (Eq. 4) gives a good estimation and representativeness of the fine material migration phenomenon in mining.

6 General conclusions

This study presents different physical experiments and simulations using numerical modeling through cellular automata in order to contribute to the current knowledge of gravity flow in block cave mining. The main goal was integrating rock size fragmentation during draw in gravity flow through a migration model. Additionally, stresses in broken columns were studied and modeled due to their influence on gravity flow, and particularly, on rock fragmentation.

In the fragmentations studies (paper 1 and 2), it was experimentally possible to identify the importance of rock strength, travel distance (or residence time) and overload (through the vertical stress, σ_V) in rock fragmentation during draw. Then, a secondary fragmentation model is included in the gravity flow simulator through the reduction ratio, $R_{50} = \frac{d_{50,inicial}-d_{50,final}}{d}$. This ratio modified the mean fragment size (d_{50}) of a cell that travels a distance d. The reduction ratio is determined based on the UCS and the vertical stress, σ_V, as $R_{50} = \alpha \left(\frac{\sigma_v}{UCS}\right)^{\beta}$, where α and β are constants. In this reduction model, the UCS is a cell property while the σ_V is determined through the vertical stress model proposed in paper 4 (previously calibrated with paper 3 and other studies).

Finally, paper 5 incorporates the d_{50} in the flow probability as a key variable in gravity flow simulations when different rock fragment sizes are present. Thus, the fragmentation and stress models are integrated in the flow simulation through the d_{50}. Then, the flow simulator based on cellular automata can included key variables during gravity flow in block caving through fast and accurate simulations.

7 Bibliography

[1]   B. Andreotti, Y. Forterre, and O. Pouliquen, *Granular Media; Between Fluid and Solid*, vol. 55, no. 2. Cambridge University Press, 2013. doi: 10.1080/00107514.2014.885579.

[2]   J. Litwiniszyn, *Stochastic Methods in Mechanics of Granular Bodies*. Springer-Verlag, 1974.

[3]   V. A. Osinov, "A model of a discrete stochastic medium for the problems of loose material flow," *Contin. Mech. Thermodyn.*, vol. 6, no. 1, pp. 51–60, 1994, doi: 10.1007/BF00711125.

[4]   W. W. Mullins, "Stochastic theory of particle flow under gravity," *J. Appl. Phys.*, vol. 43, no. 2, pp. 665–678, 1972, doi: 10.1063/1.1661175.

[5]   G. Chen, "Stochastic modeling of rock fragment flow under gravity," *Int. J. rock Mech. Min. Sci. Geomech. Abstr.*, vol. 34, no. 2, pp. 323–331, 1997, doi: 10.1016/S0148-9062(96)00051-4.

[6]   K. Kamrin and M. Z. Bazant, "Stochastic flow rule for granular materials," *Phys. Rev. E - Stat. Nonlinear, Soft Matter Phys.*, vol. 75, no. 4, pp. 1–28, 2007, doi: 10.1103/PhysRevE.75.041301.

[7]   D. Jolley, "Computer Simulation of the Movement of Ore and Waste in an Underground Mining Pillar," *Can. Min. Metall. Bull.*, vol. 61, no. 675, pp. 854–859, 1968.

[8]   C. Calderon, M. Alfaro, and J. Saavedra, "Computational model for simulation and Visualization of gravitational flow," in *Massmin 2004*, 2004, pp. 185–188.

[9]   G. Sharrock, D. A. Beck, G. Booth, and K. Sandy, "Simulating gravity flow in sub-level caving with cellular automata," in *Massmin 2004*, 2004, pp. 189–194.

[10]   R. Castro and W. Whiten, "A new cellular automaton to model gravity flow in block caving based on physical modelling observation," *Julius Kruttschnitt Mineral Research Centre*, pp. 233–241, 2007.

[11]   R. L. Castro, F. Gonzalez, and E. Arancibia, "Development of a gravity flow numerical model for the evaluation of drawpoint spacing for block/panel caving," *J. South. African Inst. Min. Metall.*, vol. 109, no. 7, pp. 393–400, 2009.

[12]   W. H. Gibson, "Stochastic models for gravity flow: numerical considerations," in *3rd International symposium on block and sublevel caving*, 2014, pp. 337–347.

[13]   Y. Hebert and G. Sharrock, "Three-dimensional simulation of cave initiation, propagation and surface subsidence using a coupled finite difference–cellular automata solution," in *Fourth International Symposium on Block and Sublevel Caving, Caving 2018*, 2018, pp. 151–166.

[14]   U. C. Kothari, F. M. Sinaga, and J. N. Tshisens, "Understanding surface subsidence from a block cave by comparing InSAR data with 3D numerical modeling," in *Eighth International Conference & Exhibition on Mass Mining, Massmin 2020*, 2020, pp. 318–326.

[15]   S. Webster, E. Sasomir, and A. Wyllie, "Learnings from mining cave extensions at Northparkes Mines and new technology to improve the value of future cave designs," in *Eighth International Conference & Exhibition on Mass Mining, Massmin 2020*, 2020, pp. 92–102.

[16]   R. Castro, R. Gómez, and L. Arancibia, "Fine material migration modelled by cellular automata," *Granul. Matter*, vol. 24, no. 1, pp. 1–11, Feb. 2022, doi: 10.1007/s10035-021-01173-8.

[17]   D. Laubscher, "Draw strategy," in *Block cave manual*, Brisbane: International Caving Study (1997-2000), 2000.

[18]   G. Power, "Full scale SLC draw trials at Ridgeway Gold Mine," in *Massmin 2004*, 2004, pp. 225–230.

[19]   G. Dunstan, "The thruth is stranger than fiction – the story of ridgeway gold mine," in *Seventh International Conference & Exhibition on Mass Mining, Massmin 2016*, 2016, pp. 19–30.

[20]   G. Power and A. Campbell, "Modelling of real-time marker data to improveoperational recovery in sublevel caving mines," in *Seventh International Conference & Exhibition on Mass Mining, Massmin 2016*, 2016, pp. 105–110.

[21]   I. Brunton, G. Lett, and G. Sharrock, "Full-scale Flow markers experiments at ridgeway Deeps and cadia east cave operations," in *Seventh International Conference & Exhibition on Mass Mining, Massmin 2016*, 2016, pp. 817–824.

[22]   R. Hocking, M. Fargher, and C. Chester, "Marker design and calibration for Carrapateena sub level and block cave with a focus on fines migration and far field Flow," in *Eighth International Conference & Exhibition on Mass Mining, Massmin 2020*, 2020, pp. 489–504.

[23]   D. Garces, E. Viera, R. Castro, and M. Meléndez, "Gravity flow full-scale tests at Esmeralda mine's Block-2, El Teniente," in *Seventh International Conference & Exhibition on Mass Mining, Massmin 2016*, 2016, pp. 349–358.

[24]   B. Hollins and J. Tucker, "Draw point analysis using a marker trial at the Perseverance Nickel Mine, Leinster, Western Australia," in *Massmin 2004*, 2004, pp. 498–502.

[25]   U. Frisch, B. Hasslacher, and Y. Pomeau, "Lattice-gas automata for the Navier-Stokes equation," *Phys. Rev. Lett.*, vol. 56, no. 14, pp. 1505–1508, 1986, doi: 10.1103/PhysRevLett.56.1505.

[26]   S. G. Psakhie *et al.*, "Movable cellular automata method for simulating materials with mesostructure," *Theor. Appl. Fract. Mech.*, vol. 37, no. 1–3, pp. 311–334, 2001, doi: 10.1016/S0167-8442(01)00079-9.

[27]   D. Désérable, P. Dupont, M. Hellou, and S. Kamali-Bernard, "Cellular Automata in Complex Matter," *Complex Syst.*, vol. 20, no. 1, pp. 67–91, 2011, doi: 10.25088/complexsystems.20.1.67.

[28]   G. E. Tucker, S. W. McCoy, and D. E. J. Hobley, "A lattice grain model of hillslope evolution," *Earth Surf. Dyn.*, vol. 6, no. 3, pp. 563–582, 2018, doi: 10.5194/esurf-6-563-2018.

[29]   V. K. Jasti and C. F. Higgs, "A fast first order model of a rough annular shear cell using cellular automata," *Granul. Matter*, vol. 12, no. 1, pp. 97–106, 2010, doi: 10.1007/s10035-009-0159-x.

[30]   J. Tejchman, *Confined granular flow in silos*. Springer Series in Geomechanics & Geoengineering, 2013.

[31]   R. Gómez, R. L. Castro, A. Casali, S. Palma, and A. Hekmat, "A Comminution Model for Secondary Fragmentation Assessment for Block Caving," *Rock Mech. Rock Eng.*, vol. 50, no. 11, pp. 3073–3084, 2017, doi: 10.1007/s00603-017-1267-2.

[32]   A. Susaeta, "Theory of gravity flow (Part 1)," in *Massmin 2004*, 2004, pp. 167–172.

[33]   R. Castro, "Study of the Mechanisms of Gravity Flow for Block Caving," University of Queensland, 2007.

[34]   R. L. Castro, M. A. Fuenzalida, and F. Lund, "Experimental study of gravity flow under confined conditions," *Int. J. Rock Mech. Min. Sci.*, vol. 67, pp. 164–169, 2014, doi: 10.1016/j.ijrmms.2014.01.013.

[35]   A. W. Jenike, J. R. Johanson, and J. W. Carson, "Bin Loads—Part 4: Funnel-Flow Bins," *J. Eng. Ind.*, vol. 2, pp. 13–16, 1973.

[36]   R. Kvapil, "Gravity flow of granular materials in hoppers and bins - Part I," *Int. J. Rock Mech. Min. Sci.*, vol. 2, no. 1, pp. 35–41, 1965, doi: 10.1016/0148-9062(65)90020-3.

[37]   R. Kvapil, "Gravity flow of granular materials in Hoppers and bins in mines-II. Coarse material," *Int. J. Rock Mech. Min. Sci.*, vol. 2, no. 3, pp. 277–292, 1965, doi: 10.1016/0148-9062(65)90029-X.

[38]   D. Laubscher, *Block cave manual*. Brisbane: Julius Kruttschnitt Mineral Research Centre, 2000.

[39]   M. Sperl, "Experiments on corn pressure in silo cells - Translation and comment of Janssen's paper from 1895," *Granul. Matter*, vol. 8, no. 2, pp. 59–65, 2006, doi:

10.1007/s10035-005-0224-z.

[40]   D. H. Laubscher, "Cave mining-the state of the art," *J. South. African Inst. Min. Metall.*, vol. 94, no. 10, pp. 279–293, 1994.

[41]   R. Kvapil, *Gravity Flow in Sublevel and Panel caving.* Lulea University of Technology Press, 2008.

[42]   A. W. Jenike, J. R. Johanson, and J. W. Carson, "Bin Loads—Part 3: Mass-Flow Bins," *J. Eng. Ind.*, vol. 95, no. 1, pp. 6–12, 1973.

[43]   P. Gustafsson, "Waste Rock Content Variations During Gravity Flow in Sublevel Caving," Lulea University of Technology, 1998.

[44]   D. Garcés, "Estudio de flujo gravitacional de material hundido por medio de trazadores inteligentes," Universidad de Chile, 2015.

[45]   J. Hurtado, J. Pereira, and R. Campos, "Informe Final Backanalysis De Fragmentación, Minas: Diablo Regimiento, Reno Y Teniente 4 Sur Tonalita. Nnm-Ico-Geo-Inf N⁰ 003.," Rancagua, 2007.

[46]   N. Montecino, "Modelo De Mezcla De Fragmentación Secundaria En Minería De Block/Panel Caving," Universidad de Chile, 2011.

[47]   S. Steffen and P. Kuiper, "Case Study: Improving SLC recovery by measuring ore flow with electronic markers," in *3rd International symposium on block and sublevel caving*, 2014, pp. 328–336.

[48]   E. Viera and E. Diez, "Analysis of hang-up frequency in Bloque 1–2, Esmeralda Sur Mine," in *Proceedings of the 3rd international symposium on block and sublevel caving, Caving 2014*, 2014, pp. 138–145.

[49]   G. W. Baxter, "Cellular automata models of granular flow," *Exp. Comput. Tech. Soft Condens. Matter Phys.*, vol. 9780521115, no. 2, pp. 209–229, 2012, doi: 10.1017/CBO9780511760549.008.

[50]   P. Cid, "Simulacion de flujo gravitacional en batea de extraccion a traves de elementos discretos," Universidad de Concepcion, 2019.

[51]   P. W. Cleary and M. L. Sawley, "DEM modelling of industrial granular flows: 3D case studies and the effect of particle shape on hopper discharge," *Appl. Math. Model.*, vol. 26, no. 2, pp. 89–111, 2002, doi: 10.1016/S0307-904X(01)00050-6.

[52]   W. Hancock, "Gravity flow of rock in caving mines : Numerical modelling of isolated, interactive and non-ideal draw," University of Queensland, 2013.

[53]   P. A. Langston, U. Tüzün, and D. M. Heyes, "Discrete element simulation of internal stress and flow fields in funnel flow hoppers," *Powder Technol.*, vol. 85, no. 2, pp. 153–169, 1995, doi: 10.1016/0032-5910(95)03009-X.

[54]   M. E. Pierce, "A model for gravity flow of fragmented rock in block caving mines," University of Queensland, 2009.

[55]   M. E. Pierce, P. A. Cundall, G. Van Hout, and L. Lorig, "PFC 3D modeling of caved rock under draw," in *Numerical Modeling in Micromechanics via Particle Methods*, 2017, pp. 211–217.

[56]   D. Laubscher, "Drawpoint spacing," in *Block cave manual*, Brisbane: International Caving Study (1997-2000), 2000.

[57]   H. Sahupala, C. Brannon, S. Annavarapu, and K. Osborne, "Recovery of extraction pillars in the deep ore zone (DOZ) block cave, PT freeport Indonesia," in *5Th Conference and Exhibition on Mass Mining*, 2008, pp. 191–202.

[58]   M. Orellana, C. Cifuentes, and J. Díaz, "Caving experiences in Esmeralda sector, El Teniente mine," in *3rd International symposium on block and sublevel caving*, 2014, pp. 78–90.

[59]   M. E. Pierce, "Forecasting vulnerability of deep extraction level excavations to draw-induced cave loads," *J. Rock Mech. Geotech. Eng.*, vol. 11, no. 3, pp. 527–534, 2019, doi: 10.1016/j.jrmge.2018.07.006.

[60]   D. H. Laubscher, "Mud flow / Mud push and water inflow potential," in *Block cave manual*, International Caving Study (1997-2000), 2000, pp. 1–9.

[61]   D. Pretorius and S. Ngidi, "Cave management ensuring optimal life of mine at Palabora," in *5Th Conference and Exhibition on Mass Mining*, 2008, pp. 63–71.

[62]   G. P. Deutsch and L. C. Schmidt, "Pressures on Silo Walls," *Trans. ASME*, pp. 450–457, 1969, doi: 10.1016/B978-0-444-42470-9.50016-7.

[63]   D. M. Walker and M. H. Blanchard, "Pressures in experimental coal hoppers," *Chem. Eng. Sci.*, vol. 22, no. 12, pp. 1713–1745, 1967, doi: 10.1016/0009-2509(67)80206-9.

[64]   R. M. Nedderman, "The use of the kinematic model to predict the development of the stagnant zone boundary in the batch discharge of a bunker," *Chem. Eng. Sci.*, vol. 50, no. 6, pp. 959–965, 1995, doi: 10.1016/0009-2509(94)00464-3.

[65]   F. Melo, F. Vivanco, C. Fuentes, and V. Apablaza, "Kinematic model for quasi static granular displacements in block caving: Dilatancy effects on drawbody shapes," *Int. J. Rock Mech. Min. Sci.*, vol. 45, no. 2, pp. 248–259, 2008, doi: 10.1016/j.ijrmms.2007.07.005.

[66]   R. M. Nedderman and U. Tüzün, "A kinematic model for the flow of granular materials," *Powder Technol.*, vol. 22, no. 2, pp. 243–253, 1979, doi: 10.1016/0032-5910(79)80030-3.

[67]   F. Melo, F. Vivanco, C. Fuentes, and V. Apablaza, "On drawbody shapes: From Bergmark-Roos to kinematic models," *Int. J. Rock Mech. Min. Sci.*, vol. 44, no. 1, pp. 77–86, 2007, doi: 10.1016/j.ijrmms.2006.04.010.

[68]   W. W. Mullins, "Critique and comparison of two stochastic theories of gravity-induced particle flow," *Powder Technol.*, vol. 23, no. 1, pp. 115–119, 1979, doi: 10.1016/0032-5910(79)85030-5.

[69]   L. J. Lorig, "Relation between Caved Column Height and Vertical Stress at the Cave Base," 2000.

[70]   R. Castro, R. Gómez, M. Pierce, and J. Canales, "Experimental quantification of vertical stresses during gravity flow in block caving," *Int. J. Rock Mech. Min. Sci.*, vol. 127, no. January, 2020, doi: 10.1016/j.ijrmms.2020.104237.

[71]   H. Sahupala, T. Szwedzicki, and R. Prasetyo, "Diameter of a draw zone—a case study from a block caving mine, Deep Ore Zone, PT Freeport Indonesia," in *Second International Symposium on Block and Sublevel Caving*, 2010, pp. 633–645.

[72]   C. Zuñiga, "Estudio del efecto de la distribución granulométrica en el flujo gravitacional," Universidad de Chile, 2007.

[73]   R. Castro, R. Trueman, and A. Halim, "A study of isolated draw zones in block caving mines by means of a large 3D physical model," *Int. J. Rock Mech. Min. Sci.*, vol. 44, no. 6, pp. 860–870, 2007, doi: 10.1016/j.ijrmms.2007.01.001.

[74]   B. Reyes, "Caracterización de elipsoides de extracción con material cohesivo en block/panel caving utilizando rocky DEM," Universidad Técnica Federico Santa Maria, 2021.

[75]   M. E. Valencia, "Desarrollo e implementación de FlowSim para su aplicación en minería de Block/Panel Caving," Universidad de Chile, 2014.

[76]   R. Castro, L. Arancibia, D. Guzman, and J. P. Henriquez, "Experiments and simulation of gravity flow in block caving through FlowSim," in *Fourth International Symposium on Block and Sublevel Caving, Caving 2018*, 2018, pp. 313–322.

[77]   F. Armijo, S. Irribarra, and R. Castro, "Experimental study of fines migration for caving mines," in *Proceedings of the 3rd international symposium on block and sublevel caving, Caving 2014*, 2014, pp. 356–362.

[78]   V. Sánchez, R. L. Castro, and S. Palma, "Gravity flow characterization of fine granular material for Block Caving," *Int. J. Rock Mech. Min. Sci.*, vol. 114, no. November 2018, pp. 24–32, 2019, doi: 10.1016/j.ijrmms.2018.12.011.

[79]   R. Castro, L. Arancibia, and R. Gómez, "Quantifying fines migration in block caving through 3D experiments," *Int. J. Rock Mech. Min. Sci.*, vol. 151, no. December 2021, pp. 8–10, Mar. 2022, doi: 10.1016/j.ijrmms.2022.105033.

[80]   A. Jin, H. Sun, G. Ma, Y. Gao, S. Wu, and X. Meng, "A study on the draw laws of caved ore and rock using the discrete element method," *Comput. Geotech.*, vol. 80, pp. 59–70, 2016, doi: 10.1016/j.compgeo.2016.06.016.

[81]   R. Le-Feaux, R. Castro, D. Cortez, R. Gómez, and D. Silva, "A hybrid extraction level layout design for block caving," *Min. Technol.*, vol. 131, no. 1, pp. 51–65, 2021, doi: 10.1080/25726668.2021.1992980.

[82]   K. Yu, F. Ren, G. Chitombo, R. Puscasu, and L. Kang, "Optimum Sublevel Height and Drift Spacing in Sublevel Cave Mining Based on Random Medium Theory," *Mining, Metall. Explor.*, vol. 37, no. 2, pp. 681–690, 2020, doi: 10.1007/s42461-020-00185-x.

[83]   J. Hadjigeorgiou and J. F. Lessard, "Numerical investigations of ore pass hang-up phenomena," *Int. J. Rock Mech. Min. Sci.*, vol. 44, no. 6, pp. 820–834, 2007, doi: 10.1016/j.ijrmms.2006.12.006.

[84]   R. Castro, R. Gómez, and A. Hekmat, "Experimental quantification of hang-up for block caving applications," *Int. J. Rock Mech. Min. Sci.*, vol. 85, pp. 1–9, 2016, doi: 10.1016/j.ijrmms.2016.02.005.

[85]   A. Susaeta, "Theory of gravity flow (Part 2)," in *Massmin 2004*, 2004, pp. 173–178.

[86]   R. Verdugo and J. Ubilla, "Geotechnical analysis of gravity flow during block caving," in *Massmin 2004*, 2004, pp. 195–200.

[87]   H. M. Beakawi Al-Hashemi and O. S. Baghabra Al-Amoudi, "A review on the angle of repose of granular materials," *Powder Technol.*, vol. 330, no. October, pp. 397–417, 2018, doi: 10.1016/j.powtec.2018.02.003.

[88]   L. Dorador, "Experimetnal Investigation of the effect of Broken ore Properties on Secondary Fragmentation During Block Caving," University of British Columbia, 2016.

[89]   D. Olivares, R. Castro, and A. Hekmat, "Influence of Fine Material, Humidity and Vertical Loads on the Flowability of Caved Rock," 2015.

[90]   C. Antilao, "Modelación física del fenómeno de migración de finos en minería de caving," Universidad de Concepción, 2021.

[91]   E. Cokca, O. Erol, and F. Armangil, "Effects of compaction moisture content on the shear strength of an unsaturated clay," *Geotech. Geol. Eng.*, vol. 22, no. 2, pp. 285–297, 2004, doi: 10.1023/B:GEGE.0000018349.40866.3e.

[92]   K. Bláhová, L. Ševelová, and P. Pilařová, "Influence of water content on the shear strength parameters of clayey soil in relation to stability analysis of a hillside in brno region," *Acta Univ. Agric. Silvic. Mendelianae Brun.*, vol. 61, no. 6, pp. 1583–1588, 2013, doi: 10.11118/actaun201361061583.

[93]   P. Müller and J. Tomas, "Investigation on the compression behavior of tetrahedral agglomerates," *Granul. Matter*, vol. 15, no. 6, pp. 863–872, 2013, doi: 10.1007/s10035-013-0419-7.

[94]   C. Camp and W. Gill, "The Effect of Drying on Soil Strength Parameters," *Soil Sci. Soc. Am. J.*, vol. 33, no. 5, pp. 641–644, 1969, doi: 10.2136/sssaj1940.036159950004000c0132x.

[95]   A. M. Mouazen, H. Ramon, and J. De Baerdemaeker, "Effects of bulk density and moisture content on selected mechanical properties of sandy loam soil," *Biosyst. Eng.*, vol. 83, no. 2, pp. 217–224, 2002, doi: 10.1006/bioe.2002.0103.

[96]   P. D. Ayers, "Moisture and Density Effects on Soil Shear Strength Parameters for Coarse Grained Soils," *Trans. Am. Soc. Agric. Eng.*, vol. 30, no. 5, pp. 1282–1287, 1987, doi: 10.13031/2013.30559.

[97]   D. Laubscher, "Draw control," in *Block cave manual*, Brisbane: International Caving Study (1997-2000), 2000.

[98]   I. Janelid and R. Kvapil, "Sublevel caving," *Int. J. Rock Mech. Min. Sci.*, vol. 3, no. 2, pp. 129–132, 1966, doi: 10.1016/0148-9062(66)90004-0.

[99]   I. D. Brunton, S. J. Fraser, J. H. Hodgkinson, and P. C. Stewart, "Parameters influencing full scale sublevel caving material recovery at the Ridgeway gold mine," *Int. J. Rock Mech. Min.*

Sci., vol. 47, no. 4, pp. 647–656, 2010, doi: 10.1016/j.ijrmms.2009.12.011.

[100] I. Brunton, G. Sharrock, and G. Lett, "Full Scale Near Field Flow Behaviour at the Ridgeway Deeps Block Cave Mine," 2012.

[101] T. G. Heslop, "Understanding the flow of caved ore and its influence on ore recoveries and dilution in a block cave," in *Second International Symposium on Block and Sublevel Caving*, 2010, pp. 539–552.

[102] V. Encina, C. Fuentes, and M. Palma, "Study of interaction between ellipses of extraction in a physical model of granular material in 2-D," in *Massmin 2004*, 2004, pp. 220–224.

[103] A. Susaeta, E. Rubio, J. Henriquez, and G. Pais, "Dilution behaviour at Codelco panel cave mines," in *5Th Conference and Exhibition on Mass Mining*, 2008, pp. 167–178.

[104] R. Trueman, R. Castro, and A. Halim, "Study of multiple draw-zone interaction in block caving mines by means of a large 3D physical model," *Int. J. Rock Mech. Min. Sci.*, vol. 45, no. 7, pp. 1044–1051, 2008, doi: 10.1016/j.ijrmms.2007.11.002.

[105] A. Van As and H. Van Hout, "Implications of widely spaced drawpoints," in *5Th Conference and Exhibition on Mass Mining*, 2008, pp. 147–154.

[106] R. L. Castro, R. Vargas, and F. De La Huerta, "Determination of drawpoint spacing in panel caving: A case study at the el teniente mine," *J. South. African Inst. Min. Metall.*, vol. 112, no. 10, pp. 871–876, 2012.

[107] D. H. Laubscher, "Angle of draw," in *Block cave manual*, International Caving Study (1997-2000), 2000.

[108] J. Bridgwater, R. Utsumi, Z. Zhang, and T. Tuladhar, "Particle attrition due to shearing-the effects of stress, strain and particle shape," *Chem. Eng. Sci.*, vol. 58, no. 20, pp. 4649–4665, 2003, doi: 10.1016/j.ces.2003.07.007.

[109] M. Hashim and G. Sharrock, "Dimensionless percolation rate of particles in block caving mines," 2012.

[110] M. H. M. Hashim, G. Sharrock, and S. Saydam, "A Review of Particle Percolation in Mining," in *SHIRMS 2008*, 2008, pp. 273–284. doi: 10.36487/acg_repo/808_72.

[111] R. Butcher, T. R. Stacey, and W. C. Joughin, "Mud rushes and methods of combating them," *J. South African Inst. Min. Metall.*, vol. 105, no. 11, pp. 817–824, 2005.

[112] D. Laubscher, "Dilution," in *Block cave manual*, Brisbane: International Caving Study (1997-2000), 2000.

[113] M. H. Cooke, J. Bridgwater, and A. M. Scott, "Interparticle percolation: lateral and axial diffusion coefficients," *Powder Technol.*, vol. 21, no. 2, pp. 183–193, 1978, doi: 10.1016/0032-5910(78)80088-6.

[114] M. Hashim, "Particle Percolation in block Caving mines," The University of New South Wales, 2011.

[115] R. Castro and M. Pineda, "The role of gravity flow in the design and planning of large sublevel stopes," *J. South. African Inst. Min. Metall.*, vol. 115, no. 2, pp. 113–118, 2015, doi: 10.17159/2411-9717/2015/v115n2a4.

[116] R. L. Castro and P. S. Paredes, "Empirical observations of dilution in panel caving," *J. South. African Inst. Min. Metall.*, vol. 114, no. 6, pp. 455–462, 2014.

[117] P. Vergara, "Estudio experimental de flujo gravitacional en minería de Panel Caving," Universidad de Chile, 2016.

[118] J. Sougarret, L. Quiñones, R. Morales, and R. Apablaza, "New Vision in Caving Mining in Andina Division, Codelco Chile," in *Massmin 2004*, 2004, pp. 542–546.

[119] Codelco, *Preacondicionamiento del Macizo Rocoso - Desarrollo Tecnológico 1999-2010*. 2010.

[120] D. Villa and T. Diering, "A new mine planning tool for sublevel caving mines," in *Second International Symposium on Block and Sublevel Caving*, 2010, pp. 237–251.

[121] C. R. Leonardi, D. R. J. Owen, Y. Feng, and W. J. Ferguson, "Computational modelling of fines migration in block caving operations," in *5Th Conference and Exhibition on Mass*

Mining, 2008, pp. 1063–1072.

[122] C. R. Leonardi, D. R. J. Owen, and Y. T. Feng, "Simulation of fines migration using a non-Newtonian lattice Boltzmann-discrete element model: Part II: 3D extension and applications," *Eng. Comput. (Swansea, Wales)*, vol. 29, no. 4, pp. 392–418, 2012, doi: 10.1108/02644401211227635.

[123] T. Ross and A. Van As, "Major Hazards Associated with Block Caving," in *6th International Conference & Exhibition on Mass Mining, Massmin 2012*, 2012.

[124] G. Flores-Gonzalez, "Major hazards associated with cave mining: are they manageable?," in *Mining Geomechanical Risk 2019*, 2019, pp. 31–46. doi: 10.36487/acg_rep/1905_0.3_flores-gonzalez.

[125] J. Jakubec, R. Clayton, and A. R. Guest, "Mudrush risk evaluation," 2012.

[126] G. Chitombo, "Importance of Geology in Cave Mining," *SEG Discov.*, no. 119, pp. 1–21, 2019, doi: 10.5382/geo-and-mining-05.

[127] M. Ferrada, "Gravity Flow Under Moisture Conditions – Control and Management of Drawpoint Mudfl ow," in *Proceedings of the 35th International Symposium of Application of Computers and Operations Research in the Minerals Industry, APCOM 2011*, 2011, pp. 761–764.

[128] A. Holder, A. J. Rogers, P. J. Bartlett, and G. J. Keytert, "Review of mud rush mitigation on kimberley's old scraper drift block caves," *J. South. African Inst. Min. Metall.*, vol. 113, no. 7, pp. 529–537, 2013.

[129] G. Hubert, S. Dirdjosuwondo, R. Plaisance, and L. Thomas, "Tele-Operation at Freeport to Reduce Wet Muck Hazards," in *Massmin 2000 proceedings*, 2000, pp. 173–180.

[130] E. Samosir, J. Basuni, E. Widijanto, and T. Syaifullah, "The Management of Wet Muck at PT Freeport Indonesia's Deep Ore Zone Mine," in *5Th Conference and Exhibition on Mass Mining*, 2008, pp. 322–332.

[131] E. Widijanto, A. D. Wilson, and L. Soebari, "Lessons Learned in Wet Muck Management in Ertsberg East Skarn System of PT Freeport Indonesia," 2012.

[132] S. Firmanulhaq, J. Kamarea, R. Hasan, F. Putra, and F. Salim, "Lessons learnt from egress drift excavation through a minor pillar in an extraction level, Deep Ore Zone mine, Freeport Indonesia, Papua," in *Underground Mining Technology 2017*, 2017, pp. 645–654. doi: 10.36487/acg_rep/1710_53_firmanulhaq.

[133] A. Hekmat, A. Anani, F. Tapia, and I. Navia, "Mud inflow risk assessment in block caving operation based on AHP comprehensive method," in *Proceedings of the 18th Symposium on Environmental Issues and Waste Management in Energy and Mineral Production*, 2018, pp. 51–66.

[134] R. Castro, D. Garcés, A. Brzovic, and F. Armijo, "Quantifying Wet Muck Entry Risk for Long-term Planning in Block Caving," *Rock Mech. Rock Eng.*, vol. 51, no. 9, pp. 2965–2978, 2018, doi: 10.1007/s00603-018-1512-3.

[135] L. E. Widodo, E. Widijanto, I. Faadhilah, and W. Sunyoto, "Fuzzy-Based Prediction of Spatio-Temporal Distribution of Wet Muck in Block Cave Mine of PT Freeport Indonesia," *J. Eng. Technol. Sci.*, vol. 50, no. 2, pp. 291–313, 2018, doi: 10.5614/j.eng.technol.sci.2018.50.2.9.

[136] M. E. Killion, "Design Pressures in Circular Bins," *J. Struct. Eng.*, vol. 111, no. 8, pp. 1760–1774, 1985, doi: 10.1061/(asce)0733-9445(1985)111:8(1760).

[137] F. Mahmoodi, "Compression mechanics of powders and granular materials probed by force distributions and a micromechanically based compaction equation," Uppsala University, 2012.

[138] S. Bock and S. Prusek, "Numerical study of pressure on dams in a backfilled mining shaft based on PFC3D code," *Comput. Geotech.*, vol. 66, pp. 230–244, 2015.

[139] D. F. Bagster, "A note on the pressure ratio in the Janssen equation," *Powder Technol.*, vol. 4, pp. 235–237, 1971.

[140] J.-P. Bouchaud, M. E. Cates, and P. Claudin, "Stress Distribution in Granular Media and Nonlinear Wave Equation," *J. Phys. I*, vol. 5, no. 6, pp. 639–656, 1995, doi: 10.1051/jp1:1995157.

[141] L. Vanel, P. Claudin, J. P. Bouchaud, M. E. Cates, E. Clément, and J. P. Wittmer, "Stresses in silos: Comparison between theoretical models and new experiments," *Phys. Rev. Lett.*, vol. 84, no. 7, pp. 1439–1442, 2000, doi: 10.1103/PhysRevLett.84.1439.

[142] R. M. Nedderman, *Statics and Kinematics of Granular Materials*. Cambridge University Press, 1992.

[143] D. M. Walker, "An approximate theory for pressures and arching in hoppers.," *Chem. Eng. Sci.*, vol. 21, no. 11, pp. 975–997, 1966, doi: 10.1016/0009-2509(67)80145-3.

[144] H. An, X. Wang, X. Fang, Z. Liu, and C. Liang, "Wall normal stress characteristics in an experimental coal silo," *Powder Technol.*, vol. 377, pp. 657–665, 2021, doi: 10.1016/j.powtec.2020.09.016.

[145] K. Pieper, "Investigation if Silo Loads in Measuring Models," *J. Eng. Ind.*, pp. 365–372, 1969.

[146] H. Zhao, X. An, Y. Wu, and X. Yang, "Microscopic analyses of stress profile within confined granular assemblies," *AIP Adv.*, vol. 8, no. 7, 2018, doi: 10.1063/1.5041976.

[147] V. Sundaram and S. C. Cowin, "A reassessment of static bin pressure experiments," *Powder Technol.*, vol. 22, no. 1, pp. 23–32, 1979, doi: 10.1016/0032-5910(79)85004-4.

[148] Y. Y. Yang, S. Zhang, P. Lin, J. F. Wan, L. Yang, and S. Ding, "Influence of wall friction on granular column," *Chinese Phys. B*, vol. 28, no. 1, 2019, doi: 10.1088/1674-1056/28/1/018104.

[149] M. S. Ketchum, *The Design of Walls, Bins and Grain Elevator.*, 3rd ed. New York: McGraw-Hill Book Company Inc., 1919.

[150] H. Zhao, X. An, Y. Wu, and Q. Qian, "DEM modeling on stress profile and behavior in granular matter," *Powder Technol.*, vol. 323, pp. 149–154, 2018, doi: 10.1016/j.powtec.2017.10.006.

[151] Z. Peng, R. Li, and Y. Jiang, "Stress distribution along sidewall of a granular column: Local fluctuation and global determination," *Phys. A Stat. Mech. its Appl.*, vol. 526, p. 120865, 2019, doi: 10.1016/j.physa.2019.04.101.

[152] F. Vivanco, J. Mercado, F. Santibáñez, and F. Melo, "Stress profile in a two-dimensional silo: Effects induced by friction mobilization," *Phys. Rev. E*, vol. 94, no. 2, pp. 1–9, 2016, doi: 10.1103/PhysRevE.94.022906.

[153] G. Flores, "Future challenges and why cave mining must change," in *3rd International symposium on block and sublevel caving*, 2014, pp. 23–52.

[154] C. Fairhurst, "Some Challenges of Deep Mining," *Engineering*, vol. 3, no. 4, pp. 527–537, 2017, doi: 10.1016/J.ENG.2017.04.017.

[155] R. Trueman, M. Pierce, and R. Wattimena, "Quantifying stresses and support requirements in the undercut and production level drifts of block and panel caving mines," *Int. J. Rock Mech. Min. Sci.*, vol. 39, no. 5, pp. 617–632, 2002, doi: 10.1016/S1365-1609(02)00060-6.

[156] E. T. (Edwin T. Brown, "Cave initation by undercutting," in *Block Caving Geomechanics*, Julius Kruttschnitt Mineral Research Centre, 2007, pp. 229–287.

[157] P. J. Barlett, A. Croll, P. Bartlett, and A. Croll, "Cave mining at premier mine," in *Massmin 2000 proceedings*, 2000, pp. 227–234.

[158] M. Callahan, K. Keskimaki, and L. Fronapfel, "Constructing and operating Henderson's new 7210 production level," in *5Th Conference and Exhibition on Mass Mining*, 2008, pp. 15–24.

[159] O. Araneda and A. Sougarret, "Lessons learned in cave mining at the El Teniente mine over the period 1997-2007," in *5Th Conference and Exhibition on Mass Mining*, 2008, pp. 43–52.

[160] F. Fernandez, P. Evans, and R. Gelson, "Design and implementation of a damage assessment system at Argyle Diamond's block cave project," in *Proceedings of the Second International*

Symposium on Block and Sublevel Caving, 2010, pp. 65–81.

[161] J. L. Lett *et al.*, "Undercutting to surface breakthrough – Cadia East panel cave (stage 1)," in *Seventh International Conference & Exhibition on Mass Mining, Massmin 2016*, 2016, pp. 65–82.

[162] L. Snyman, S. Webster, and J. Samosir, "E48 cave extension at Northparkes," in *Seventh International Conference & Exhibition on Mass Mining, Massmin 2016*, 2016, pp. 111–117.

[163] E. Rojas, R. Molina, A. Bonani, and H. Constanzo, "The pre-undercut caving method at the El Teniente mine, Codelco Chile," in *Massmin 2000 proceedings*, 2000, pp. 261–266.

[164] L. Quiñones, C. Lagos, F. Ortiz, E. Farias, L. Toro, and D. Villegas, "Undercut advance direction management at the North 3rd panel, Rio Blanco mine, División Andina Codelco Chile," in *3rd International symposium on block and sublevel caving*, 2014, pp. 91–97.

[165] G. Viegas, K. Bosman, D. Angus, W. De Beer, and T. Urbancic, "Mapping cave front growth utilising the collective behaviour of seismicity and velocity fields," in *Fourth International Symposium on Block and Sublevel Caving, Caving 2018*, 2018, pp. 577–588.

[166] M. P. Richardson, "Area of draw influence and drawpoint spacing for block caving mines," in *Design and operation of caving and sublevel stoping mines*, 1981, pp. 149–156.

[167] D. H. Laubscher, "Mining sequence," in *Block cave manual*, International Caving Study (1997-2000), 2000.

[168] C. Bravo, "Recuperación de reservas colapsadas en minas panel caving," Universidad de Chile, 2010.

[169] A. Karzulovic, "Modelo conceptual del campo de esfuerzos en mina El Teniente," Santiago, 2006.

[170] Z. Y. Xia, Z. Y. Tan, and L. Zhang, "Instability Mechanism of Extraction Structure in Whole Life Cycle in Block Caving Mine," *Geofluids*, vol. 2021, 2021, doi: 10.1155/2021/9932932.

[171] B. Brady and E. T. Brown, *Rock Mechanics for Underground Mining*, Third edit. Kluwer Academic Publishers, 2004.

[172] C. D. Martin, P. K. Kaiser, and D. R. McCreath, "Hoek-Brown parameters for predicting the depth of brittle failure around tunnels," *Can. Geotech. J.*, vol. 36, no. 1, pp. 136–151, 1999, doi: 10.1139/t98-072.

[173] R. Gonzales, R. Munoz, J. Vallejos, and A. Delonca, "Characterisation and monitoring of the stress state of production pillars at El Teniente Mine," in *Seventh International Conference & Exhibition on Mass Mining, Massmin 2016*, 2016, pp. 197–202.

[174] I. Febrian, W. Yudanto, and E. Rubio, "Application of convergence monitoring to manage induced stress by mining activities at PT Freeport Indonesia deep ore zone mine," in *Massmin 2004*, 2004, pp. 269–272.

[175] Z. Y. Xia and Z. Y. Tan, "Study on Instability Mechanism of Extraction Structure under Undercut Space Based on Thin Plate Theory in Block Caving Method," *Shock Vib.*, vol. 2021, 2021, doi: 10.1155/2021/5548213.

[176] G. B. Sharrock, D. A. Beck, G. W. Capes, and I. Brunton, "Applying coupled Newtonian Cellular Automata - Discontinuum Finite Element models to simulate propagation of Ridgeway Deeps Block Cave," 2012.

[177] O. K. Mahabadi, A. Lisjak, A. Munjiza, and G. Grasselli, "Y-Geo: New Combined Finite-Discrete Element Numerical Code for Geomechanical Applications," *Int. J. Geomech.*, vol. 12, no. 6, pp. 676–688, 2012, doi: 10.1061/(asce)gm.1943-5622.0000216.

[178] S. Arndt, T. Bui, T. Diering, I. Austen, and R. Hocking, "ntegrated simulation and optimisation tools for production scheduling using finite element analysis caving geomechanics simulation coupled with 3D cellular automata," in *Caving 2018*, 2018, pp. 247–260.

[179] A. Lisjak *et al.*, "Block caving modelling using the Y-Geo hybrid finite-discrete element code," 2012.

[180] P. A. Cundall and O. D. L. Strack, "A discrete numerical model for granular assemblies," *Geotechnique*, vol. 29, no. 1, pp. 47–65, 1979, [Online]. Available: http://scholar.google.com/scholar?hl=en&btnG=Search&q=intitle:A+discrete+numerical+model+for+granular+assemblies#0

[181] H. Caram and D. Hong, "Diffusing Void Model for granular Flow," *Mod. Phys. Lett. B*, vol. 6, no. 3, pp. 761–771, 1992.

[182] O. Miranda, "FlowSim: Simulador de Flujo Granular," Santiago, 2012.

[183] R. Gonzalez, "Desarrollo de FlowSim 3.0: Simulador de flujo gravitacional para minería de Block/Panel Caving," Universidad de Chile, 2014.

[184] D. Guzman, "Análisis de propagación del Caving y modelamiento mediante FlowSim BC," Universidad de Chile, 2018.

[185] M. Fuentes, "Calibración y desarrollo de FlowSim mediante la utilización de trazadores inteligentes," Universidad de Chile, 2015.

[186] C. Torres, "Recomendación de una malla de extracción en base a simulaciones de flujo gravitacional en FlowSim BC," Universidad de Concepción, 2020.

[187] N. Vega, "Análisis de la contaminación por barro asociado a distintos diseños, mina El Teniente," Universidad de Chile, 2019.

[188] B. Eadie, "A framework for modelling fragmentation in block caving," The University of Queensland, 2003.

[189] E. T. (Edwin T. Brown, *Block caving geomechanics*, Second edi. Julius Kruttschnitt Mineral Research Centre, 2007.

[190] I. Brunton, J. L. Lett, and T. Thornhill, "Fragmentation prediction and assessment at the Ridgeway Deeps and Cadia East cave operation," in *Seventh International Conference & Exhibition on Mass Mining, Massmin 2016*, 2016, pp. 151–160.

[191] V. Lapčević and S. Torbica, "Numerical investigation of caved rock mass friction and fragmentation change influence on gravity flow formation in sublevel caving," *Minerals*, vol. 7, no. 4, p. 56, 2017, doi: 10.3390/min7040056.

[192] E. Brown, "Fragmentation Assessment," in *Block Caving Geomechanics*, 2007, pp. 184–228.

[193] N. Barton, R. Lien, and J. Lunde, "Engineering classification of rock masses for the design of tunnel support," *Rock Mech.*, vol. 6, no. 4, pp. 189–236, 1974, doi: 10.1007/BF01239496.

[194] ISRM, "Suggested methods for the quantitative description of discontinuities in rock masses," *Int. J. Rock Mech. Min. Sci. Geomech. Abstr.*, vol. 15, no. 6, pp. 319–368, 1978.

[195] Z. Sen and E. Eissa, "Volumetric rock quality designation," *J. Geotech. Eng.*, vol. 117, no. 9, pp. 1331–1346, 1991.

[196] A. J. Hardy, T. M. Ryan, and J. M. Kemeny, "Block size distribution of in situ rock masses using digital image processing of drill core," *Int. J. rock Mech. Min. Sci. Geomech. Abstr.*, vol. 34, no. 2, pp. 303–307, 1997, doi: 10.1016/S0148-9062(96)00058-7.

[197] G. S. Esterhuizen, "A program to predict block cave fragmentation." p. 56, 2005.

[198] S. Rogers, D. Elmo, G. Webb, and A. Catalan, "A discrete fracture network based approach to defining in situ, primary and secondary fragmentation distributions for the Cadia East panel cave," in *Second International Symposium on Block and Sublevel Caving*, 2010, pp. 425–440.

[199] D. Elmo, E. Eberhardt, D. Stead, and S. Rogers, "Discrete fracture network modelling – importance of accounting for data uncertainity and variability," in *Seventh International Conference & Exhibition on Mass Mining, Massmin 2016*, 2016, pp. 845–852.

[200] F. Ortiz, "Metodología de Construcción de Modelos DFN, para Determinación de Fragmentación in Situ en el Yacimiento Río Blanco," in *II Congreso Iberoamericano en Minería Subterránea y a Cielo Abierto*, 2018, pp. 242–251.

[201] A. Brzovic, J. P. Hurtado, and N. Marin, "Intensity rock mass preconditioning and fragmentation performance at the El Teniente Mine, Chile," in *3rd International symposium*

on block and sublevel caving, 2014, pp. 547–556.

[202] E. Ghazvinian, B. Damjanac, L. Lorig, P. Cavieres, and A. Madrid, "Back analysis of the effect of hydraulic fracturing preconditioning on mining-induced seismicity at the main access of New Mine Level project, CODELCO Chile - El Teniente Division," in *Eighth International Conference & Exhibition on Mass Mining, Massmin 2020*, 2020, pp. 249–263.

[203] E. Chacón, V. Barrera, R. Jeffrey, and A. van As, "Hydraulic fracturing used to precondition ore and reduce fragment size for block caving," in *Massmin 2004*, 2004, pp. 527–534.

[204] D. Nicholas and A. Srikant, "Assessment of primary fragmentation from drill core data," in *Massmin 2004*, 2004, pp. 55–58.

[205] L. Merino, "Predicting the size distribution of ore fragments in block caving mines," Imperial College, 1986.

[206] D. H. Laubscher, "Secondary fragmentation," in *Block cave manual*, 2000.

[207] M. Pierce, D. Weatherley, and T. Kojovic, "A hybrid methodology for secondary fragmentation prediction in cave mines," in *Second International Symposium on Block and Sublevel Caving*, 2010, pp. 567–581. doi: 10.36487/acg_rep/1002_39_weatherley-pierce.

[208] Z. Chik, "The Effect of Fragmentation on the Engineering Properties of Granular Materials; Laboratory and Fractal Analyses," University of Pittsburgh, 2004.

[209] G. R. McDowell, M. D. Bolton, and D. Robertson, "The Fractal Crushing of Granular Materials," *J. Mech. Phys. Solids*, vol. 44, no. 12, pp. 2079–2102, 1996, doi: 10.1557/s0883769400058747.

[210] R. Handy, "The arch in soil arching," *J. Geotech. Eng.*, vol. 113, no. 3, pp. 269–271, 1985, doi: 10.1061/(ASCE)0733-9410(1987)113:3(269).

[211] L. Dorador, E. Heberhardt, D. Elmo, B. Norman, and A. Aguayo, "Influence of secondary fragmentation and column height on block size distribution and fines migration reaching drawpoints," in *3rd International symposium on block and sublevel caving*, 2014, pp. 128–137.

[212] P. V. Lade, J. A. Yamamuro, and P. A. Bopp, "Significance of Particle Crushing in Granular Materials," *J. Geotech. Geoenvironmental Eng.*, vol. 122, pp. 309–316, 1996, doi: 10.1061/(asce)1090-0241(1997)123:9(889).

[213] K. Lee and I. Farhoomand, "Compressibility and crushing of granular soil in anisotropic triaxial compression," *Can. Geotech. J.*, vol. 4, no. 1, pp. 68–86, 1967.

[214] D. M. Wood and K. Maeda, "Changing grading of soil: Effect on critical states," *Acta Geotech.*, vol. 3, no. 1, pp. 3–14, 2008, doi: 10.1007/s11440-007-0041-0.

[215] G. R. McDowell and M. D. Bolton, "On the micromechanics of crushable aggregates," *Geotechnique*, vol. 48, no. 5, pp. 667–679, 1998, doi: 10.1680/geot.1998.48.5.667.

[216] G. R. McDowell, "On the Yielding and Plastic Compression of Sand," *Soils Found.*, vol. 42, no. 1, pp. 139–145, 2002.

[217] L. Dorador, E. Eberhardt, D. Elmo, and A. Aguayo, "Assessment of broken ore density variations in a block cave draw column as a function of fragment size distributions and fines migration," in *3rd International symposium on block and sublevel caving*, 2014, no. 2012, pp. 1–8.

[218] Y. Nakata, A. F. L. Hyde, M. Hyodo, and H. Murata, "A probabilistic approach to sand particle crushing in the triaxial test," *Geotechnique*, vol. 49, no. 5, pp. 567–583, 1999, doi: 10.1680/geot.1999.49.5.567.

[219] F. Osses, "Ensayos de carga multicontacto para el estudio de ruptura de roca primaria en mina El Teniente," Universidad de Chile, 2014.

[220] I. K. Lee and M. R. Coop, "The intrinsic behaviour of a decomposed granite soil," *Geotechnique*, vol. 45, no. 1, pp. 117–130, 1995.

[221] N. Miura and T. Yamanouchi, "Effect of water on the behavior of a quartz-rich sand under high stresses," *Soils Found.*, vol. 15, no. 4, pp. 24–34, 1975.

[222] R. Gómez, "Experimetal assessment of hang-up and secondary fragmentation for block

caving," Universidad de Chile, 2015.

[223] D. Verma, A. Kainthola, T. N. Singh, and R. Thareja, "International Research Journal of Geology and Mining," *Int. Res. J. Geol. Min.*, vol. 4, no. 4, pp. 122–132, 2014, doi: 10.14303/irjgm.2014.024.

[224] C. Torres, "Rate of draw effect on fragmentation," Santiago, 2019.

[225] D. Landriault, "Backfill in Undergound Mining," in *Underground Mining Methods*, SME, 2001, pp. 601–614.

[226] T. R. Yu, "Some factors relating to the stability of consolidated rockfill at Kidd Creek," in *Innovations in Mining Backfill Technology*, 1989, pp. 279–286.

[227] L. Dorador, E. Eberhardt, and D. Elmo, "Influence of rock mass veining and non-persistent joints on secondary fragmentation during block caving," in *Fourth International Symposium on Block and Sublevel Caving, Caving 2018*, 2018, pp. 271–282. doi: 10.36487/acg_rep/1815_18_dorador.

[228] A. Brzovic and E. Villaescusa, "Rock mass characterization and assessment of block-forming geological discontinuities during caving of primary copper ore at the El Teniente mine, Chile," *Int. J. Rock Mech. Min. Sci.*, vol. 44, no. 4, pp. 565–583, 2007, doi: 10.1016/j.ijrmms.2006.09.010.

[229] M. Pierce and M. Fuenzalida, "Application of a methodology for secondary fragmentation prediction in cave mines," in *3rd International symposium on block and sublevel caving*, 2014, pp. 318–327.

[230] W. Hustrulid, "Method selection for large-scale underground mining," in *Massmin 2000 proceedings*, 2000, pp. 29–56.

[231] B. Y. S. R. Broadbent and T. G. Callcott, "A matrix analysis of processes involving particle assemblies," *Philos. Trans. R. Soc. London. Ser. A, Math. Phys. Sci.*, vol. 249, no. 960, pp. 99–123, 1956, doi: 10.1098/rsta.1956.0016.

[232] Broad National Materials Advisory, "Comminution and energy consumption," 1981.

[233] A. Lynch, *Mineral crushing and grinding circuits, their simulation, optimization, design and control*. Amsterdam: Elsevier Scientific Publishing Company, 1997.

[234] J. Blondel and J. Soffia, "Geotecnia área Ten-5 Pilares," 1990.

[235] Golder, "FracMan." FracMan Technology Group, 2012.

[236] J. Castillo, "Desarrollo de metodología de fragmentación en minería de caving," Universidad de Concepción, 2021.

[237] S. López and R. Castro, "Análisis de formación de colgaduras en el boque 2 de la Mina Esmeralda," in *II Congreso Iberoamericano en Minería Subterránea y a Cielo Abierto*, 2018, pp. 82–94.

[238] L. F. Orellana, "Evaluación de variables de Diseño del Sistema de Minería Continua a Partir de Experimentación en Laboratorio," Universidad de Chile, 2012.

[239] G. Sotomayor, "Recomendación de malla de extracción para el proyecto Mina Chuquicamata Subterránea," Universidad de Chile, 2016.

[240] R. Castro, S. López, R. Gómez, S. Ortiz, and N. Carreño, "Experimental Study of the Influence of Drawbell Geometry on Hang-Ups in Cave Mine Applications," *Rock Mech. Rock Eng.*, vol. 54, no. 1, pp. 1–10, 2020, doi: 10.1007/s00603-020-02247-4.

[241] J. Hadjigeorgiou, J. F. Lessard, and F. Mercier-Langevin, "Ore pass practice in Canadian mines," *J. South African Inst. Min. Metall.*, vol. 105, no. 11, pp. 809–816, 2005.

[242] J. Hurtado and J. Pereira, "INFORME DE AVANCE BACKANALYSIS DE FRAGMENTACIÓN : SECTOR RESERVAS NORTE (RENO). API T06E209.," Rancagua, 2009.

[243] A. Brzovic *et al.*, "Analysis and modelling of the fragmentation process—case studies at El Teniente Mine," in *Proceedings of the seventh international conference on mass mining, Massmin 2016*, 2016, pp. 305–310.

[244] L. Araya, "Modelamiento empírico de colgaduras en minería de caving," Universidad de

Chile, 2018.

[245] M. Beus, W. Pariseau, B. Stewart, and S. Iverson, "Design of ore passes," in *Underground mining methods*, W. Hustrulid and R. Bullock, Eds. 2001, pp. 627–634.

[246] A. Sato and H. Tang, "Analysis of Ore Pass Hang-Ups in Long Vertical Ore Passes by 3-D DEM," *Int. J. Min. Eng. Miner. Process.*, vol. 9, no. 1, pp. 1–11, 2020, doi: 10.5923/j.mining.20200901.01.

[247] S. Maass, "Alternativas tecnologicas para el descuelgue de zanjas," Universidad de Chile, 2013.

[248] S. Dessureaul, M. Scoble, and E. Rubio, "Simulating Block Cave Secondary Breakage — An Application of Information and Operations Management Tools in Mass Mining Systems," in *Massmin 2000 proceedings*, 2000, pp. 893–896.

[249] G. Van Hout, S. Allen, M. Breed, and J. Singleton, "Status of draw control practice and waste Management at Cullinan diamond mine," in *Massmin 2004*, 2004, pp. 491–499.

[250] F. Carrasco, V. Encina, and S. Maass, "Extraction rate: As an index of effectiveness," in *Massmin 2004*, 2004, pp. 469–473.

[251] A. Ovalle, "Mass Caving Maximum Production Capacity," 2012.

[252] C. Kurniawan and T. B. Setyoko, "Impact of rock type variability on production rates and scheduling at the DOZ-ESZ block cave mine," in *5Th Conference and Exhibition on Mass Mining*, 2008, no. June, pp. 291–302.

[253] S. Ngidi and D. Pretorius, "Impact of poor fragmentation on cave management," in *Second International Symposium on Block and Sublevel Caving*, 2010, pp. 593–601.

[254] R. J. Butcher, "Block Cave Undercutting - Aims, Strategies, Methods and Management," in *Massmin 2000 proceedings*, 2000, pp. 423–428.

[255] G. Baiden, "Telerobotics for hang-up assessment and removal - an idea whose time has come," in *First international conference on underground mining technology*, 2017, pp. 597–607.

[256] I. Consulting, "Levantamiento y evaluación de prácticas de reducción secundaria," Santiago, 2006.

[257] K. Calder, P. Townsend, and F. Russel, "The Palabora Underground Mine Project," in *Massmin 2000 proceedings*, 2000, pp. 219–226.

[258] T. Szwedzicki, "Formation and removal of hang-ups in ore passes," *Trans. Institutions Min. Metall. Sect. A Min. Technol.*, vol. 116, no. 3, pp. 139–145, 2007, doi: 10.1179/174328607X191047.

[259] J. Hadjigeorgiou and J. F. Lessard, "Strategies for restoring material flow in ore and waste pass systems," *Int. J. Mining, Reclam. Environ.*, vol. 24, no. 3, pp. 267–282, 2010, doi: 10.1080/17480931003658894.

[260] D. H. Laubscher, "Secondary breakage," in *Block cave manual*, Julius Kruttschnitt Mineral Research Centre, 2000.

[261] P. Paredes, F. Rodríguez, R. Castro, D. Morales, and D. García, "Design and evaluation of single-phase drawbell excavation at the Chuquicamata underground mine," *J. South. African Inst. Min. Metall.*, vol. 119, no. 12, pp. 1061–1070, 2020, doi: 10.17159/2411-9717/682/2020.

[262] B. Hardin, "Crushing of Soil Particles," *J. Geotech. Eng.*, vol. 111, pp. 1177–1192, 1985.

[263] H. Liu, Z. Xia, F. Ren, and R. He, "Study on Discrete Element Simulation of Secondary Rock Failure Characteristics in Granular Media," *Geotech. Geol. Eng.*, vol. 37, no. 4, pp. 2503–2511, 2019, doi: 10.1007/s10706-018-00772-2.

[264] P. Cundall, M. Pierce, and D. Mas Ivars, "Quantifying the Size Effect of Rock Mass Strength," in *SHIRMS 2008*, 2008, no. July, pp. 3–15. doi: 10.36487/acg_repo/808_31.

[265] J. Manso, J. Marcelino, and L. Caldeira, "Single-particle crushing strength under different relative humidity conditions," *Acta Geotech.*, vol. 16, no. 3, pp. 749–761, 2021, doi: 10.1007/s11440-020-01065-w.

[266] B. L. Sainsbury, "Sensitivies in the numerical assessment of cave propagation," in *Second International Symposium on Block and Sublevel Caving*, 2010, pp. 523–538.

[267] A. Srikant, D. Nicholas, and L. Rachmad, "Visual estimation of fragment size distributions in the DOZ block cave," in *Massmin 2004*, 2004, pp. 286–290.

[268] K. J. Reid, "A solution to the batch grinding equation," *Chem. Eng. Sci.*, vol. 20, pp. 953–963, 1965.

[269] R. R. Klimpel and L. G. Austin, "The Back calculation of specific rates of breakage and non-normalized breakage distribution parameters from batch grinding data," *Int. J. Miner. Process.*, vol. 4, pp. 7–32, 1977.

[270] J. A. Herbst and D. W. Fuerstenau, "Scale-UP procedure for continuous grinding mill design using population balance models," *Int. J. Miner. Process.*, vol. 7, pp. 1–31, 1980.

[271] L. G. Austin and P. T. Luckie, "The estimation of non-normalized breakage distribution parameters from batch grinding tests," *Powder Technol.*, vol. 5, no. 5, pp. 267–271, 1972, doi: 10.1016/0032-5910(72)80030-5.

[272] L. Austin and F. Concha, *Diseño y simulación de circuitos de molienda y clasificación*. CYTED, 1994.

[273] G.-C. Cho, J. Dodds, and J. C. Santamarina, "Particle Shape Effects on Packing Density, Stiffness, and Strength: Natural and Crushed Sands," *J. Geotech. Geoenvironmental Eng.*, vol. 132, no. 5, pp. 591–602, 2006, doi: 10.1061/(asce)1090-0241(2006)132:5(591).

[274] J. More and D. C. Sorensen, "Computing a trust region step," *SIAM J. Sci. Stat. Comput.*, vol. 4, no. 3, pp. 553–572, 1983.

[275] D. H. Laubscher, "Potential draw rate," in *Block cave manual*, Julius Kruttschnitt Mineral Research Centre, 2000.

[276] J. Jakubec, "Fragmentation estimates using BCF software - experiences and pitfalls," in *3rd International symposium on block and sublevel caving*, 2014, pp. 191–200.

[277] G. R. McDowell and A. Humphreys, "Yielding of granular materials," *Granul. Matter*, vol. 4, no. 1, pp. 1–8, 2002, doi: 10.1007/s10035-001-0100-4.

[278] B. Brady and E. Brown, "Rock strength and deformability," in *Rock mechanics for Underground Mining*, Third edit., Kluwer Academic Publishers, 2004, pp. 85–139.

[279] R. Marsal, "Particle breakage," in *Mechanical properties of rockfill*, Wiley and Sons, Incorporated, 1973, pp. 130–140.

[280] R. Marsal, *Research on the behavior of granular materials and rockfill samples*. 1965.

[281] M. Hyodo, A. Hyde, N. Aramaki, and Y. Nakata, "undrained Monotonic and Cyclic Shear Behaviour of Sanf Under Low and High Confining Stresses," *Soils Found.*, vol. 42, no. 3, pp. 63–76, 2002.

[282] ASTM D3080/D3080M, "Standard test method for direct shear test of soils under consolidated drained conditions," *Am. Soc. Test. Mater.*, 2011.

[283] ASTM D5731, "Standard Test Method for Determination of the Point Load Strength Index of Rock and Application to Rock Strength Classifications," *Am. Soc. Test. Mater.*, 2008.

[284] A. M. Scott and J. Bridgwater, "Interparticle Percolation: A Fundamental Solids Mixing Mechanism," *Ind. Eng. Chem. Fundam.*, vol. 14, no. 1, pp. 22–27, 1975, doi: 10.1021/i160053a004.

[285] C. Cerrutti, A. Ovalle, and Y. Vergara, "How high a draw column in block caving?," in *3rd International symposium on block and sublevel caving*, 2014, pp. 674–683.

[286] D. Cuello and G. Newcombe, "Key geotechnical knowledge and practical mine planning guidelines in deep, high-stress, hard rock conditions for block and panel caving mining," in *Fourth International Symposium on Block and Sublevel Caving, Caving 2018*, 2018, pp. 17–36.

[287] R. Gómez, R. Castro, F. Betancourt, and M. Moncada, "Comparison of normalized and non-normalized block caving comminution models," *J. South. African Inst. Min. Metall.*, vol. 121, no. 11, pp. 581–588, Nov. 2021, doi: 10.17159/2411-9717/1150/2021.

[288] W. long Shen, J. biao Bai, X. yu Wang, and Y. Yu, "Response and control technology for entry loaded by mining abutment stress of a thick hard roof," *Int. J. Rock Mech. Min. Sci.*, vol. 90, no. September, pp. 26–34, 2016, doi: 10.1016/j.ijrmms.2016.10.001.

[289] J. Jaky, "Earth pressure - pressure in silos," in *Second International Conference on Soil Mechanics and Foundation Engineering*, 1948, pp. 103–107.

[290] R. M. Nedderman, "The method of differencial slices," in *Static and Kinematic of Granular Materials*, Cambridge University Press, 1992, pp. 84–126.

[291] J. Munch-Andersen, O. Ditlevsen, C. Christensen, S. Randrup-Thomsen, and P. Hoffmeyer, "Empirical Stochastic Silo Load Model. II: Data Analysis," *J. Eng. Mech.*, vol. 121, no. 9, pp. 981–986, 1995, doi: 10.1061/(asce)0733-9399(1995)121:9(987).

[292] C. S. Chou, Y. C. Chuang, J. Smid, S. S. Hsiau, and J. T. Kuo, "Flow patterns and stresses on the wall in a moving granular bed with eccentric discharge," *Adv. Powder Technol.*, vol. 13, no. 1, pp. 1–23, 2002, doi: 10.1163/15685520252900929.

[293] K. Hoeg, "Stresses against underground estrcutural cylinders," *J. oif Soil Mech. Found. Divition*, vol. 94, no. 4, pp. 833–858, 1968, doi: 10.1061/JSFEAQ.0001175.

[294] K. N. Berntsen and O. Ditlevsen, "Stochastic stresses in granular matter simulated by dripping identical ellipses into plane silo," *Stoch. Stress. Granul. matter simulated by dripping identical ellipses into Pl. silo*, no. October 1999, pp. 57--64, 2000.

[295] C. Colonnello, L. I. Reyes, E. Clément, and G. Gutiérrez, "Behavior of grains in contact with the wall of a silo during the initial instants of a discharge-driven collapse," *Phys. A Stat. Mech. its Appl.*, vol. 398, pp. 35–42, 2014, doi: 10.1016/j.physa.2013.12.010.

[296] R. Kobyłka, J. Horabik, and M. Molenda, "Numerical simulation of the dynamic response due to discharge initiation of the grain silo," *Int. J. Solids Struct.*, vol. 106–107, pp. 27–37, 2017, doi: 10.1016/j.ijsolstr.2016.12.001.

[297] J. A. Knappett and R. F. Craig, "Basic characteristic of soils," in *Craig's soil mechanics*, Eigth., Spon press editorial, 2012, pp. 3–38.

[298] J. W. Landry, G. S. Grest, and S. J. Plimpton, "Discrete element simulations of stress distributions in silos: Crossover from two to three dimensions," *Powder Technol.*, vol. 139, no. 3, pp. 233–239, 2004, doi: 10.1016/j.powtec.2003.10.016.

[299] Y. C. Zhou, B. H. Xu, R. P. Zou, A. B. Yu, and P. Zulli, "Stress distribution in a sandpile formed on a deflected base," *Adv. Powder Technol.*, vol. 14, no. 4, pp. 401–410, 2003, doi: 10.1163/156855203769710636.

[300] R. Kobyłka and M. Molenda, "DEM modelling of silo load asymmetry due to eccentric filling and discharge," *Powder Technol.*, vol. 233, pp. 65–71, 2013, doi: 10.1016/j.powtec.2012.08.039.

[301] A. J. Matchett, P. A. Langston, and D. McGlinchey, "A model for stresses in a circular silo with an off-centre circular core, using the concept of a principal stress cap: Solution for a completely filled silo and comparison with Janssen and DEM data," *Chem. Eng. Res. Des.*, vol. 93, no. July, pp. 330–348, 2015, doi: 10.1016/j.cherd.2014.07.006.

[302] P. Wang, L. Zhu, and X. Zhu, "Flow pattern and normal pressure distribution in flat bottom silo discharged using wall outlet," *Powder Technol.*, vol. 295, pp. 104–114, 2016, doi: 10.1016/j.powtec.2016.03.036.

[303] R. Kobyłka, M. Molenda, and J. Horabik, "Loads on grain silo insert discs, cones, and cylinders: Experiment and DEM analysis," *Powder Technol.*, vol. 343, pp. 521–532, 2019, doi: 10.1016/j.powtec.2018.11.032.

[304] A. R. Guest, G. Van Hout, A. von Johannides, and L. F. Scheepers, "An application of linear programming for block cave draw control," in *Massmin 2000 proceedings*, 2000, pp. 461–468.

[305] V. E. Hooker and D. Bickel, *Overcoring equipment and techniques: used in rock stress determination*. US Bureau of Mines, 1974.

[306] B. Brady and E. Brown, "Premining state of the stress analysis," in *Rock mechanics for*

Underground Mining, Third edit., Kluwer Academic Publishers, 2004, pp. 142–164.

[307] C. H. Liu *et al.*, "Force fluctuations in bead packs," *Science (80-.).*, vol. 269, no. 5223, pp. 513–515, 1995, doi: 10.1126/science.269.5223.513.

[308] S. Coppersmith, C. Liu, S. Majumdar, O. Narayan, and T. Witten, "Model for force fluctuations in bead packs," *Phys. Rev. E*, vol. 53, no. 5, pp. 4673–4685, 1996.

[309] J. Hemmingsson, H. Herrmann, and S. Roux, "Vectorial Cellular Autolnaton for the Stress in Granular Media," *J. Phys. I*, vol. 7, no. 2, pp. 291–302, 1997.

[310] X. T. Feng, P. Z. Pan, and H. Zhou, "Simulation of the rock microfracturing process under uniaxial compression using an elasto-plastic cellular automaton," *Int. J. Rock Mech. Min. Sci.*, vol. 43, no. 7, pp. 1091–1108, 2006, doi: 10.1016/j.ijrmms.2006.02.006.

[311] F. Yan, P. Z. Pan, X. T. Feng, and S. J. Li, "The continuous-discontinuous cellular automaton method for elastodynamic crack problems," *Eng. Fract. Mech.*, vol. 204, no. October, pp. 482–496, 2018, doi: 10.1016/j.engfracmech.2018.10.025.

[312] P. Z. Pan, F. Yan, X. T. Feng, Z. Wu, and S. Qiu, "Modeling of an excavation-induced rock fracturing process from continuity to discontinuity," *Eng. Anal. Bound. Elem.*, vol. 106, no. May, pp. 286–299, 2019, doi: 10.1016/j.enganabound.2019.05.014.

[313] I. Zuriguel, T. Mullin, and J. M. Rotter, "Effect of particle shape on the stress dip under a sandpile," *Phys. Rev. Lett.*, vol. 98, no. 2, pp. 1–4, 2007, doi: 10.1103/PhysRevLett.98.028001.

[314] G. S. Esterhuizen, L. Rachmad, A. V. Potapov, and L. K. Nordell, "Investigation of swell factor in a block cave draw column," in *Massmin 2004*, 2004, pp. 215–219.

[315] L. Dorador, E. Eberhardt, and D. Elmo, "Procedure for estimating broken ore density distribution within a draw column during block caving," *Min. Technol. Trans. Inst. Min. Metall.*, vol. 130, no. 3, pp. 131–145, 2021, doi: 10.1080/25726668.2021.1886544.

[316] ASTM, "Standard test method for specific gravity and absorption of coarse aggregate," *ASTM Stand.*, vol. 83, pp. 7–9, 2021.

[317] L. L. Lapin, *Probability and statistics for modern*. Boston: Engineering, Thomson information/publishing group, 1990.

[318] T. Diering and O. Richter, "Block cave production scheduling using PCBC," in *Proceedings of the SME Annual Meeting & Exhibit*, 2010, pp. 455–467.

[319] J. P. Hurtado, "Fragmentation back analysis at El Teniente 1993– 2013," Rancagua, 2014.

[320] M. E. Pierce, "PFC3D modeling of inter-particle percolation in caved rock under draw," in *Numerical Modeling in Micromechanics via Particle Methods*, 2004, pp. 149–156.

[321] H. Sun, Y. Gao, D. Elmo, A. Jin, S. Wu, and L. Dorador, "A Study of Gravity Flow Based on the Upside-Down Drop Shape Theory and Considering Rock Shape and Breakage," *Rock Mech. Rock Eng.*, vol. 52, no. 3, pp. 881–893, 2019, doi: 10.1007/s00603-018-1514-1.

[322] D. Deserable, "A VERSATILE TWO-DIMENSIONAL CELLULAR AUTOMATA NETWORK FOR GRANULAR FLOW," *SIAM J. Appl. Math.*, vol. 62, no. 4, pp. 1414–1436, 2002.

[323] J. Bridgwater, D. F. Bagster, S. F. Chen, and J. H. Hallam, "Geometric and dynamic similarity in particle mixing," *Powder Technol.*, vol. 2, no. 4, pp. 198–206, 1969, doi: 10.1016/0032-5910(69)80013-6.

[324] J. Bridgwater, "Fundamental powder mixing mechanisms," *Powder Technol.*, vol. 15, no. 2, pp. 215–236, 1976, doi: 10.1016/0032-5910(76)80051-4.

[325] D. Julin, "Block caving," in *SME Mining Engineering Handbook*, Hartman, Ed. SME, 1992, pp. 1815–1836.

[326] D. Villa and E. Farias, "Remanent ore model generation and categorization post-block caving extraction at El Salvador Mine," in *Seventh International Conference & Exhibition on Mass Mining, Massmin 2016*, 2016, pp. 461–470.

[327] J. Von Neumann, "The general and logical theory of automata." pp. 1–41, 1951.

[328] H. L. Langhaar, *Dimensional Analysis and Theory of Models*. New York: wiley, 1951.

[329] IM2, "Hydraulic fracture evaluation for preconditioning on primary rock of Salvador mine," Santiago, 2005.